Universidade do Minho
Escola de Engenharia

Hélder David Malheiro da Silva

Indoor Positioning System for Wireless Sensor Networks

FCT Fundação para a Ciência e a Tecnologia
MINISTÉRIO DA CIÊNCIA, TECNOLOGIA E ENSINO SUPERIOR

Hélder David Malheiro da Silva **Indoor Positioning System for Wireless Sensor Networks**

UMinho | 2016

maio de 2016

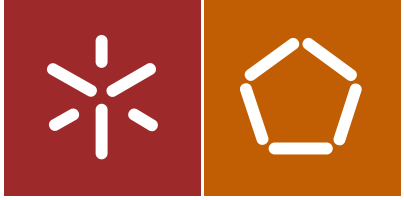

Universidade do Minho
Escola de Engenharia

Hélder David Malheiro da Silva

Indoor Positioning System for Wireless Sensor Networks

Tese de Doutoramento
Programa Doutoral em Engenharia Electrónica e Computadores

Trabalho efectuado sob a orientação do
Professor Doutor Luís Alexandre Rocha
Professor Doutor José Augusto Afonso

maio de 2016

STATEMENT OF INTEGRITY

I hereby declare having conducted my thesis with integrity. I confirm that I have not used plagiarism or any form of falsification of results in the process of the thesis elaboration.

I further declare that I have fully acknowledged the Code of Ethical Conduct of the University of Minho.

University of Minho, 31st of May 2016

Full name: Hélder David Malheiro da Silva

Signature: Hélder David Malheiro da Silva

Acknowledgments

First and foremost, I would like to show my deepest gratitude for my supervisors, Professor Luis Alexandre Rocha and Professor José Augusto Afonso, for the scientific guidance, support, advices and suggestions, crucial to the work of my PhD thesis.

To my friends Pedro Macedo and Miguel Silva, for their valuable input and for always being ready to help with any questions or tasks I had to accomplish.

To all my friends from University of Minho, in particular everyone that was part of the Micro and Nanotechnologies Laboratory, for their friendship, the laughs and the good times that we spent together. I know… cake is on me.

To Bruno Monteiro for the enlightening and never-ending conversations about information.

To Liliana Correia for anything and everything during all these years and the ones still to come.

To my dear parents, Constantino Silva and Maria Brasilissa, and my brothers, Paulo Silva and João Silva for their motivation and unconditional support.

I would like to acknowledge the Fundação para a Ciência e a Tecnologia (FCT), for the financial support under the PhD scholarship SFRH/BD/78018/2011. I would also like to acknowledge the doctoral program in Electronics and Computer Engineering for supporting this work.

Abstract

Positioning technologies are ubiquitous nowadays. From the implementation of the global positioning system (GPS) until now, its evolution, acceptance and spread has been unanimous, due to the underlying advantages the system brings. Currently, these systems are present in many different scenarios, from the home to the movie theatre, at work, during a walk in the park. Many applications provide useful information, based on the current position of the user, in order to provide results of interest.

Positioning systems can be implemented in a wide range of contexts: in hospitals to locate equipment and guide patients to the necessary resources, or in public spaces like museums, to guide tourists during visits. They can also be used in a gymnasium to point the user to his next workout machine and, simultaneously, gather information regarding his fitness plan. In a congress or conference, the positioning system can be used to provide information to its participants about the on-going presentations. Devices can also be monitored to prevent thefts.

Privacy and security issues are also important in positioning systems. A user might not want to be localized or its location to be known, permanently or during a time interval, in different locations. This information is therefore sensitive to the user and influences directly the acceptance of the system itself.

Concerning outdoor systems, GPS is in fact the system of reference. However, this system cannot be used in indoor environment, due to the high attenuation of the satellite signals from non-line-of-sight conditions. Another issue related to GPS is the power consumption. The integration of these devices with wireless sensor networks becomes prohibitive, due to the low power consumption profile associated with devices in this type of networks. As such, this work proposes an indoor positioning system for wireless sensor networks, having in consideration the low energy consumption and low computational capacity profile.

The proposed indoor positioning system is composed of two modules: the received signal strength positioning module and the stride and heading positioning module. For the first module, an experimental performance comparison between several received signal strength based algorithms was conducted in order to assess its performance in a predefined

indoor environment. Modifications to the algorithm with higher performance were implemented and evaluated, by introducing a model of the effect of the human body in the received signal strength.

In the case of the second module, a stride and heading system was proposed, which comprises two subsystems: the stride detection and stride length estimation system to detect strides and infer the travelled distance, and an attitude and heading reference system to provide the full three-dimensional orientation stride-by-stride.

The stride detection enabled the identification of the gait cycle and detected strides with an error percentage between 0% and 0.9%. For the stride length estimation two methods were proposed, a simplified method, and an improved method with higher computational requirements than the former. The simplified method estimated the total distance with an error between 6.7% and 7.7% of total travelled distance. The improved method achieved an error between 1.2% and 3.7%. Both the stride detection and the improved stride length estimation methods were compared to other methods in the literature with favourable results.

For the second subsystem, this work proposed a quaternion-based complementary filter. A generic formulation allows a simple parameterization of the filter, according to the amount of external influences (accelerations and magnetic interferences) that are expected, depending on the location that the device is to be attached on the human body. The generic formulation enables the inclusion/exclusion of components, thus allowing design choices according to the needs of applications in wireless sensor networks. The proposed method was compared to two other existing solutions in terms of robustness to interferences and execution time, also presenting a favourable outcome.

Keywords - Indoor positioning, wireless sensor networks, received signal strength, body effect, propagation model, stride and heading system, attitude and heading reference system, sensor fusion.

Resumo

Os sistemas de posicionamento fazem parte do quotidiano. Desde a implementação do sistema GPS (Global Positioning System) até aos dias que correm, a evolução, aceitação e disseminação destes sistemas foi unânime, derivada das vantagens subjacentes da sua utilização. Hoje em dia, eles estão presentes nos mais variados cenários, desde o lar até à sala de cinema, no trabalho, num passeio ao ar livre. São várias as aplicações que nos fornecem informação útil, usando como base a descrição da posição atual, de modo a produzir resultados de maior interesse para os utilizadores.

Os sistemas de posicionamento podem ser implementados nos mais variados contextos, como por exemplo: nos hospitais, para localizar equipamento e guiar os pacientes aos recursos necessários, ou nas grandes superfícies públicas, como por exemplo museus, para guiar os turistas durante as visitas. Podem ser igualmente utilizados num ginásio para indicar ao utilizador qual a máquina para onde se deve dirigir durante o seu treino e, simultaneamente, obter informação acerca desta mesma máquina. Num congresso ou conferência, o sistema de localização pode ser utilizado para fornecer informação aos seus participantes sobre as apresentações que estão a decorrer no momento. Os dispositivos também podem ser monitorizados para prevenir roubos.

Existem também questões de privacidade e segurança associados aos sistemas de posicionamento. Um utilizador poderá não desejar ser localizado ou que a sua localização seja conhecida, permanentemente ou num determinado intervalo de tempo, num ou em vários locais. Esta informação é por isso sensível ao utilizador e influencia diretamente a aceitação do próprio sistema.

No que diz respeito aos sistemas utilizados no exterior, o GPS (ou posicionamento por satélite) é de facto o sistema mais utilizado. No entanto, em ambiente interior este sistema não pode ser usado, por causa da grande atenuação dos sinais provenientes dos satélites devido à falta de linha de vista. Um outro problema associado ao recetor GPS está relacionado com as suas características elétricas, nomeadamente os consumos energéticos. A integração destes dispositivos nas redes de sensores sem fios torna-se proibitiva, devido ao perfil de baixo consumo associado a estas redes.

Este trabalho propõe um sistema de posicionamento para redes de sensores sem fio em ambiente interior, tendo em conta o perfil de baixo consumo de potência e baixa capacidade de processamento.

O sistema proposto é constituído por dois módulos: o modulo de posicionamento por potência de sinal recebido e o módulo de navegação inercial pedestre. Para o primeiro módulo foi feita uma comparação experimental entre vários algoritmos que utilizam a potência do sinal recebido, de modo a avaliar a sua utilização num ambiente interior pré-definido. Ao algoritmo com melhor prestação foram implementadas e testadas modificações, utilizando um modelo do efeito do corpo na potência do sinal recebido.

Para o segundo módulo foi proposto um sistema de navegação inercial pedestre. Este sistema é composto por dois subsistemas: o subsistema de deteção de passos e estimação de distância percorrida; e o subsistema de orientação que fornece a direção do movimento do utilizador, passo a passo.

O sistema de deteção de passos proposto permite a identificação das fases da marcha, detetando passos com um erro entre 0% e 0.9%. Para o sistema de estimação da distância foram propostos dois métodos: um método simplificado de baixa complexidade e um método melhorado, mas com maiores requisitos computacionais quando comparado com o primeiro. O método simplificado estima a distância total com erros entre 6.7% e 7.7% da distância percorrida. O método melhorado por sua vez alcança erros entre 1.2% e 3.7%. Ambos os sistemas foram comparados com outros sistemas da literatura apresentando resultados favoráveis.

Para o sistema de orientação, este trabalho propõe um filtro complementar baseado em quaterniões. É utilizada uma formulação genérica que permite uma parametrização simples do filtro, de acordo com as influências externas (acelerações e interferências magnéticas) que são expectáveis, dependendo da localização onde se pretende colocar o dispositivo no corpo humano. O algoritmo desenvolvido permite a inclusão/exclusão de componentes, permitindo por isso liberdade de escolha para melhor satisfazer as necessidades das aplicações em redes de sensores sem fios. O método proposto foi comparado com outras soluções em termos de robustez a interferências e tempo de execução, apresentando também resultados positivos.

Palavras chave - posicionamento em ambiente interior, redes de sensores sem fios, potência de sinal recebido, efeito do corpo, modelo de propagação, navegação inercial pedestre, orientação, fusão sensorial.

Contents

List of Figures

List of Tables

Acronyms and Abbreviations

ADC	Analogue-to-Digital Conversion
AHRS	Attitude and Heading Reference System
AMR	Anisotropic Magneto-Resistance
AOA	Angle of Arrival
AP	Access Point
APIT	Approximate Point-In-Triangulation Test
ARW	Angle Random Walk
AVAR	Alan Variance
BNP	Body Not Present
BP	Body Present
CDF	Cumulative Distribution Function
CF	Complementary Filter
CLP	Closest Link Path loss
COG	Centre Of Gravity
COTS	Commercial Off-The-Shelf
CRLB	Cramer-Rao Lower Bound
CSMA/CA	Carrier Sense Multiple Access/Collision Avoidance
DGPS	Differential GPS
DMA	Direct Memory Access
DR	Dead Reckoning
DWCL	Distance WCL
EKF	Extended Kalman Filter
FF	Foot-Flat
FFD	Full Function Device
FIFO	First-In-First-Out
FQA	Factored Quaternion Algorithm
FSM	Finite State Machine
GDA	Gradient Decent Algorithm
GDOP	Geometric Dilution of Precision
GNA	Gauss-Newton Algorithm
GPS	Global Positioning System
GSM	Groupe Spécial Mobile

HO	Heel-Off
HS	Heel-Strike
I/O	Input/Output
I^2C	Inter-Integrated Circuit
IEEE	Institute of Electrical and Electronic Engineers
IKF	Indirect Kalman Filter
IMMU	Inertial and Magnetic Measurement Unit
IMU	Inertial Measurement Unit
IMU	Inertial Measurement Unit
INS	Inertial Navigation System
IoT	Internet of Things
IR	Infrared
KF	Kalman Filter
KNN	K-Nearest Neighbour
LBS	Location-Based Services
LLS	Linear Least Squares
LORAN	Long Range Navigation
LOS	Line-of-Sight
LP	Lower Peak
LPZC	Lower Peak Zero Crossing
LQI	Link Quality Indication
LR-WPAN	Low Rate-Wireless Personal Area Network
LS	Least Squares
LSB	Least Significant Bit
MAC	Medium Access Control
MAC	Medium Access Control
MARG	Magnetic, Angular-Rate and Gravity
ME	Mean Error
MEMS	Micro-Electro-Mechanical System
MMW	Millimetre Wave
MS	Mid-Stance
MSW	Mid-Swing
NLOS	Non-Line-of-Sight
NN	Nearest Neighbour
PC	Personal Computer

PDF	Probability Distribution Function
PDR	Pedestrian Dead Reckoning
PLE	Path Loss Exponent
PS	Positioning System
RADAR	Radio Detection and Ranging
RAM	Random Access Memory
RF	Radio Frequency
RFD	Reduced Function Device
RFID	Radio Frequency Identification
RI	Radio Interferometry
RIPS	Radio Interferometric Positioning System
RSS	Received Signal Strength
RWCL	Received signal strength WCL
SCP	Static Centre Position
SD	Step/Stride Detection
SDC	Secure Digital Card
SFD	Start of Frame Delimiter
SHORAN	Short Range Navigation
SHS	Step/Stride and Heading System
SL	Step/Stride Length
SNR	Signal to Noise Ratio
SoC	System-on-Chip
SPI	Serial Peripheral Interface
SRIPS	Stochastic RIPS
STD	Standard Deviation
STRIPS	Space-Time RIPS
SW	Swing
TDOA	Time Difference of Arrival
TO	Toe-Off
TOA	Time of Arrival
TTD	Total Travelled Distance
TVO	Two-Vector Observation
UKF	Unscented Kalman Filter
ULA	Uniform Linear Array
UP	Upper Peak

UPZC	Upper Peak Zero Crossing
US	Ultrasound
USART	Universal Synchronous Asynchronous Receiver Transmitter
UWB	Ultra-Wideband
WAAS	Wide Area Augmentation System
WCL	Weighted Centroid Localization
WKNN	Weighted KNN
WLAN	Wireless Local Area Network
WSN	Wireless Sensor Network
ZAU	Zero Angular-rate Update
ZC	Zero Crossing
ZVU	Zero Velocity Update

Chapter 1

Introduction

Positioning technologies are ubiquitous nowadays, with position information being increasingly used to provide contextual feedback to applications. Location information of users enables applications to provide context-based information of interest, such as waypoints, commodities and services available nearby. This is the basis of location-based services (LBS), and this type of service is available mainly in outdoor environments, where the global positioning system (GPS) is capable of offering an adequate quality of service to the majority of applications. Companies such as Google, Microsoft and Nokia have undertaken an enormous effort in order to create detailed maps of outdoor environments. This enabled updated information of roads, streets, door numbers, and all types of services, from restaurants to shopping malls and gas stations, are available in every device with an Internet connection. Only recently has this mapping effort started to address indoor environments, with indoor maps from Google being available to users by late 2011.

Indoor positioning is currently available in some countries, where a few proprietary solutions targeted at very specific applications exist, such as finding shelf products in a supermarket or navigating in large business areas. Several companies are engaged in pushing indoor localization systems to the market [1]. These companies can be roughly divided into two categories: map providers, such as Apple, Google, Nokia and Micello; and positioning

system providers including Apple, Google, Indoor Atlas, Pole Star, Shopkick, Aeroscout, Ekahau, Zebra Tech and Aisle411. Indoor positioning system solutions are mainly based on technologies such as WLAN (wireless local area network), radio frequency identification (RFID) and ultra-wideband (UWB).

Under a worldwide perspective, indoor positioning is generally unavailable to users. It is a challenging task due to the variety of different situations that can arise inside buildings. From the type of walls to the objects that can be found in an indoor environment, the coexistence with other systems and the users themselves, all these elements interfere with position calculation. Under this type of environment, GPS is not reliable due to the signal attenuation from the lack of line-of-sight (LOS) to GPS satellites.

UWB is a technology with potential to solve the problem of indoor positioning due to its high accuracy when inferring distances between devices [2]. UWB enables ranging capabilities between devices and allows the detection of multipath components of transmitted signals by using large channel bandwidths. Accuracies in the sub-meter range can be achieved with this technology. Yet, due to the existence of two versions of UWB standard competing among each other, a pulsed version and a frequency division version, standard acceptance has been very slow. Furthermore, the ranging capability feature is optional, not obligating manufacturers to implement it in order to comply with the standard. Due to the slow standard acceptance, there isn't yet a mass market in place, which in turn affects device cost for currently available off-the-shelf components. The inclusion of UWB in IEEE 802.15.4 standard [3] as a low power physical layer is a step towards faster industry acceptance, due to the popularity of 802.15.4 and its network and application layer protocol ZigBee. Since no particular solution has yet proven to be reliable, cost efficient and of generic application for every situation, a *de facto* standard has not yet been achieved. This lack of standard is also explained by the defragmentation seen in current indoor positioning solutions, which are typically proprietary, closed and non-compatible systems.

The Internet of things (IoT) is another application area that can greatly benefit from indoor localization services. IoT is a vision consisting of a world where a large number of common objects used in a daily basis are imbued with computational and communication capabilities, efficiently automating innumerous tasks [4]. There are several institutions working in order to achieve this vision, not only in the form of standards creation and improvement, but also in the interaction between different standards, so a global network

augmented by these objects can be realized [5]. Sensor networks have a central role in this ubiquitous computing vision, since they provide the connection to the real world through sensors and actuators. A plethora of different sensors can be applied to the most diverse scenarios and the information generated by these sensors can be used to increase process efficiency or to achieve higher understanding of a certain phenomenon.

The terms IoT and ubiquitous computing, along with other terms such as ambient intelligence, pervasive computing and smart objects are related and sometimes used interchangeably in literature. A common feature shared between these visions, directly related to the data sensed from these smart objects, is the location from where the data is collected. Sensor information is commonly referred to as context, and since location information is also user-sensitive context information, they complement each other. As such, positioning technologies are key enablers for the ubiquitous computing vision due to the application opportunities that arise with the knowledge of the position of the user or device. Wireless sensor networks (WSNs) are a major component of the ubiquitous computing vision; therefore indoor positioning in WSNs is also a key component for the IoT vision.

A node in a WSN is a sensing capable device composed by a microcontroller and a wireless transceiver. WSN constraints relate to device cost, energy and computational capabilities, the latter of which trades-off with higher battery recharge frequencies. Due to typical WSN energy consumption and computational capacity constraints, low complexity positioning solutions are desired. Low power requirements are a common feature associated with WSN, which in turn is addressed in part by relaxing the computational capabilities of these devices.

Positioning capability in WSNs brings spatial information to the data obtained from sensors. The position information can be used in the most various contexts, from geodesic routing to antenna beam forming, or to detect soil temperature and pinpoint the origin of a wildfire. Positioning in WSNs can be accomplished by using optical, acoustic or radio frequency (RF) technologies, to produce range, angle or pattern information. Using one of these measurements, or a combination of them, the location of a device can be computed. Received signal strength (RSS) based positioning is a popular approach in WSNs since no additional hardware is needed to implement this type of localization system. RSS positioning stands as a fast and inexpensive method to obtain the location of a device in a WSN, with accuracies spanning from 3 to 10 meters. This approach is also attractive due to the low power

consumption profile that sensor nodes are usually subject to. The small cost of sending or receiving radio messages to compute location is usually preferable than the increased costs (in terms of price, size and energy) of adding extra hardware to the positioning solution. RSS based positioning is accomplished by either using a propagation model to convert RSS to distance or by using the RSS measure itself as proximity estimate.

The achievable accuracy by a positioning system is also very important and limits the applications in which a positioning system can be used. For example, while an accuracy of 100 meters is sufficient for a ship navigating at sea to find its way across the ocean, such accuracy would be useless when driving a car along a road. Higher accuracy is generally desired, yet different applications require different minimum accuracies to be achieved. With higher accuracy, RSS positioning could deliver the quality of service necessary for a wider range of IoT applications.

Low power consumption is a typical requirement in WSNs, since nodes are usually battery operated. A WSN node is capable of RSS positioning without the addition of extra hardware, thus not incurring in additional energy consumption. Coexistence with other systems, objects and environment is an important aspect of positioning systems. Coexistence with the users in RSS positioning is especially important due to the body influence in RSS readings.

Recently, hybrid-positioning systems fusing information from multiple localization techniques and sensors have gained popularity within the scientific community. When a localization system fuses position information from multiple sources, high computational capabilities are necessary in order to produce higher accuracy position estimates in real-time, using the typical Kalman, Bayesian or particle filter implementations. The low power, low computational profiles of WSN are incompatible with this approach. As such, a balance between accuracy and computational complexity must be achieved in order to implement hybrid-positioning algorithms in low cost WSN.

1.1 Evolution of Positioning Systems

Positioning and navigation are an integral part of human nature, since our survival depended on the ability to find the way to shelter or food sources in the early ages of mankind. References or landmarks served the purpose of positioning and helped to identify important locations, such as the Stonehenge (3100 BC), which conveyed religious

significance to the location, or the Easter Island Statues (1680 BC), which symbolize social status of local tribe members. These landmarks not only served the local populations, they would also later be transposed to maps, facilitating navigation to anyone that ventured to these locations [6].

In maritime navigation, early sailors such as the Polynesian tribes did not have maps, and as such they observed the surrounding nature for references, such as the species of birds and fish and their migrations, the sky and the sea. The invention of the compass dates back to the Han Dynasty (204 BC) and the first Chinese navigators began to use the compass (1040 AC) to establish sea routes, using the stars to find their positions. The compass would later be perfected by the Europeans, along with a number of instruments created to aid maritime navigation, such as the back staff, the cross staff, the kamal, the mariner's astrolabe, the quadrant, the octant and the sextant. These instruments were used to measure altitude, angle (which would later be known as latitude) and to determine the distance from the Earth's poles. Earth mapping using latitude and longitude coordinates was envisioned by Roger Bacon (1267 AC) in his work *Opus Majus*. A great leap in maritime navigation occurred when timekeeping was introduced by means of the sand hourglass and later the mechanical marine chronometers, which allowed navigators to find the longitude coordinate, which in conjunction with the latitude pinpointed the exact location of a vessel at sea. Timekeeping also brought with it the first forms of dead reckoning (DR), where navigation was accomplished by following charts containing compass orientations, keeping track of direction, speed and time spent on each heading. The accuracy of the position estimate was closely tied to the accuracy of timekeeping, with both evolving over time [6]. DR is reliable over short distances since, apart from measurement errors, it is also dependent on other factors (such as wind speeds and currents), which affect the estimation of distance traveled.

Air navigation was partly accomplished using the instruments and techniques discovered and perfected in the maritime navigation. Yet, due to the time to compute a position fix and the harsh conditions aboard an airplane, many of the methods used before were impracticable in the aircraft context. As such, improvements in the sextant led to the bubble sextant, which allowed its use without visibility to the horizon. The first radio systems from the late 19th century also enabled direction finding by means of directional antennas. At the time, precise aerial navigation, especially in long-range flights, required careful coordination using astronavigation, DR and radio direction finding techniques. The evolution of timekeeping, namely from mechanical based timekeeping (accuracy of seconds) to

frequency based timekeeping (accuracy of microseconds) yet again revolutionized the process of navigation. This improvement, along with the discovery of radio waves theorized by Maxwell and demonstrated by Hertz, paved way for the radio detection and ranging (RADAR) system, enabling the detection of obstacles, their distances and speeds due to the reflection of radio signals and the Doppler effect. RADAR also enabled mapping of landforms while airborne.

Military applications were the main driver for air navigation systems, with several hyperbolic navigation systems being implemented during World War I and World War II. By finding the time difference between signals from different base stations, and with the help of hyperbolic charts, a position fix could be achieved. Among these systems are GEE, DECCA, LORAN (Long Range Navigation) and SHORAN (Short Range Navigation). Positioning computers started to replace the navigator's job aboard military aircrafts in the early 1950s, by combining astronavigation systems with inertial navigation units.

Navigation in air, land or at sea can generally be treated as a two-dimensional problem, where the altitude or depth is treated as a separate dimension. Space exploration brought with it the need to find the position in three dimensions, with the added complexity of the much larger distances to travel. Inertial navigation evolved during this time, with laser gyroscopes and atomic clock precision, yet it was mainly used as a fallback system when communications with Earth were not possible. Tracking was accomplished by base stations situated in strategic points on Earth, which measured the time-of-flight of radio signals travelling to the probe. Transit [7], the first satellite navigation system, emerged during the space exploration age, and it was based on the Doppler effect. Using control stations on Earth, the position of the satellite was known. A device that received the radio signal from a satellite would be able to find its relative velocity. With the information of the satellites position, a position fix for the device was possible, with accuracy of 200 meters. By implementing passive systems, neither scalability nor privacy was an issue, and it was made available to serve both military and civilian purposes. A subsequent iteration of the satellite navigation system, based on the time of arrival of radio signals, would replace Transit and come to be known as GPS, combining atomic clock sources and a constellation of at least 24 satellites covering the entire globe. Further enhancements to GPS include the wide area augmentation system (WAAS) and the differential GPS (DGPS), which further improve GPS accuracy to the sub-meter range.

Clearly satellite based systems such as the GPS play a crucial role in societies nowadays. Its evolution and dissemination has been constantly growing, due to the advantages that it brings, and the increasing efficiency in the most diverse fields, both civilian (from transportation to agriculture) and military (from tactical soldiers deployment to guiding a missile to its target). While an enormous effort has been made in perfecting outdoor positioning, only recently indoor positioning has begun to receive attention of the research community.

1.2 Motivation and Objectives

In outdoor environments, GPS is the standard positioning system and is capable of offering good quality of service to the majority of applications. However, in indoor environment, GPS cannot be used due to the high attenuation of satellite signals when not in LOS. Another issue associated with GPS is energy consumption. The integration of these devices in WSN is prohibitive due to the low power profile associated with these networks.

Indoor positioning systems can be implemented in the most varied contexts, such as in hospitals, to locate equipment and guide patients to necessary resources, or in large public areas like museums, to guide tourists. Such a system can also be used in a gymnasium to indicate which machine a user should go next to proceed with his training, in a conference venue to find a specific presentation, or to monitor and prevent theft. Security and privacy issues are very important in positioning systems, since users may not want to be locatable in a specific location or interval in time. This information is therefore very user-sensitive and can influence directly in the acceptance of the systems [8].

The market of indoor positioning is expected to have an exponential growth in the near future, according to several reports [9], [10]. Many use cases have been envisioned, where new location based services connect users to products, services and to other users, in ways never seen before. Yet, due to the lack of a universal indoor positioning technology that addresses every important aspect such as cost, efficiency, accuracy, availability, security and privacy above all, the boom that was expected to have already happened is still yet to come.

Several implementations of indoor positioning systems exist. Some take advantage of existing infrastructures such as WLAN, while others use magnetic variances across a building or special beacons with ranging capabilities. Fingerprinting based solutions (also known as map matching) using WLAN or magnetic variance, depend on an offline phase where data

from the location is collected and compiled into a database. This is a sensible and cumbersome task, which influences the systems final accuracy. Furthermore, when changes occur in the environment, the database information collected needs to be rebuilt to reflect the new environmental changes. On the other hand, solutions that use special beacons need an infrastructure of their own, which implies additional costs to implement positioning capabilities.

The study, development and test of an indoor positioning system for WSN is proposed in this work. The system combines two independent methods of position estimation, in order to maximize accuracy. Since low power is an important characteristic, RSS will be used as basis for position estimation, to which an inertial measurement unit (IMU) is added. The latter typically uses filters that require high computation capabilities (e.g., Kalman filters). Therefore we seek to adapt this system to WSN, relaxing computation requirements using simplified filtering techniques. A generic implementation of a positioning system without limiting its application to a specific area (such as sports, healthcare or assisted living) is desired; as such, we explored the achievable accuracy with current off-the-shelf components and assessed their integration in order to increase overall accuracy. The indoor positioning system is integrated into a body posture monitoring system which also uses an IMU to find the orientation of each body segment [11]. The following objectives are pursued:

- Study of a relative positioning approach, having in consideration the body posture monitoring system, which allows the determination of the orientation of each user within radio range.
- Implementation and characterization of a positioning system based on RSS.
- Study and implementation of dead reckoning techniques to improve system accuracy. These techniques make use of an inertial measurement unit. Since low power is a requirement of WSN, relaxed computational filters are pursued and implemented.
- Individual testing of the positioning capabilities of each technique. Evaluation of performance individually and also combining both RSS and DR techniques, having in mind the possible detection of improvements to implement.

1.3 Thesis Outline

The remainder of this thesis is organized as follows: Chapters 2 and 3 present the state-of-the-art regarding positioning technologies, systems and algorithms, WSN positioning, DR and sensor fusion. Chapter 4 reviews the hardware platform and methods used to implement and test the RSS-based positioning solutions proposed. Chapter 5 studies, implements and tests modifications to RSS-based positioning, having in account the body-induced effects. Chapter 6 studies, implements and tests an inertial navigation system applied to the user's body. Chapter 7 presents the conclusions and future work.

1.4 References

[1] K. Searl, 'Top 33 Indoor Location-Based Services (LBS) Companies in the US', *Technavio*, 2014. [Online]. Available: http://www.technavio.com/blog/top-33-indoor-location-based-services-lbs-companies-in-the-us.

[2] E. Karapistoli, F.-N. Pavlidou, I. Gragopoulos, and I. Tsetsinas, 'An overview of the IEEE 802.15.4a Standard', *IEEE Communications Magazine*, vol. 48, no. 1, pp. 47–53, Jan. 2010.

[3] IEEE, 'Standard for Local and metropolitan area networks - Part 15.4: Low-Rate Wireless Personal Area Networks (LR-WPANs)', 2011.

[4] M. Weiser, 'The computer for the 21st century', *Scientific american*, vol. 3, no. 3, pp. 94–104, 1991.

[5] L. Atzori, A. Iera, and G. Morabito, 'The Internet of Things: A survey', *Computer Networks*, vol. 54, no. 15, pp. 2787–2805, Oct. 2010.

[6] A. K. Johnston, R. D. Connor, C. E. Stephens, and P. E. Ceruzzi, *Time and Navigation: The Untold Story of Getting from Here to There*. Washington, D.C.: Smithsonian Books, 2015.

[7] R. J. Danchik, 'An overview of transit development', *Johns Hopkins APL Technical Digest (Applied Physics Laboratory)*, vol. 19, no. 1, pp. 18–26, 1998.

[8] Y. Gu, A. Lo, and I. Niemegeers, 'A survey of indoor positioning systems for wireless personal networks', *Communications Surveys & Tutorials, IEEE*, vol. 11, no. 1, pp. 13–32, 2009.

[9] IDTechEx, 'Mobile Phone Indoor Positioning Systems (IPS) and Real Time Locating Systems (RTLS) 2014-2024', 2015. [Online]. Available: http://www.idtechex.com/research/reports/mobile-phone-indoor-positioning-systems-ips-and-real-time-locating-systems-rtls-2014-2024-000359.asp.

[10] Marketsandmarkets.com, 'Indoor Location Market by Solution (Tag-based, RF-based, Sensor-based), by Application (Indoor Maps & Navigation, Indoor Location-based Analytics, Tracking & Tracing, Monitoring & Emergency Management), by Service, by Vertical, & by Region - Global Foreca', 2014. [Online]. Available: http://www.marketsandmarkets.com/Market-Reports/indoor-positioning-navigation-ipin-market-989.html.

[11] H. D. Silva, P. Macedo, J. A. Afonso, and L. A. Rocha, 'Design and implementation of a wireless sensor network applied to motion capture', *1st Portuguese Conference on Wireless Sensor Networks (CNRS 2011)*, Coimbra, Portugal, 2011.

Chapter 2

Positioning Systems and Algorithms in Wireless Sensor Networks

A wireless sensor network (WSN) consists of small, low-cost, resource-constrained devices equipped with sensing and communication capabilities, with the ability to form ad-hoc networks in order to sense the environment. The WSN employed in this work is a low rate-wireless personal area network (LR-WPAN), which, according to the definition presented by the IEEE 802.15.4 standard, is “a simple, low-cost communication network that allows wireless connectivity in applications with limited power and relaxed throughput requirements” whose main objectives are “ease of installation, reliable data transfer, short-range operation, extremely low cost and reasonable battery life” [1]. Low power requirements are common in these networks, since nodes are battery operated and longer operation times are desirable.

A WSN is generally composed of two node types, which in IEEE 802.15.4 terminology are called full function devices (FFD) and reduced function devices (RFD). The

FFDs, apart from sensing tasks, can serve as network coordinators, facilitating message exchange between other nodes and other networks to which they have access. RFDs, on the other hand, are nodes that cannot be assigned this network management task, and their sole purpose is to collect data from the environment. This data can be pre-processed by the node prior to its transmission, and the resulting information can be used in order to act on the environment if needed (e.g., averaging temperature readings from a sensor and using this information to control room temperature to a specified level). FFDs and RFDs are also known as sink and source nodes respectively, since RFD nodes typically are the source generating data for the sink to process or relay to other entities. These networks can operate in star topology, where all nodes relay messages to a central node, or peer-to-peer topology, where every FFD can communicate with other FFD. In both topologies, RFDs can only communicate with a FFD to relay messages. Figure 2.1 exemplifies the topologies described in [1].

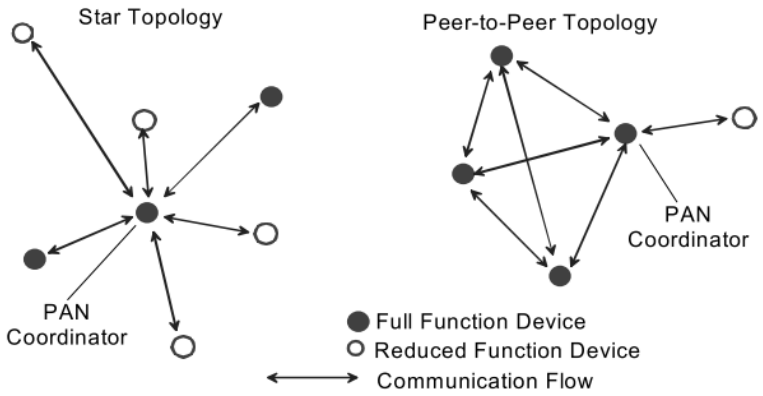

Figure 2.1: Star and Peer-to-peer topology examples [1]

A sensor node is a battery-operated device composed by a microprocessor, memory, a radio interface and a sensor interface. Microprocessors used in WSNs are generally low power and have low computation capabilities (8 bit microprocessors are common), running at frequencies in the order of tens of megahertz. The memory available is usually also limited, in the range of kilobytes. A wide range of sensors can be employed to sense data, which is transmitted to other entities through the radio interface.

Low power requirements are often achieved by careful coordination of the necessary hardware for the task at hand. The microprocessor can be put in a sleep state or a specific sensor can be turned off for a certain amount of time before it is used again. The radio interface, which is typically the component that exhibits higher power consumption, can be turned off to save energy during periods when communications are not needed. Low power

requirements are also addressed at the medium access control (MAC) protocol level, with beaconed networks implementing idle times and guaranteed time slots for dedicated transmissions, which avoid wasting precious machine cycles of high power consumption while running contention access algorithms. Depending on data throughput and computation load, these mechanisms allow the extension of operation time for months of uninterrupted operation on a single coin cell battery.

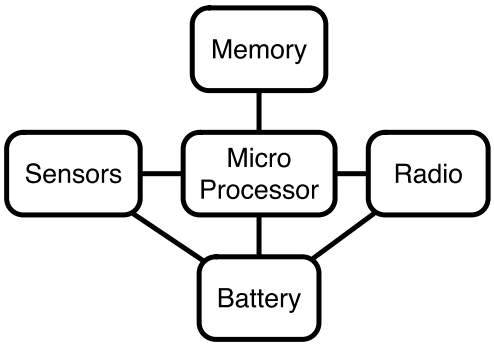

Figure 2.2: Sensor Node Architecture.

A positioning system (PS) allows the determination of the spatial location of an entity (user or device), using measurements collected from the environment. Knowledge of the position of sensor nodes enables a wide range of applications, from tracking to event monitoring and routing control.

2.1 Positioning System Taxonomy

Taxonomies abound when classifying PSs. In [2], systems are classified into exact and approximate positioning, where the first is based on precise measurements of distances or angles between sensor nodes and reference nodes (also known as anchor nodes), incurring in extensive calculations and high network traffic; and the latter allows relaxed calculations, producing estimates with lower accuracy, but exhibiting lower network traffic.

The work in [3] classifies systems as: relative or absolute PSs, according to the type of position estimation produced; and autonomous-based or infrastructure-based positioning, depending on whether the node itself or an external resource computes the location, which exposes privacy and bottleneck issues and highlights the balance between computation costs and network overhead. The autonomous or infrastructure-based concepts are extended in [4] with the direct and indirect methods, where the entity that computes the location shares it with the device or external resource and vice-versa. The authors in [5] refer to this classification as

centralized or distributed positioning methods, and provide further classifications. Distributed methods are classified as either anchor-based or anchor-free, where in anchor based systems, anchors are deployed with the knowledge or with the ability to determine their own position autonomously, while in anchor-free methods, nodes compute their positions relative to other nodes in communication range. Anchor-based methods are yet again further classified into range-based and range-free methods, which are defined as the exact and approximate positioning methods from [2]. Figure 2.3 presents an overview of the taxonomies described.

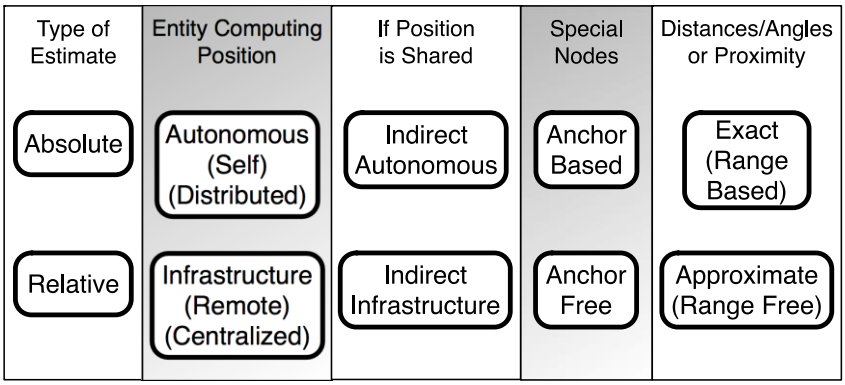

Figure 2.3: Classification of positioning methods in WSN.

In [6] PSs are classified according to the signals used to collect measurements, which can be infrared (IR), ultrasound (US), radio frequency (RF), vision-based and acoustic.

2.2 Performance Metrics in Positioning Systems

Performance metrics present the basis of comparison among algorithms [7]. The performance metric that is most commonly emphasized in PSs is accuracy, which is generally measured as the mean Euclidean distance between the estimated position and the true position. Precision measures the consistency of results obtained when positions are estimated and, along with accuracy, a cumulative distribution function (CDF) is usually presented, denoting a given accuracy for a specific percentage of position estimates (e.g., an accuracy of 3.2 m with 90% probability).

The area of coverage of a system is the designated area where the PS is expected to provide service. It can be a single room, an entire building, a city or worldwide coverage. In [3], scale is defined as the area per unit of infrastructure and number of objects within this area that the system can locate. Adding more infrastructure units increases the area of coverage.

Positioning frequency is an important metric for applications such as navigation in real-time. Higher frequencies imply higher computational costs, which lead to higher energy consumption. The complexity of a positioning solution limits positioning frequency, along with sensor sample rate and microprocessor frequency when estimates are computed autonomously. When estimates are computed by the infrastructure, the limit is imposed by the network latency (bit rate, bit error rate and medium access mechanisms and number of hops) along with the time the server takes to compute the estimate. As pointed out in [7], positioning frequency is an important indicator of complexity.

The cost metric can be related to energy and computational costs, but also related to the infrastructure, the positioning device and installation or maintenance of a PS. A low power positioning solution can decrease the costs associated with rechargeable batteries and reduce computation capability requirements associated with the microprocessor.

Security and privacy are metrics highly sensitive to users, since the whereabouts of a person are often desired to remain private and in full control of the user.

If a PS is to be used by a large number of users, scalability issues can arise, especially when resources are shared among users (e.g., a server which computes location of devices). Devices that compute the location estimate autonomously, such as GPS devices, avoid this kind of issue.

Robustness is the ability to cope with erroneous or absent measurement information. If the PS is a hybrid solution between different positioning technologies, robustness is also related to the seamless integration of all technologies involved, where in the advent of failure from one positioning technology, the system should be able to cope with this issue and be able to produce position estimates.

The accuracy and precision metrics are a result of the positioning measurements and algorithms used to compute position estimates. Range-based measurements are also known as geometric measurements, since they build on geometric shapes to estimate parameters such as distances or angles.

2.3 Overview of Range-Based Measurements and Algorithms

Time of arrival (TOA), received signal strength (RSS) and angle of arrival (AOA) are the most common measurement types used in PSs. TOA and RSS are most commonly found in WSNs. Despite the AOA measurement being a well-known technique, it is the least common type in WSNs. Each type offers distinct performance metrics in terms of cost, energy consumption, accuracy and precision.

An important aspect in PSs is the error associated with the employed measurement type. The Cramer-Rao lower bound (CRLB) is often used to characterize the achievable precision using a specific measurement method. This bound on variance can be seen as the best possible precision a certain positioning algorithm can achieve. As such, this enables algorithms to be benchmarked, according to how close the positioning estimate is to the best precision possible [8]. In the simplest case where the parameter to be estimated is a scalar, the bound is given by:

$$\sigma_{\hat{\theta}}^2 \geq \frac{1}{-E\left[\frac{\partial^2}{\partial\theta^2}\ln[p(X;\theta)]\right]} \tag{2.1}$$

where $\hat{\theta}$ is an estimator of the true parameter θ (which could be, for example, a distance or an angle), E is the expected value operator, p is the probability distribution function (PDF) associated with the random measurement X. The PDF is derived from the respective measurement model, reflecting the nature of the errors associated with each measurement type. Typically the noise present in the random measurement X is modelled through a zero-mean Gaussian random variable.

2.3.1 Angle-of-Arrival and Angulation

The AOA technique determines the angle between an anchor node and a sensor node. A directional antenna or an array antenna can be employed to determine the AOA of a signal by analysing the phase or amplitude difference received by each antenna element. AOA is also possible to be determined by analysing the phase or time difference of an ultrasound signal detected by multiple receivers [9], or by means of radio interferometry [10]. This special antenna usually increases node cost and is typically employed in anchor nodes, which

are usually in lesser number than sensor nodes. Figure 2.4 depicts an example of the angulation algorithm, using two AOA measurements.

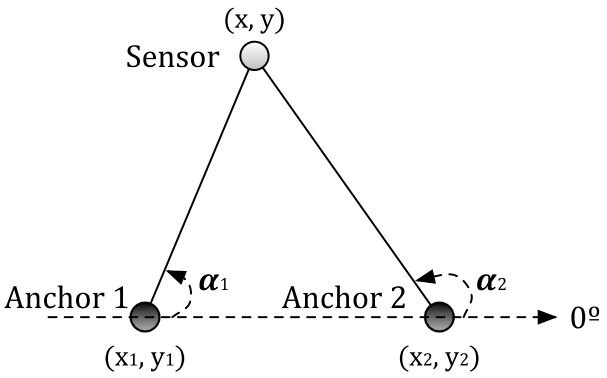

Figure 2.4: Angulation example with known anchor coordinates.

Given non-collinear locations among sensor and anchor nodes, two angle readings and known anchor node coordinates are sufficient to obtain a position estimate in 2D using angulation. The angles measured are given according to a reference orientation illustrated as the 0º direction in Figure 2.4, which could represent the orientation of the magnetic north (or true north). The angles and the coordinates of the sensor node and anchor nodes are related by equation (2.2) [11].

$$(x_i - x)\, sin\, \alpha_i = (y_i - y)\, cos\, \alpha_i \tag{2.2}$$

Using the linear least-squares (LLS) method, multiple measurements are rearranged into the matrix form $\boldsymbol{AX}=\boldsymbol{B}$, with $\boldsymbol{X}$ being the column vector containing the estimated sensor coordinates $[x, y]^T$, where:

$$\boldsymbol{A} = \begin{bmatrix} -\, sin\, \alpha_1 & cos\, \alpha_1 \\ \vdots & \vdots \\ -\, sin\, \alpha_n & cos\, \alpha_n \end{bmatrix} \tag{2.3}$$

and:

$$\boldsymbol{B} = \begin{bmatrix} y_1\, cos\, \alpha_1 - x_1\, sin\, \alpha_1 \\ \vdots \\ y_n\, cos\, \alpha_n - x_n\, sin\, \alpha_n \end{bmatrix} \tag{2.4}$$

According to the LLS algorithm formulation, the solution is found using:

$$\boldsymbol{X} = (\boldsymbol{A^T A})^{-1} \boldsymbol{A^T B} \tag{2.5}$$

The LLS method is also a solution for data fusion when more than two measurements are available. It is important since this is a closed form method that minimizes a set of

observations and produces a result even when the angles sensed by the anchor nodes do not provide a unique intersection point due to noise factors that influence the process.

The CRLB provides intuition on the achievable limit for AOA measurement systems. Considering a uniform linear array (ULA) with N_a elements, such limit is presented in [12] as:

$$\sqrt{Var(\psi)} = \frac{\sqrt{3}c}{\sqrt{2}\pi\sqrt{SNR}\beta\Delta\sqrt{N_a(N_a^2-1)}\,sin\,\psi} \tag{2.6}$$

where ψ is the AOA estimate, c the speed of light, *SNR* the signal-to-noise-ratio for each element, β the effective bandwidth and Δ the spacing between elements. Since small antennas are desirable for WSN applications, increasing Δ is not usually an option. Precision of the AOA measurement increases with higher SNR, signal bandwidth and number of elements. The best precision is also obtained when the antenna is perpendicular to the signal direction. The precision of the angle estimate will depend on directivity of the antenna, multipath propagation and shadowing conditions [13]. When under non-line-of-sight (NLOS), the multipath components of the signal can induce very large errors, since they can arrive from an arbitrary angle.

A different approach is considered in [14], where anchor nodes are equipped with an array of antennas which create a rotating beacon signal using phase adjustments. Sensor nodes keep track of the time between the initial detection of the rotating beacon and its respective peak power, in order to find the angle to the anchor node.

The main challenge for AOA systems in WSN relates to hardware complexity, since nodes in a WSN are usually constrained by low power and low cost requirements. Balance between complexity and accuracy is very important, and since this balance is difficult to achieve in AOA systems, they are less common in WSN. Furthermore, AOA is usually applied in outdoor scenarios.

2.3.2 Time-of-Arrival and Lateration

The TOA technique produces distance estimates by keeping track of the time that a signal takes to travel from one point to another. The distances obtained for each anchor will narrow the location of the sensor node to a circumference with radius equal to the distance estimated. Given three non-collinear measurements, the intersection of the three

circumferences pinpoints the sensor location. Consider the 2D case positioning presented in Figure 2.5.

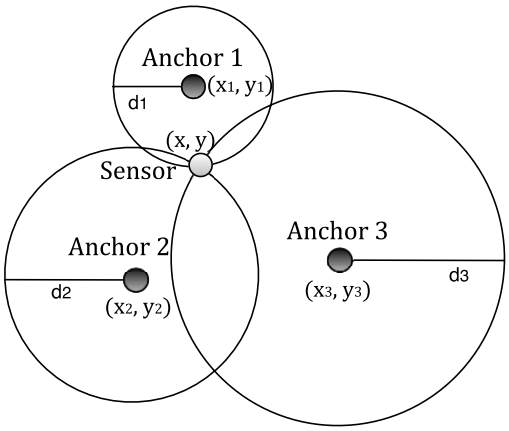

Figure 2.5: Lateration example with three anchor nodes.

The distances estimated for each anchor node are related by equation (2.7) [11].

$$(x_i - x)^2 + (y_i - y)^2 = d_i^2 \tag{2.7}$$

To find a solution to this system, first a linearization of the system of equations is obtained by subtracting the distance equation of the first anchor node from the other equations, which cancels the unknown squared terms.

$$x_i^2 + y_i^2 - x_1^2 - y_1^2 - 2x(x_i - x_1) - 2y(y_i - y_1) = d_i^2 - d_1^2 \tag{2.8}$$

A linear system of the form $\boldsymbol{AX=B}$ is obtained, which can also be solved using the LLS method from equation (2.5). The distance estimates can also be obtained by using a propagation model to convert RSS to distance, serving the result as inputs of the lateration algorithm. Detailed analysis of RSS systems is presented in section 2.4.

The CRLB for TOA measurements is presented in [12] as:

$$\sqrt{Var(\tau)} = \frac{1}{2\sqrt{2}\pi\sqrt{SNR}\beta} \tag{2.9}$$

where τ represents the TOA estimate, *SNR* is the signal-to-noise-ratio and β is the signal bandwidth. This result reflects the reason behind the high precision of UWB systems, since precision increases with higher signal bandwidths, which is precisely one of its features.

Clock synchronization is necessary in order to measure the TOA and the granularity of the clock sources must be several orders higher than the time interval being measured. In the

case of ultrasounds this issue is not as critical as with the speed of light, where an error of 1 nanosecond is equivalent to 30 cm distance error. The clock synchronization requirement can be removed if a two-way ranging procedure is employed, such as the one described in the IEEE 802.15.4a standard [15]. The clock accounting for time will always be the same, where an additional message exchange and cooperation of a second node is necessary. Another strategy that relieves nodes from clock synchronization is used in the Cricket system [16], where a RF and an ultrasound message are transmitted concurrently. As soon as the RF message is detected, a timer starts counting the time until the arrival of the ultrasound pulse. By neglecting the RF propagation time, which is much smaller than the ultrasound, the RF message itself is used as a synchronizing event. The speed of the traveling signal needs to be known *a priori*, and since the speed of sound depends on temperature, [17] also implements temperature adjustments by sensing the temperature in both nodes when performing the distance measurement.

NLOS conditions also introduce errors in the estimation, although with lesser impact than in the AOA case. UWB is a popular approach in TOA systems, since its large bandwidth and short pulse duration enables the detection of the various multipath components of the signal [13]. Algorithms and strategies to select which multipath component to use in the distance estimation process is an on-going research topic.

2.3.3 Time-Difference-of-Arrival and Hyperbolic Lateration

The time-difference-of-arrival (TDOA) measurement is similar to the TOA and is typically used for tracking a target emitting a signal, where instead of measuring the time from a single anchor node, a time difference is measured from two anchor nodes simultaneously. This determines the position of the tracked sensor node on two hyperbolas with foci centred at the anchor nodes. Individual measurements of TOA from each of the anchor nodes can be tagged with a timestamp and relayed to the node computing the position estimation [5], [13]. Clock synchronization between anchor nodes is implicit; nonetheless relieving the sensor node from the synchronization task, which happened in the case of TOA. Three anchors are necessary to estimate the position of a sensor node in 2D using TDOA measurements.

Consider the example presented in Figure 2.6. The TDOA is a measurement of time, which when multiplied by the propagation velocity will yield the difference in distances [18].

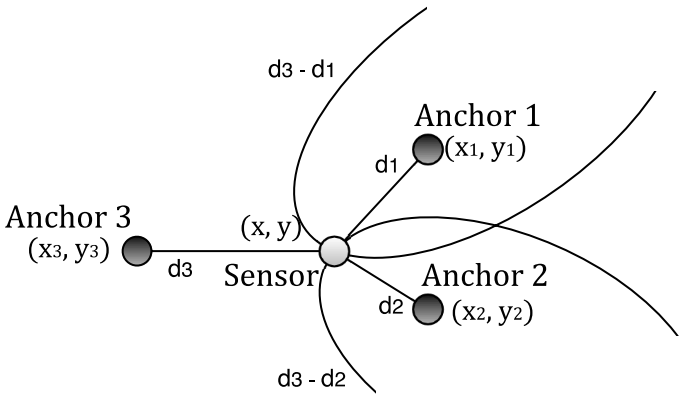

Figure 2.6: Hyperbolic lateration example with three anchor nodes.

Using anchor 3 as reference for this example, the measurements depicted in Figure 2.6 produce an equation of the form [11]:

$$d_{3,n}{}^2 + 2d_{3,n}d_n = x_n^2 + y_n^2 - x_1^2 - y_1^2 - 2x(x_n - x_3) - 2y(y_n - y_3) \quad (2.10)$$

A system of the form $\boldsymbol{AX=B}$ is obtained, where $\boldsymbol{X}$ includes the coordinates of the sensor node and the distance $d_{3,}$ since it is also an unknown. The solution can be found using equation (2.5).

In [19] the CRLB for TDOA is investigated, where it is concluded that it cannot perform better than TOA case. As such, bandwidth and SNR are two key parameters to improve precision in this type of system.

Similar to the TOA case, the synchronization requirement can be removed under certain conditions. Although not adequate to WSNs, using acoustic signals and recording these signals, the method described in [20] removes the synchronization requirement by emitting a second signal, a known time interval after receiving the first signal. The same concept of second signal transmission with known offset is used in [21].

2.3.4 Radio Interferometry

Determining the position using radio interferometry (RI) technique can be accomplished by using the readily available RSS indication present in commercial off-the-shelf (COTS) devices to measure the phase difference of two radio signals. This phase difference is then used to determine distance between nodes. RI stems from the same principles governing optical interferometry, and it is of interest since it is able to achieve high accuracy and long range simultaneously [22]. The method was first applied to WSN

localization in the RIPS (radio-interferometric positioning system) [23] where two anchor nodes emit pure sinusoids at slightly different frequencies, creating a compound signal envelope with low frequency, that can be measured using the RSS indicator. Consider Figure 2.7 as an example.

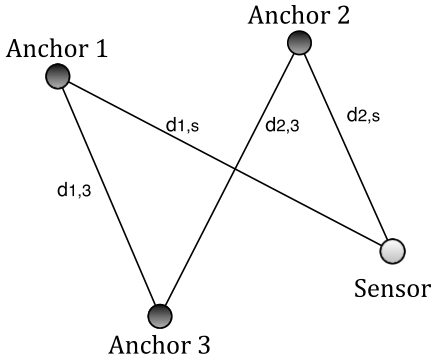

Figure 2.7: Interferometry ranging example.

Anchor 1 and 2 transmit pure sinusoids synchronized in time, while anchor 3 and the sensor node receive the resulting signal by sampling the RSS indicator. A low-pass filter is applied to the RSS signal in order to remove the high frequency components. Assuming the two sinusoidal signal frequencies are lesser than 2 kHz apart, and the distances between the two emitters and two receivers is smaller than 1 km (100 m is the usual range for WSN radios), the resulting signal's relative phase offset is related to the distance between the receiving nodes by equation (2.11) [23].

$$\vartheta_1 - \vartheta_2 = 2\pi\left(\frac{d_{1,s} - d_{1,3} + d_{2,3} - d_{2,s}}{c/f}\right), (mod\ 2\pi) \tag{2.11}$$

The phase difference between the signals is directly related to the carrier frequency f and the distance between the transmitting and the receiving nodes. By collecting multiple measurements between nodes in the network, the phase ambiguity can be removed. In [23] a broadcast message sent by one of the sender nodes serves as synchronizing event for each participating node, after which local timers are used to keep time synchronization. The calibration of the radios to the specific frequency follows, after which both senders start to transmit the pure sinusoids. This method achieves an accuracy of 5 cm in an area of 18 m by 18 m, with a latency of 80 minutes, due to multiple combinations of sender/receiving nodes in a 16-node network.

Authors in [24] present SRIPS (stochastic RIPS) using the 2.4 GHz frequency band. SRIPS eliminates the calibration phase of [23] by employing a stochastic approach and improve the time taken to perform a single measurement, which reduces the time to compute a position estimate to around 10 minutes.

The application of RIPS and SRIPS is not suitable for indoor environments due to multipath propagation effects. To tackle indoor environments, authors in [25] propose space-time RIPS (STRIPS), which uses a millimetre wave (MMW) system operating in the 60 GHz frequency band employing space-time coding, although only simulation results are presented.

2.4 RSS-Based Indoor Positioning Systems

RSS systems are known for the low reliability when inferring distances from measurements. Filtering techniques are a solution for dealing with RSS reliability under noisy environment conditions. These techniques also stand as the common solution for integration of heterogeneous PSs, in order to provide more accurate location estimation. Kalman filters [26] and particle filters [27] are the usual approaches; however, since these solutions need high computational capacity, they are usually not compatible with WSNs. Instead, filtering is typically accomplished by averaging multiple measurements, thus positioning accuracy is sacrificed in the trade-off for lower computational demands, longer lifespan of sensor nodes and faster positioning update rates when desired. Hybrid positioning techniques are a popular research topic in WSN, due to devices combining a radio interface along with sensing capabilities. Data is gathered from several sensors and fused with RSS positioning techniques in order to improve accuracy [28]–[30].

Map matching, range-free positioning and range-based positioning are the main methods used to locate nodes in PSs based on RSS. Map matching systems are a popular approach in RSS positioning in wireless local area networks (WLANs), which uses already deployed network infrastructure without needing additional components. Range-free positioning uses radio parameters such as link quality indication (LQI), RSS or node connectivity to infer proximity to a certain known reference point. Range-based systems use RSS readings as input for propagation models that estimate distances between devices in a network.

2.4.1 Propagation Models

Distance inference through signal attenuation use propagation models that depend heavily on the environment where the system is implemented. Some propagation models are better for indoor settings while others are more appropriate for outdoors environment. A general overview of various propagation models can be found in [31].

Several efforts have been made to characterize radio signal propagation during the GSM (Groupe Spécial Mobile) system's evolution, through the COST 231 project [32]. For indoor settings, the one-slope [33] and the multiwall [34] propagation models are frequently used in the state-of-the-art. The one-slope equation is defined in (2.12).

$$RSS_{OS}(d) = RSS(d_0) - 10 \times n \times log\left(\frac{d}{d_0}\right) + \chi_\sigma \tag{2.12}$$

The parameter $RSS(d_0)$ is the RSS at the reference distance d_0 (usually 1 meter), n is the path loss exponent (PLE) and χ_σ is a Gaussian distributed random variable with zero-mean and environment dependent variance. The multiwall model is defined in equation (2.13).

$$RSS_{MW}(d) = RSS_{OS}(d) - \sum k_i \times Att_i \tag{2.13}$$

The multiwall model uses the one-slope model attenuation and includes the effect from walls obstructing LOS communication between devices. The parameter k_i represents the number of walls of type i, and Att_i the respective attenuation value for type of wall i.

These propagation models typically model the large-scale effects of signal attenuation. The main error source comes from the small-scale fading effect, which is the fast variation that occurs in a short time period. This effect happens when the environment changes or when the antennas are moved by a fraction of the wavelength. Multipath waves combine at the receiver in slightly different time instants, giving rise to a signal that can largely vary in amplitude and phase [35]. Small-scale fading is usually modelled through a Gaussian random variable as in equation (2.12).

A typical approach used to obtain the values of the propagation model parameters is to apply linear regression techniques on data collected from a specific site. Least squares method can be applied to obtain values for the PLE parameter. A PLE of 2 is the reference path loss used in free space propagation. Authors in [36], [37] obtained PLE values above 2, which is

typical in non-line of sight (NLOS) or reflection dominated environments. Values below 2 are less frequent, but are sometimes found in literature [34].

The propagation model method stands as a fast and cost efficient way to obtain an estimate of distance between nodes in a network. The main disadvantage is the low accuracy in indoor environment. When devices are worn near or on the human body, propagation models performance further degrades. Attenuations as high as 15 dB due to human body are reported when compared to the line-of-sight (LOS) case [38], thus affecting distance inference. Authors in [38] argue that models accounting for the impact of the human body might be developed, using exponential interpolation from data collected in test measurements. Body orientation is of extreme importance when accounting for body attenuation factor, yet a system that incorporates the body effect is seldom seen in the literature.

2.4.2 Map Matching

Radio propagation complexity is addressed in map matching by collecting empirical data from the location were the PS is to be implemented. This data is later used to find the position of a node. Two phases compose the system originally implemented by Bahl et al. [39]. In the offline phase, data relating position and RSS from access points (APs) is gathered from the site into a database, in order to create a radio map. In the online phase, mobile nodes report to a server the RSS from APs in range. The server compares the mobile node readings to the radio map signatures so a match (or the closest to) can be found, thus pinpointing the mobile node's position. Equation (2.14) is used in the search for the smallest distance in signal space.

$$D_{ss} = \left[\sum_{i=1}^{N} \left|R_{Map}(i) - R_s(i)\right|^p\right]^{\frac{1}{p}} \tag{2.14}$$

The parameter N is the number of anchor nodes in range, $R_{Map}(i)$ is the RSS stored for anchor i in a calibration point of the radio map, $R_s(i)$ is the RSS sampled in the online phase for anchor i and p is the norm used, e.g., for p = 2, the signal space distance is the Euclidean distance between the calibration point and the mobile node's RSS reading. Equation (2.14) is computed for all calibration points and the nearest neighbour (NN), which is the calibration point that produces the smallest D_{ss}, is assumed as the position of the mobile node. A variant of this method is to find K NNs (KNN) instead of a single NN, averaging the coordinates of the K points to produce the position estimate. In [40] the KNNs are weighted

by the inverse of the distance in signal space (WKNN), improving the position estimates. The WKNN position estimate is obtained using equation (2.15):

$$\widehat{\boldsymbol{x}} = \frac{\sum_{i=1}^{K} w_i \cdot \boldsymbol{P_i}(x,y)}{\sum_{i=1}^{K} w_i}; w_i = \frac{1}{D_i} \tag{2.15}$$

with P_i being the coordinates (x and y in the 2D case) of each of the K calibration points found during the search. The purpose is to weight heavier the readings that are closer to the calibration points collected during the offline phase. If the same weight were given to all neighbours, a simple average would be obtained from the K calibration points closest to the reading.

Apart from the centralized approach, the disadvantage of map matching is that changes in the environment after the radio map has been built will affect the positioning accuracy. A comprehensive study on fingerprinting is presented in [41]. Authors conclude that map density translates to higher accuracy with a nonlinear behaviour in increasing the number of calibration points. The direction faced when collecting samples, also studied by Bahl et al., is crucial and greatly improves system accuracy. However, even though positioning algorithms in map matching search through a database of calibration points taken in different body orientations, these algorithms do not account for the direction the user is facing when an RSS sample is collected during the online phase. The use of sensors capable of producing orientation information (such as magnetic or gyroscope sensors) could bring accuracy improvements to these systems.

The radio map creation is a cumbersome task when a large area is to be mapped, or when the density of calibration points is high. Approaches to facilitate the creation of a radio map in the offline phase have been conducted. Authors in [37] use propagation models to ease the process of radio map database creation, and consequently, adapting to changes in the environment through recalculation of the database. Another solution to the map creation phase is to use ray-tracing modelling to obtain the attenuation values of signal propagation [42].

2.4.3 Range-Free Positioning

The range-free positioning method involves determining the proximity when a device or object is near a known location. Examples of technologies used in this method include physical contact detection by means of a sensor or monitoring wireless access points. In WSNs, this method is used typically under high node density.

The weighted centroid localization (WCL) method [43] is a well-known, low complexity algorithm with good robustness to noise that can be used along with any kind of metric that reflects proximity or distance between nodes. Bulusu et al. implemented this method in [44], where node connectivity was the metric used to infer distance. Given a set of beacon nodes in the network possessing knowledge of their location, the position of sensor nodes can be estimated by calculating the centroid of all beacon node coordinates for which the sensor is in range of. The main advantage of WCL derives from its simplicity, since the position estimate depends only on the number of anchor nodes in communication range. The position estimate is calculated using equation (2.16):

$$\widehat{\boldsymbol{x}} = \frac{\sum_{i=1}^{B} w_i \cdot \boldsymbol{L_i}(x,y)}{\sum_{i=1}^{B} w_i}; w_i = \left|\frac{1}{(R_p)^e}\right| \tag{2.16}$$

where $\boldsymbol{L}_i$ are the coordinates of each anchor node and R_p is the radio parameter used to calculate the weight. The exponent e allows an adjustment of the importance of the weight applied to each anchor node's R_p parameter.

In [45], authors compare the LLS method against centroid-based algorithms. Results show that the centroid-based method outperforms the LLS method in precision and accuracy with lower complexity, when under an environment strongly affected by multipath propagation.

LANDMARC [46] uses RSS readings in their approximate positioning method. Tag readers report RSS from moving RFID tags, along with RSS from reference tags. Reference tags are fixed and their RSS are used as means of comparison between that of the movable tags to infer proximity. In analogy to the Map Matching solution, the reference tags role is similar to the radio map in section 2.4.2. As such, an equation identical to equation (2.15) is used to find the position of a tracked tag, where the weight used is defined in equation (2.17):

$$w_i = \frac{1/E_i^2}{\sum_{i=1}^{k} E_i^2} \tag{2.17}$$

where E_i is equal to the distance in signal space from equation (2.14), using $p = 2$. In spite of the 1-meter accuracy attained by their method, the time to determine position of movable tags is incompatible with real time positioning. In a more recent work [47], authors further improve LANDMARC's positioning error. Although their system has faster update rate than original LANDMARC, tags have a signal reporting cycle of 2 seconds, which is still incompatible with many real time positioning scenarios.

The approximate point-in-triangulation test (APIT) algorithm [48], despite not being designed as an indoor system, could also be used in such conditions. In APIT a sensor node chooses three anchors that are in communication range and tests whether it is located inside the triangular area formed by the anchor nodes. The test is repeated for other combinations of anchor nodes, and the final position estimate is given as the centre of gravity (COG) of the intersection of all triangles in which the sensor node found itself to be located. Only simulation results are presented, from which it is concluded that APIT is more susceptible to node density than WCL.

The work in [49] implements improvements to the WCL algorithm by adjusting weights based on an adjusted LQI scheme. The feasibility of this method could be an issue under real WSN implementations, since the IEEE 802.15.4 standard [1] only requires this 8 bit parameter to be modelled with at least eight unique values in the range from 0 to 255. In addition, the simulations presented in [49] implement the LQI value as a function of distance, when the LQI value is essentially a function of SNR and bit error rate. For example, the Texas Instruments CC2530 datasheet [50] recommends the implementation of LQI using a correlation measurement between the start of frame delimiter (SFD) and the first eight symbols of an incoming packet, along with two parameters (offset and slope) derived from empirical measurements of packet error ratio. The LQI can also be a function of the RSS, in which case no additional information could be derived from the LQI that is not already mapped in the RSS.

Network-based positioning algorithms such as DV-Hop [51] can use the RSS as a metric to infer distance for each hop. Error is reduced in comparison with using hop information only. In [52], authors achieve less than 10% radio coverage error when using RSS measurements between hops. In contrast, authors in [53] discard a RSS solution due to its low reliability. These contradictory opinions are strongly related to the use case scenario of each positioning system implementation. The RSS positioning is a common first approach to localization in WSN, yet if care is not taken to account for the environment and/or body influence, performance may degrade significantly.

2.5 Issues in RSS Positioning Systems

The accuracy of the methods described in the previous section is directly related to RF propagation, depending on features like the topology of a building, construction materials,

objects, furniture and number of persons inside a room. When propagation models are used, the PLE is usually considered fixed for a specific scenario. This is also one of the main problems, since the PLE is a key parameter in distance estimation that varies with position and environment changes [54]. According to [55] a fixed environment-dependent PLE generally has smaller variance compared to the dynamic PLE obtained through an estimation process, which demonstrates the random nature associated with the propagation environment.

PLE estimation suffers from multipath and shadowing effects, which are the main sources of error in RSS-based PSs, especially in indoor environments. Multipath happens when the radio wave travels the propagation medium interacting with objects along the way, suffering attenuation, reflection, scattering and diffraction [56]. Multiple copies of the signal arrive at the receiver with different attenuations, delays and phase-shifts, which are added constructively or destructively depending on each signal phase. The multipath effect depends on the number of objects, dimensions and dielectric material properties present in the signal's propagation path. This effect is also commonly termed small-scale effect or fast fading [57], due to the fast RSS variations over small distances (in the order of the wavelength).

Shadowing happens when the radio wave travels through different obstacles or mediums, suffering attenuation in the process [35]. Shadowing and path loss (the gradual decay of signal power along distance) are also called large-scale effects or slow fading, due to the slower RSS variations over greater distances. These large-scale effects are always present whether static or dynamic scenarios are considered. For greater distances between transmitter and receiver, the probability of the signal encountering a greater number of objects is also higher, thus it is common to find in literature increasing variances for higher distances between devices.

Ray-tracing techniques are a common tool used in network planning and deployment, in order to determine efficient device placement in a building [58]. This type of tool can generate a map of radio propagation, which can be used in producing more accurate distance estimates. Due to the dynamics of indoor environments, it is unfeasible to have a radio map being constantly updated by a ray-tracing algorithm and deployed to devices in a particular room.

RSS dependence on the environment is what makes indoor positioning a challenging task, due to the accuracy of the position estimate being a function of so many variables, which can vary widely from one indoor scenario to another. In practice, since indoor propagation

environment complexity is very high, an empirical model such as the one-slope model from equation (2.12) is used extensively [56]. It is a simple model that captures the essence of the signal decay with distance. Note that by using a constant power at the reference distance, the transmission power is implicitly assumed as constant.

In [19], [59], theoretical precision bounds are studied for RSS positioning, which for a single RSS reading are given by equation (2.18):

$$\sqrt{Var(d)} \geq \frac{\sigma d \, ln\, 10}{10 \cdot n \cdot} \tag{2.18}$$

where d is the distance between transmitter and receiver, n is the PLE and σ is the standard deviation of the shadowing effect from equation (2.12). This theoretical framework allows insight over the properties that affect precision. From equation (2.18) we can denote that the RSS variance increases with the distance, such as reported in [8], [18], [43], [60]–[62] and decreases with increasing values of the path loss exponent n, such as observed in [63]. The bound itself may be unachievable yet it serves as an overall precision mark that positioning algorithms can be compared to.

In practical situations, indoor conditions and the proximity of the user's body significantly hinder the propagation model's correlation with distance. Furthermore, RSS variance only occurs when the environment is dynamic, e.g., when any surrounding objects or transmitter and receiver devices are moved. When every object and both the transmitter and receiver devices are static, the multipath effect does not change in time, and the RSS is given by the sum of all copies of the original signal that the receiver can detect. For example, a receiver placed 10 meters away from a transmitter will experience the same RSS variance as when a distance of 2 meters separates the receiver and transmitter, which stands in direct conflict with the CRLB in equation (2.18). This variance property is what enables tomographic radio imaging systems to track user movements inside buildings [64]. Since the variance of the signal is null under static conditions, averaging over time will not influence the outcome of the positioning error. This implies that the RSS received by the device in static conditions is constant, and is a function of multipath and shadowing effects that are occurring in a given instant. When the user moves or the environment changes (e.g., a door opens), these multipath and shadowing effects also change, thus the RSS variance is both position and environment dependent.

The effect of the body on the propagation conditions is an important topic for communications systems deployment and performance assessment. The proximity of the human body is an important factor that induces bias in the position estimation, with attenuations as high as 15 dB under NLOS conditions [38]. When the user's body blocks the LOS transmission between two devices, a part of the wave travels through the body (shadow fading occurs) while the remaining wave energy is absorbed, reflected, diffracted and scattered. These attenuation effects directly influence RSS positioning algorithms since the RSS is used to infer distance or proximity.

Some works attempt to model the body effect in the antenna using the super-antenna concept referred in [65], which is directly related to shadowing caused by the proximity of the body. In this model, the body is considered as an integral part of the antenna, contributing to the radiation diagram. Besides radiation pattern, factors such as transmission power and radio frequency also play an important role [66].

The sparse anchor problem [53] is also an issue for localization algorithms in WSN since a minimum number of anchors are needed to provide a location estimate. If enough anchors are available, the positioning estimate is also dependent on the anchor placement in the field. This problem is known as geometric dilution of precision (GDOP) and happens when anchor locations are collinear [15].

The work presented in [67], where a model of relative antenna gain versus rotation is inferred from measurements, also considers body effects. This antenna gain model is used in conjunction with an inertial model, which assumes the orientation of the user is the same as the orientation of its velocity vector. In [38] the body effect is characterized in terms of the location of the sensor node (pocket or necklace), contact time and effective bandwidth between sensor nodes both in indoor and outdoor environments. The work in [68] encountered variations of up to 30 dB when the source is located from 0 cm to 10 cm off the body. Body posture and antenna placement in the user's body is analysed in [69], where the body movement is of utmost importance for the communications performance.

2.6 References

[1] IEEE, 'IEEE Standard Part 15.4: Wireless MAC and PHY Specifications for Low-Rate WPANs', 2006.

[2] J. Blumenthal, F. Reichenbach, and D. Timmermann, 'Position Estimation in Ad hoc Wireless Sensor Networks with Low Complexity', *PROCEEDINGS OF THE 2nd WORKSHOP ON POSITIONING, NAVIGATION AND COMMUNICATION (WPNC'05) & 1st ULTRA-WIDEBAND EXPERT TALK (UET'05)*, pp. 41–50, 2005.

[3] J. Hightower and G. Borriello, 'A Survey and Taxonomy of Location Systems for Ubiquitous Computing', Seattle, 2001.

[4] M. Vossiek, L. Wiebking, P. Gulden, J. Wieghardt, C. Hoffmann, and P. Heide, 'Wireless local positioning', *Microwave Magazine, IEEE*, vol. 4, no. 4, pp. 77–86, 2003.

[5] R. Dagher and R. Quilez, 'Localization in Wireless Sensor Networks', in *Wireless Sensor and Robot Networks: From Topology Control to Communication Aspects*, N. Mitton and D. Simplot-Ryl, Eds. Worldscientific, 2014, pp. 203–247.

[6] Y. Gu, A. Lo, and I. Niemegeers, 'A survey of indoor positioning systems for wireless personal networks', *Communications Surveys & Tutorials, IEEE*, vol. 11, no. 1, pp. 13–32, 2009.

[7] H. Liu, S. Member, H. Darabi, P. Banerjee, and J. Liu, 'Survey of Wireless Indoor Positioning Techniques and Systems', *IEEE TRANSACTIONS ON SYSTEMS, MAN, AND CYBERNETICS—PART C: APPLICATIONS AND REVIEWS*, vol. 37, no. 6, pp. 1067–1080, 2007.

[8] N. Patwari, J. N. Ash, S. Kyperountas, A. O. Hero, R. L. Moses, and N. S. Correal, 'Locating the nodes: cooperative localization in wireless sensor networks', *IEEE Signal Processing Magazine*, vol. 22, no. 4, pp. 54–69, Jul. 2005.

[9] N. B. Priyantha, A. K. L. Miu, H. Balakrishnan, and S. Teller, 'The cricket compass for context-aware mobile applications', *Proceedings of the 7th annual international conference on Mobile computing and networking - MobiCom '01*, no. July, pp. 1–14, 2001.

[10] I. Amundson, J. Sallai, X. Koutsoukos, and A. Ledeczi, 'Radio interferometric angle of arrival estimation', *Lecture Notes in Computer Science (including subseries Lecture*

Notes in Artificial Intelligence and Lecture Notes in Bioinformatics), vol. 5970 LNCS, pp. 1–16, 2010.

[11] J. Figueiras and S. Frattasi, *Mobile Positioning and Tracking: From Conventional to Cooperative Techniques*. Jon Wiley and Sons, 2010.

[12] S. Gezici, 'A Survey on Wireless Position Estimation', *Wireless Personal Communications*, vol. 44, no. 3, pp. 263–282, Oct. 2007.

[13] G. Mao, B. Fidan, and B. D. O. Anderson, 'Wireless sensor network localization techniques', *Computer Networks*, vol. 51, pp. 2529–2553, 2007.

[14] P. Kułakowski, J. Vales-Alonso, E. Egea-López, W. Ludwin, and J. García-Haro, 'Angle-of-arrival localization based on antenna arrays for wireless sensor networks', *Computers & Electrical Engineering*, vol. 36, no. 6, pp. 1181–1186, 2010.

[15] IEEE, 'IEEE Std 802.15.4a-2007: Wireless MAC and PHY Specifications for LR-WPANs - Amendment 1: Add Alternate PHYs', 2007.

[16] N. B. Priyantha, A. Chakraborty, and H. Balakrishnan, 'The Cricket Location-Support System', in *Proceedings of the 6th ACM International Conference on Mobile Computing and Networking (ACM MOBICOM)*, 2000, vol. 2000, no. August.

[17] N. B. Priyantha, 'The Cricket Indoor Location System', Massachusetts Institute of Technology, 2005.

[18] C. Gentile, N. Alsindi, R. Raulefs, and C. Teolis, *Geolocation Techniques*. Springer, 2013.

[19] Y. Qi, 'Wireless Geolocation in a Non-Line-of-Sight Environment', Princeton University, 2003.

[20] B. Xu, G. Sun, R. Yu, and Z. Yang, 'High-accuracy TDOA-based localization without time synchronization', *IEEE Transactions on Parallel and Distributed Systems*, vol. 24, no. 8, pp. 1567–1576, 2013.

[21] S. He, X. Dong, and S. Member, 'Asynchronous Time Difference of Arrival Positioning System', pp. 1–28.

[22] S. Szilvasi, P. Volgyesi, J. Sallai, A. Ledeczi, and M. Maroti, 'Interferometry in Wireless Sensor Networks', in *Interferometry - Research and Applications in Science and Technology*, InTech, 2012.

[23] M. Maróti, B. Kusy, G. Balogh, P. Volgyesi, A. Nádas, K. Molnar, S. Dóra, and Á. Lédeczi, 'Radio Interferometric Geolocation', in *SenSys'05*, 2005, pp. 1–12.

[24] B. J. Dil and P. J. M. Havinga, 'Stochastic radio interferometric positioning in the 2.4 GHz range', *Proceedings of the 9th ACM Conference on Embedded Networked Sensor Systems - SenSys '11*, p. 108, 2011.

[25] M. Shinotsuka, Y. Wang, X. Ma, and G. T. Zhou, 'Designing radio interferometric positioning systems for indoor localizations in millimeter wave bands', in *2014 48th Asilomar Conference on Signals, Systems and Computers*, 2014, pp. 1184–1188.

[26] G. Glanzer, T. Bernoulli, T. Wiessflecker, and U. Walder, 'Semi-autonomous indoor positioning using MEMS-based inertial measurement units and building information', *2009 6th Workshop on Positioning, Navigation and Communication*, vol. 2009, pp. 135–139, Mar. 2009.

[27] H. Wang, H. Lenz, A. Szabo, J. Bamberger, and U. D. Hanebeck, 'WLAN-Based Pedestrian Tracking Using Particle Filters and Low-Cost MEMS Sensors', *2007 4th Workshop on Positioning, Navigation and Communication*, vol. 2007, pp. 1–7, Mar. 2007.

[28] R. C. Luo, O. Chen, and C. W. Lin, 'Indoor Human Monitoring System Using Wireless and Pyroelectric Sensory Fusion System', in *The 2010 IEEE/RSJ International Conference on Intelligent Robots and Systems*, 2010, pp. 1507–1512.

[29] P. Tarrío, M. Cesana, and A. Redondi, 'Energy-accuracy trade-offs for hybrid localization using RSS and inertial measurements in wireless sensor networks', *Ad Hoc Networks*, vol. 11, no. 6, pp. 1874–1889, Aug. 2013.

[30] T. Gadeke, J. Schmid, W. Stork, and K. D. Muller-Glaser, 'Pedestrian Dead Reckoning for Person Localization in a Wireless Sensor Network', in *International Conference on Indoor Positioning and Indoor Navigation*, 2011, no. September.

[31] I. Forkel and M. Salzmann, 'Radio Propagation Modelling and its Application for 3G Mobile Network Simulation', *10th Aachen Symposium on Signal Theory*, pp. 363–375, 2001.

[32] E. Damosso and L. M. Correia, 'Cost Action 231: Digital Mobile Radio Towards Future Generation Systems, Final Report.', 1999.

[33] Z. Zhang, G. Wan, M. Jiang, and G. Yang, 'Research of An Adjacent Correction Positioning Algorithm Based on RSSI-Distance Measurement', in *2011 Eighth International Conference on Fuzzy Systems and Knowledge Discovery (FSKD)*, 2011, pp. 2319–2323.

[34] S.-Y. Yeong, W. Al-Salihy, and T.-C. Wan, 'Indoor WLAN Monitoring and Planning Using Empirical and Theoretical Propagation Models', in *2010 Second International Conference on Network Applications Protocols and Services*, 2010, pp. 165–169.

[35] T. S. Rappaport, *Wireless Communications: Principles and Practice*. Englewood Cliffs, New Jersey: Prentice-Hall, 1996.

[36] L. C. Liechty, E. Reifsnider, and G. Durgin, 'Developing the Best 2 . 4 GHz Propagation Model from Active Network Measurements', in *IEEE 66th Vehicular Technology Conference*, 2007, no. 404, pp. 894–896.

[37] P. Mestre, C. Serodio, L. Coutinho, L. Reigoto, and J. Matias, 'Hybrid technique for fingerprinting using IEEE802.11 wireless networks', in *2011 International Conference on Indoor Positioning and Indoor Navigation, IPIN*, 2011, no. September, pp. 1–7.

[38] E. Miluzzo, X. Zheng, K. Fodor, and A. T. Campbell, 'Radio Characterization of 802.15.4 and Its Impact on the Design of Mobile Sensor Networks', in *5th European Conf. on Wireless Sensor Networks (EWSN '08)*, 2008, pp. 171–188.

[39] P. Bahl and V. N. Padmanabhan, 'RADAR: An In-building RF-based User Location and Tracking System', in *INFOCOM 2000. Nineteenth Annual Joint Conference of the*

IEEE Computer and Communications Societies. Proceedings. IEEE, 2000, vol. 2, pp. 775 – 784 vol.2.

[40] B. Li, J. Salter, and A. Dempster, 'Indoor positioning techniques based on wireless LAN', in *LAN, FIRST IEEE INTERNATIONAL CONFERENCE ON WIRELESS BROADBAND AND ULTRA WIDEBAND COMMUNICATIONS*, 2006, pp. 13 – 16.

[41] V. Honkavirta, T. Perala, S. Ali-Loytty, and R. Piche, 'A comparative survey of WLAN location fingerprinting methods', in *2009 6th Workshop on Positioning, Navigation and Communication*, 2009, vol. 2009, pp. 243–251.

[42] A. V. Bosisio, 'Performances of an RSSI-based positioning and tracking algorithm', in *2011 International Conference on Indoor Positioning and Indoor Navigation, IPIN 2011*, 2011, pp. 1–8.

[43] F. Reichenbach and D. Timmermann, 'Indoor Localization with Low Complexity in Wireless Sensor Networks', *2006 IEEE International Conference on Industrial Informatics*, pp. 1018–1023, Aug. 2006.

[44] N. Bulusu, J. Heidemann, and D. Estrin, 'GPS-less low-cost outdoor localization for very small devices', *Personal Communications, IEEE*, vol. 7, no. 5, pp. 28–34, 2000.

[45] A. Fink and H. Beikirch, 'Analysis of RSS-based Location Estimation Techniques in Fading Environments', in *International Conference on Indoor Positioning and Indoor Navigation*, 2011, no. SEPTEMBER.

[46] L. M. Ni, Y. Liu, Y. C. Lau, and A. P. Patil, 'LANDMARC: Indoor Location Sensing Using Active RFID', *Wireless Networks*, vol. 10, no. 6, pp. 701–710, Nov. 2004.

[47] X. Yinggang, K. Jiaoli, W. Zhiliang, and Z. Shanshan, 'Indoor location technology and its applications base on improved LANDMARC algorithm', in *Proceedings of the 2011 Chinese Control and Decision Conference, CCDC 2011*, 2011, no. 2, pp. 2453–2458.

[48] T. He, C. Huang, B. M. Blum, J. a. Stankovic, and T. Abdelzaher, 'Range-free localization schemes for large scale sensor networks', *Proceedings of the 9th annual international conference on Mobile computing and networking - MobiCom '03*, p. 81, 2003.

[49] R. Behnke and D. Timmermann, 'AWCL: Adaptive Weighted Centroid Localization as an efficient improvement of coarse grained localization', *2008 5th Workshop on Positioning, Navigation and Communication*, pp. 243–250, Mar. 2008.

[50] T. Instruments, 'CC253x System-on-Chip Solution for 2.4-GHz IEEE 802.15.4 and ZigBee® Applications', 2012.

[51] S. Tian, X. Zhang, P. Liu, P. Sun, and X. Wang, 'A RSSI-Based DV-Hop Algorithm for Wireless Sensor Networks', *2007 International Conference on Wireless Communications, Networking and Mobile Computing*, pp. 2555–2558, Sep. 2007.

[52] R. Nagpal, H. Shrobe, and J. Bachrach, 'Organizing a Global Coordinate System from Local Information on an Ad Hoc Sensor Network', in *Proceedings of the 2nd international conference on Information processing in sensor networks*, 2003, pp. 333–348.

[53] C. Savarese, J. Rabaey, and K. Langendoen, 'Robust Positioning Algorithms for Distributed Ad-Hoc Wireless Sensor Networks', in *ATEC '02 Proceedings of the General Track of the annual conference on USENIX Annual Technical Conference*, 2002, pp. 317–327.

[54] M. B. Zeytinci, V. Sari, F. K. Harmanci, E. Anarim, and M. Akar, 'Location estimation using RSS measurements with unknown path loss exponents', *EURASIP Journal on Wireless Communications and Networking*, pp. 1–14, 2013.

[55] M. Veletić and M. Šunjevarić, 'On the Cramer-Rao lower bound for RSS-based positioning in wireless cellular networks', *AEU - International Journal of Electronics and Communications*, vol. 68, no. 8, pp. 730–736, Aug. 2014.

[56] M. Kochlan and J. Micek, 'Indoor Propagation of 2.4 GHz Radio Signal: Propagation Models and Experimental Results', in *The 10th International Conference on Digital Technologies*, 2014, pp. 125–129.

[57] A. Goldsmith, *Wireless Communications*. Cambridge University Press, 2005.

[58] M. F. Iskander, 'Propagation prediction models for wireless communication systems', *IEEE Transactions on Microwave Theory and Techniques*, vol. 50, no. 3, pp. 662–673, Mar. 2002.

[59] S. Mazuelas, A. Bahillo, R. M. Lorenzo, P. Fernandez, F. a. Lago, E. Garcia, J. Blas, and E. J. Abril, 'Robust Indoor Positioning Provided by Real-Time RSSI Values in Unmodified WLAN Networks', *IEEE Journal of Selected Topics in Signal Processing*, vol. 3, no. 5, pp. 821–831, Oct. 2009.

[60] D. Sanchez, M. a. Quintana, and J. L. Navarro, 'WLAN Location Determination Using Probability Distributions with Search Area Reduction via Trilateration', *2009 Fifth International Conference on Wireless and Mobile Communications*, no. 1, pp. 328–333, 2009.

[61] F. Della Rosa, L. Xu, H. Leppäkoski, and J. Nurmi, 'Relative Positioning of Mass Market Devices in Ad-hoc Networks', in *International Conference on Indoor Positioning and Indoor Navigation*, 2011, no. September.

[62] J. Palazon, J. Gozálvez, and G. Prieto, 'Experimental RSSI-based localization system using wireless sensor networks.', *17th IEEE International Conference on Emerging Technologies and Factory Automation*, 2012.

[63] H. Silva, J. Afonso, and L. Rocha, 'Experimental Performance Comparison of Indoor Positioning Algorithms Based on Received Signal Strength', in *Proceedings of the World Congress of Engineering*, 2014, vol. I, pp. 677–683.

[64] J. Wilson and N. Patwari, 'See Through Walls: Motion Tracking Using Variance-Based Radio Tomography Networks', *IEEE Transactions on Mobile Computing*, vol. 10, no. 5, pp. 612–621, 2011.

[65] F. Della Rosa, M. Pelosi, and J. Nurmi, 'Human-induced effects on RSS ranging measurements for cooperative positioning', *International Journal of Navigation and Observation*, vol. 2012, pp. 1–13, 2012.

[66] A. Awad, T. Frunzke, and F. Dressler, 'Adaptive Distance Estimation and Localization in WSN using RSSI Measures', in *10th Euromicro Conference on Digital System Design Architectures, Methods and Tools (DSD 2007)*, 2007, no. Dsd, pp. 471–478.

[67] G. V. Zàruba, M. Huber, F. a. Kamangar, and I. Chlamtac, 'Indoor location tracking using RSSI readings from a single Wi-Fi access point', *Wireless Networks*, vol. 13, no. 2, pp. 221–235, Jun. 2006.

[68] C. Oliveira and L. M. Correia, 'A Statistical Model to Characterize User Influence in Body Area Networks', *Vehicular Technology Conference Fall (VTC 2010-Fall), 2010 IEEE 72nd*. pp. 0–4, 2010.

[69] M. Mackowiak and L. Correia, 'Towards a Radio Channel Model for Off-Body Communications in a Multipath Environment', in *18th European Wireless Conference European Wireless*, 2012.

Chapter 3

Inertial Navigation Systems and Sensor Fusion

An inertial navigation system (INS) integrates position and orientation changes over time, in order to estimate the relative position and orientation since system start-up. This form of positioning is also known as dead reckoning (DR) and is used in many applications, including missile guidance, aircraft, spacecraft, ship and submarine navigation. An INS uses an inertial measurement unit (IMU) containing tri-axial accelerometers and gyroscopes. Other types of sensors are also commonly found, such as magnetic, temperature and pressure sensors. When the magnetic sensor is present, other common terminologies are used to refer to the IMU, such as inertial and magnetic measurement unit (IMMU) or magnetic, angular-rate and gravity (MARG) sensor. The IMU terminology is used in this work, making appropriate references to the specific sensors as needed.

Under ideal error-free measurements, an IMU would suffice in order to obtain a relative position estimate autonomously. Under such error conditions, a gyroscope when at rest could detect the Earth's rotation and find true north autonomously [1]. From a positioning system's perspective, this would be an ideal positioning method since it is self-contained

(does not require infrastructure) and could be used anywhere in the world. Since every measurement is always associated with an error, dealing with measurement errors in INSs is crucial, since errors will accumulate with each measurement update, causing drift of the position and orientation estimates. INSs can provide good estimates for short periods of time. When paired with other positioning solutions like global positioning system (GPS), the drift errors can be compensated. INSs and GPS systems complement each other, providing position estimates with higher accuracy, or improving system robustness during GPS signal outages [2].

3.1 Inertial and Magnetic Sensors

The evolution of micro-electro-mechanical system (MEMS) sensors enabled the application of INSs to the detection of human motion. The advantages of MEMS sensors are the small form factor, low cost, low power, lightweight, rugged construction, fast start-up time, low maintenance and high reliability characteristics [3]. The main disadvantage of MEMS sensors is the lower accuracy when compared to previous mechanical or fiber optic systems. Another disadvantage is that MEMS sensor output measurements in the body-frame (frame with origin in the sensor), while mechanical systems output measurements in the world-frame [3] (frame aligned with the vertical and the north direction on the Earth's surface). The body-frame measurements imply that additional calculations need to be performed in order to obtain the required world-frame measurements of interest. The gain in size, weight, lower power and reliability far surpass such disadvantage, which becomes negligible as computation capacity increases. Current smartphones for instance, contain all the sensors and computational capacity necessary for INS applications, enabling ubiquitous tracking of users movements.

A capacitive MEMS accelerometer can be described as a suspended proof mass. When this mass moves due to inertia (induced external forces or the gravitational force), the accelerometer's structure bend, acting like a spring. The displacement of the proof mass is detected by capacitance changes. The principle behind a MEMS accelerometer relates to Hooke's law and Newton's second law of motion:

$$F_H = F_N; k \cdot x = m \cdot a \tag{3.1}$$

where k is a constant factor characteristic of the spring, x is the displacement, m is the mass and a is the acceleration.

The MEMS gyroscope operating principle is based on the Coriolis force. The gyroscope can be described as a proof mass that is oscillating in a plane. When subject to a rotation with a rotation axis perpendicular to the oscillating plane, a Coriolis force appears:

$$\boldsymbol{F_C} = -2 \cdot m \cdot \boldsymbol{v} \times \boldsymbol{\omega} \tag{3.2}$$

where m is the mass, $\boldsymbol{v}$ is the velocity of the plane oscillations and $\boldsymbol{\omega}$ is the rotation. This force is then detected by means of capacitance changes.

Current MEMS magnetometers used in INS applications are mostly Hall effect or anisotropic magneto-resistance (AMR) sensor types. Hall effect magnetometers are based on the Lorentz force, which deflects the electrons traversing a conductor when a magnetic field perpendicular to the direction of the flow of electrons is applied. This results in a voltage between the planes of the conductor [4], which is proportional to:

$$V_H = \frac{R_H}{t} \cdot I \cdot B \tag{3.3}$$

where R_H is the Hall coefficient which depends on the conductor material, t is the conductor thickness, I is the current passing through the conductor and B is the magnetic field perpendicular to the conductor. AMR magnetometers use a thin film of ferromagnetic material where its resistance varies with the strength of the magnetic field applied in a specific direction. The resistance variation [4] is given by:

$$R_{AMR} = R_0 - \Delta R \sin^2 \alpha \tag{3.4}$$

where ΔR is the maximum resistance variation (in the order of 3%), R_0 is the resistance in a non-magnetic field and α is the angle of the magnetic field direction. These variations are detected typically using a Wheatstone bridge configuration.

These sensors suffer from the same sources of error: bias, white noise, bias stability, temperature effects, quantization, axis misalignments, scale factors and non-linearity [3]:

- Bias is the offset of the output to the true value. When integrated, causes an error that grows linearly with time.
- White noise is a random signal with frequency much higher than the sampling rate. It is modelled by a sequence of zero-mean uncorrelated random variables with finite variance. Random walk appears due to the integration of white noise, causing errors that grow proportionally to the square root of time.

- Bias stability, or 1/f noise, specifies how the bias of a device may change over time. This effect is usually observed at low frequencies and incurs in the same magnitude of errors as in the random walk case.
- Temperature affects the bias of the sensor and can be compensated with calibration. The compensation can be already embedded in the sensor for higher end devices containing an on-board temperature sensor. Temperature compensation for accelerometers is generally not necessary [1].
- Axis misalignments or cross-axis sensitivity occur when the sensing axis are not perfectly orthogonal. These effects are usually neglected since most sensors are assembled as three-axis units, which minimize misalignments.
- Scale factors influence the magnitude of the sensor output, incurring in bias errors when the sensor is undergoing rotation/acceleration.
- Non-linearity is the maximum deviation of the sensor output from an ideal linear fit, which is typically presented as a percentage of full-scale.
- Quantization errors are a consequence of analogue-to-digital conversion (ADC) and are usually considered as part of the non-linearity. The maximum quantization error is bounded to 0.5 LSB (least significant bit).

Sensor calibration minimizes the effects of scale factors, axis misalignments, initial biases, temperature compensation and non-linearity. A simple calibration method is used in [5]. Details of a rigorous calibration process can be found in [6], [7]. Magnetometer calibration involves compensating for distortions that are caused by components or objects placed near the sensor, which are subject to the same rotations as the sensor (e.g., components inside the same device). When the magnetic distortions are constant, the influence will appear as an offset in the measurements of each axis. This is known as hard iron effect and is caused by permanent magnets and magnetized iron or steel. When the magnetic distortion changes with the orientation of the device, the scale of the measurements will also change. This is known as soft iron effect and is caused by nearby ferrous materials such as nickel used in batteries [8].

Since the measurements from the MEMS magnetometer are not integrated over time, drift is not an issue. Sensing the Earth's magnetic field to perform heading measurements using magnetometers is heavily influenced by external magnetic distortions, especially in indoor environments.

The characterization of sensor noise is typically accomplished using the Allan variance (AVAR) test, which is a time domain analysis technique designed for characterizing noise and stability in clock systems [9]. This method identifies the different types of noises and their respective magnitudes affecting the system. A practical example on the application of this method is presented in [3]. A perfectly calibrated device will have a performance that depends only on bias stability and random walk. These parameters, obtained from the AVAR test, impose a maximum achievable limit in performance under optimal conditions. MEMS sensors performance is expected to improve along with improvements in the fabrication techniques, with lower prices due to large-scale production and integration on mass consumer products such as smartphones, tablets, smartwatches and wearable gadgets.

IMUs are often classified according to the bias stability that the embedded sensors achieve. Authors in [1] classify IMUs according to the grades presented in Table 3.1.

Table 3.1: IMU classification.

Grade	Gyroscope Bias	Accelerometer Bias
Military	0.005 º/h	< 30 μg
Navigation	0.01 º/h	50 μg
Tactical	1 º/h	1 mg
Consumer	> 1 º/h	> 1 mg

Low cost MEMS sensors are consumer grade level, for which calibration is a fundamental issue for its usability in INS applications. Even using high end consumer grade MEMS IMU, errors can exceed 100 meters after 1 minute of operation at 100 Hz sampling rate [3] due to gyroscope errors.

The INS task is to use IMU measurements to compute two estimates: changes in orientation and changes in displacement. INSs using DR method alone, as the only orientation/positioning method, will exhibit unbound errors over time. INSs coupled with other positioning methods will exhibit bounded errors. These errors are either bounded by the alternative positioning method or the bound is given as a percentage of the distance travelled. When applying INS to human motion, certain conditions can be identified and used in order to minimize the accumulated error. These conditions are discussed in section 3.5.1. The next section discusses DR.

3.2 Dead Reckoning

A strap-down INS performing DR positioning is a self-contained system that accounts for differences in orientation and displacement sensed with the help of gyroscope and accelerometer sensors. Orientation is a typical output of an INS and can be encoded using Euler angles, rotations matrices or quaternions. Quaternions are a popular alternative, as they do not suffer from singularities (also known as gimbal lock) that occur in Euler angles when two rotation axes are aligned. Compared to rotation matrices, quaternions only use four parameters instead of the nine required to encode rotations. Regarding computational efficiency, quaternion algebra requires fewer operations than the matrix counterpart, which is an advantage when implementing INS in resource constrained embedded devices. For these reasons, quaternions are adopted in this work. Figure 3.1 depicts a block diagram of the operations performed by an INS.

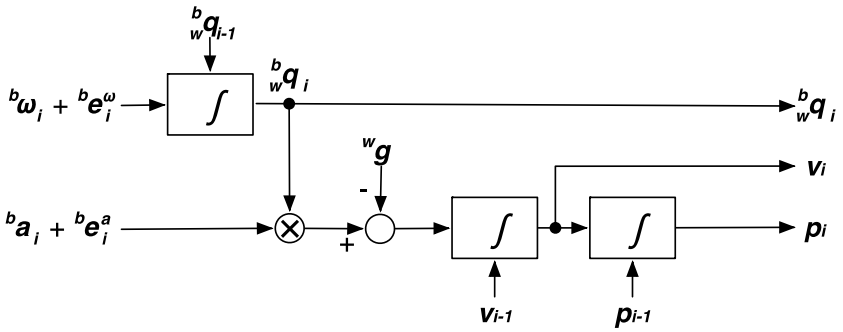

Figure 3.1: Orientation, velocity and position estimation in DR.

For the INS to be able to compute the direction of the distance traveled, the orientation of the device must first be estimated. This is achieved by integrating the body-frame angular-rate measurements (${}^{b}\boldsymbol{\omega_i}$) from the gyroscope. The kinematic equations used to update the body-frame to world-frame rotation at each time instant [5], [10] are presented in equations (3.5) and (3.6):

$$\dot{\boldsymbol{q}}_{\boldsymbol{\omega}} = \frac{1}{2} \cdot \boldsymbol{q}_{\boldsymbol{i-1}} \otimes \left[0_w, {}^{b}\omega_x, {}^{b}\omega_y, {}^{b}\omega_z\right] \tag{3.5}$$

$$\boldsymbol{q}_{\boldsymbol{i}} = \boldsymbol{q}_{\boldsymbol{i-1}} + \dot{\boldsymbol{q}}_{\boldsymbol{\omega}} \cdot dt \tag{3.6}$$

where dt is the time between measurements, $\boldsymbol{q}_{\boldsymbol{i}}$ and $\boldsymbol{q}_{\boldsymbol{i-1}}$ are the current and previous quaternion rotations from body-frame to world-frame and $\dot{\boldsymbol{q}}_{\boldsymbol{\omega}}$ is the quaternion derivative from body-frame to world-frame, which is the result of the quaternion multiplication between

the previous orientation estimate with a quaternion containing a zero scalar component and axis *i, j, k* equal to the angular rates sensed in the body frame axis *x, y* and *z* respectively. Assuming unit quaternions, and since the quaternion conjugate ($\boldsymbol{{}^{b}_{w}q_{i}^{*}}$) is equal to its inverse under this condition, the current orientation estimate ($\boldsymbol{{}^{b}_{w}q_{i}}$) is used to obtain the acceleration measurement in the world-frame using equation (3.7).

$$\boldsymbol{{}^{w}a} = \boldsymbol{{}^{b}_{w}q_{i}} \otimes \left[0_w, {}^{b}a_x, {}^{b}a_y, {}^{b}a_z\right] \otimes \boldsymbol{{}^{b}_{w}q_{i}^{*}} \tag{3.7}$$

Removing gravity in the world-frame is accomplished by simply subtracting the gravity value (9.8 m/s^2 or 1 g) from the vertical axis, perpendicular to the Earth's surface. Integrating the gravity-corrected accelerometer measurements in world-frame yields the velocity estimate. Integrating the velocity estimate yields the position estimate. The problem associated with this procedure is the error that accumulates during both the orientation and the position integration process.

The orientation estimate drift is due to the integration of the angular rate error ($\boldsymbol{{}^{b}e_{i}^{\omega}}$). This drift or orientation error influences the projection of the body-frame accelerometer measurements into the world-frame, which are used in the gravity correction step. This error in the orientation estimate is crucial, especially the roll and pitch (or tilt) angles, which effectively project part of the gravity vector in the wrong direction. The accelerometer error ($\boldsymbol{{}^{b}e_{i}^{a}}$) will also incur in additional position estimation errors, although to a much lesser extent, due to being several orders lower than the error induced from the orientation estimation [1], [3].

Errors in DR will exhibit unbound growth in time. The solution to this problem is addressed by the integration of multiple measurements from different sensors using sensor fusion techniques, which are described in the next section. The application of sensor fusion methods to improve orientation and position estimation is described in sections 3.4 and 3.5 respectively.

3.3 Sensor Fusion

A sensor fusion method is the combination of measurements obtained from several sensors in order to provide a new, more accurate and/or more robust estimate than any of the sources individually. It can be applied to measurements of the same type of sensor, which is the case of the least squares (LS) method from the previous chapter or it can be applied to

measurements from different sensor types. The purpose of sensor fusion is to limit drift errors of the INS, by exploiting information that can be derived from a multitude of different sensors, such as accelerometer, magnetometer, pressure, temperature, Doppler sensor, wind speed, etc.

The complementary filter (CF) is a simple sensor fusion method, which follows a frequency-based approach to combine measurements of the same signal originating from different sensors.

Bayesian filtering is a general approach to the sensor fusion problem using Bayes's rule.

$$P(x|y) = \frac{P(y|x)\,P(x)}{P(y)} \tag{3.8}$$

The state vector (e.g., the parameters of interest such as position, acceleration, velocity, etc.) of the system is estimated through a state dynamics model and a measurement model, each incorporating independent noise in the estimates. The state dynamics assume a Markov model, where the state only depends on the previous state estimate (e.g., states prior to the previous state provide no additional information). Equations (3.9) and (3.10) describe this general probabilistic framework [11].

$$Bel^{-}(x_t) = \int P(x_t|x_{t-1})\,Bel(x_{t-1})\,dx_{t-1} \tag{3.9}$$

$$Bel(x_t) = \alpha_t\,P(z_t|x_t)\,Bel^{-}(x_t) \tag{3.10}$$

The dynamics and measurement models are represented by $P(x_t|x_{t-1})$ and $P(z_t|x_t)$ respectively; α_t is a normalizing constant. The system starts with an initial belief (*Bel*) of the state vector, which is updated by the dynamics model. This new state estimate is then used when a new measurement is available, to recursively update the uncertainty associated with the current estimate. The implementation of this abstract probabilistic approach requires the definition of the dynamics model, the measurement model and the representation of the belief, enabling different filter implementations [11].

The Kalman filter (KF) is a specific case of the general Bayesian filter, which models the uncertainty of the state estimates using Gaussian distributions [12]–[16]. It is a sensor fusion method that follows a stochastic or time domain approach. The KF is generally adopted due to its accuracy and computational efficiency [11].

Particle filters are another Bayesian filtering technique that provides solutions to non-linear cases and are typically used when map information is available, enabling autonomous location estimation by matching features found in the environment to the map information [12], [16]. The main disadvantage of particle filters is the high computational capacity requirement due to the need to generate a large number of particles to obtain accurate estimations.

Due to restrictions in power and computational capacity, wireless sensor networks (WSNs) require low complexity sensor fusion methods, where computational efficiency is crucial. The computational overhead of a KF solution is still significant when considering WSNs. As an example, the work in [17] implements a solution based on KF which imposes a load of 37 % on a 1 GHz Qualcomm Snapdragon processor with 512 MB of RAM (random access memory). WSN nodes have much less computational capacity, with 8 bit microprocessors and frequencies in the order of tens of megahertz.

The next sections describe the CF and KF, which are the most computationally efficient sensor fusion methods.

3.3.1 Complementary Filter

The CF is an application of Wiener filtering theory [18] where two measurements of the same signal with different noise characteristics are combined, in order to provide a better estimate of the signal. Considering as an example a gyroscope signal that is integrated over time to give an estimate of the roll angle, and an accelerometer, where the roll angle is estimated using equation (3.11):

$$roll = tan^{-1}\left(\frac{a_y}{a_z}\right) \tag{3.11}$$

Both sensors are employed to measure the roll angle (signal of interest) and each sensor is affected by noise signals with complementary spectral characteristics: the gyroscope angle estimate is predominantly affected by low frequency noise due to drift from errors accumulated over time, while the accelerometer is predominantly affected by high frequency noise due to external accelerations. The block diagram for this filter type is presented in Figure 3.2.

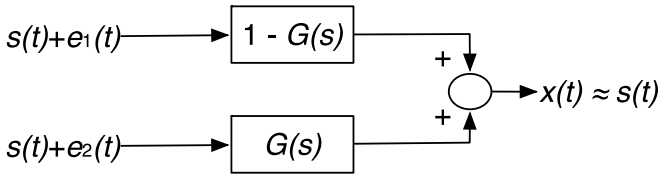

Figure 3.2: Complementary filter block diagram.

Assuming for example that $G(s)$ is a low-pass filter with the Laplace domain transfer function:

$$G(s) = \frac{1}{1 + Ts} \tag{3.12}$$

where T is the time constant defining the cut-off frequency of the filter; the complementary transfer function will be a high-pass filter, as can be seen in equation (3.13), with the same cut-off frequency.

$$1 - G(s) = \frac{Ts}{1 + Ts} \tag{3.13}$$

The CF operates in the frequency domain by high-pass filtering the noise signal e_1 and low-pass filtering the noise signal e_2. Combining the two results the signal is reconstructed, thus removing, or at least attenuating noise signals corrupting the signal of interest $s(t)$. An alternate version of this system is presented in Figure 3.3, where the filter is operating on the noise signals only [18], [19].

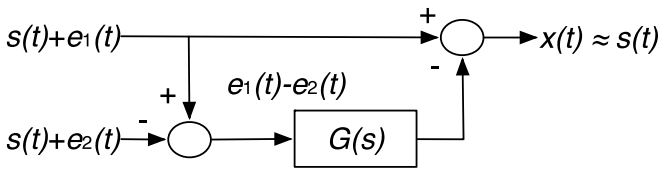

Figure 3.3: Alternate complementary filter block diagram.

By subtracting both measurements, the difference between the noise signals e_1 and e_2 is served as input to the low-pass filter $G(s)$. The filter is effectively estimating the noise signal e_1, which is then subtracted from the measurement affected by the high-frequency noise. This later form of the complementary filter is more appropriate for practical implementations, since it only uses one multiplication operation.

The CF is a well-known technique used in the flight control industry for many years. These filters are a special case of the KF [20] under steady-state conditions, with a much lesser computational burden [19].

3.3.2 Kalman Filter

The KF [20] was proposed in 1960 and is still one of the most important sensor fusion algorithms, with applications in the most diverse areas from defence to commercial and health products. The KF revolutionized the space era by providing the navigation solution to the moon and back in the Apollo moon project [21].

This type of filter is known as the optimal tracking filter and is based on the assumption that the noise present in the measurements and actuation signals are independent and affected by zero-mean Gaussian random variables. Since the product of two Gaussian distributions is also a Gaussian distribution, the filter is able to predict the estimate error. The KF model bases its principle in three sources of information: model dynamics, control inputs and sensor measurements [22]. Model dynamics and control inputs are described in equation (3.14):

$$x_k = A_k x_{k-1} + B_k u_k + w_k \tag{3.14}$$

where x_k is the current state vector, x_{k-1} is the previous state vector, u_k is the input vector containing the control inputs (e.g., throttle force, braking force, steering angle, etc.), the matrices A and B represent the state transition matrix and the control input matrix and w_k is the process noise. The matrix A models the dynamics of the system, applying the effect of the state parameters at time $k-1$ to the system state at time k (e.g., the acceleration or braking force in the previous time step will influence velocity in the current time step). Matrix B converts the effect of input controls u_k to the domain of the state parameters at time k. The sensor measurements are described in equation (3.15):

$$z_k = C_k x_k + v_k \tag{3.15}$$

where z_k is the current sensor measurement vector, C_k is the observation matrix that converts state vector parameters to the domain of sensor measurements and v_k is the measurement noise. The index k indicates that the entities can change over time. The KF updates the state of a system from time $k-1$ to time k by applying equation (3.16), which is known as the state prediction equation:

$$x_k^- = A_k x_{k-1} + B_k u_k \tag{3.16}$$

where x_k^- is the predicted (also known as *a priori*) state vector containing the variables to track at time k (e.g., position, velocity, acceleration, orientation, sensor bias, etc.). This prediction step is subject to the process noise w_k with covariance matrix Q_k affecting the state parameters. The filter updates the error prediction P_k^- using equation (3.17):

$$P_k^- = A_k P_{k-1} A_k^T + Q_k \tag{3.17}$$

where P_{k-1} is the previous error estimate. Equations (3.16) and (3.17) represent the prediction phase of the KF, which is followed by the measurement phase by applying equation (3.18) to compute the Kalman gain:

$$K_k = P_k^- C_k^T (C_k P_k^- C_k^T + R_k)^{-1} \tag{3.18}$$

where C_k^{T} is the transpose of matrix C_k and R_k is the covariance matrix of v_k, which accounts for errors in the measurement process. The filtered state estimate is then computed using equation (3.19):

$$x_k = x_k^- + K_k(z_k - C_k x_k^-) \tag{3.19}$$

where the predicted values are compared with the measured values (also known as *innovation*). The Kalman gain acts as a weighting function of the *innovation*, given the uncertainty of the errors associated with each source of information. A smaller Kalman gain or smaller *innovation* implies better tracking by the system, since smaller corrections are applied to the predicted state. Equation (3.19) is based on the same principle of the complementary filter from section 3.3.1, applied in the estimation of the vector parameter. The error of the final estimate is obtained using equation (3.20):

$$P_k = (I - K_k C_k) P_k^- \tag{3.20}$$

where I is the identity matrix. This model is applied to linear systems where matrix A is a linear function of x_k and w_k, and matrix C is a linear function of x_k and v_k. The control inputs of the KF model are usually absent when KFs are used in the context of INS applied to human motion.

An extended KF (EKF) is used when the system is described by nonlinear functions. The EKF transforms the nonlinear function into an approximate linear function using a first order Taylor series expansion [23]. This requires the computation of a Jacobian matrix and is sensitive to inaccuracies in the approximation and initial conditions, which affect the filter

performance. As an alternative, the unscented KF (UKF) is proposed, which improves the performance of the filter under nonlinear systems, with increased complexity and computation capacity. Under the specific case of human motion, the UKF is considered to have approximately the same accuracy of the EKF [24].

3.4 Improving Orientation Estimates

A simple method to obtain an improved orientation estimate is the FQA (factored quaternion algorithm) presented in [25]. This method uses the accelerometer sensor to obtain roll and pitch angles directly from accelerometer measurements, assuming that the IMU is stationary (i.e., only the gravitational force is present in the accelerometer measurements). The magnetometer measurements are used in the same way as in a tilt-compensated e-compass [26], from which the yaw angle is extracted. One advantage of this method is that magnetometer measurements are only used in the estimation of the yaw angle. This implies that magnetic disturbances do not influence the projection of gravity, which is a critical part for reducing error growth in INS. The main issue associated with FQA or the tilt-compensated e-compass method is that the stationary condition of the accelerometer measurements is seldom the use case in the context of human motion.

Information from other sensors in the IMU can be used to compensate the gyroscope bias drift by employing the sensor fusion techniques described in section 3.3. One common approach to improve orientation estimates is to apply a minimization technique such as the Gauss-Newton algorithm (GNA) [5], [27] to estimate the error of the orientation using a cost function that relates the previous orientation estimate and the current sensor measurements (accelerometer measurements are compared to gravity and magnetometer measurements are compared to the current reference heading). The iterative GNA is presented in equation (3.21).

$$x_{n+1} = x_n - (J_r^T J_r)^{-1} J_r^{\mathrm{T}}\, r(x_n) \tag{3.21}$$

where x is the orientation error estimate, J is the Jacobian matrix and r the cost function. This error estimate is combined with the gyroscope measurements using a CF. The error-filtered orientation rate is integrated and normalized in order to obtain the final orientation. An identical approach using an EKF instead of a CF is found in [28]. The cut-off frequency of the CF is a parameter that can be controlled, which in [27] is adaptively modified according to the convergence rate of the GNA and the divergence rate of the gyroscope.

One disadvantage of the GNA method is the sensitivity to biased measurements, which causes convergence issues. To counter this, authors in [27] implement a compensation method based on the magnitude of the acceleration and magnetic measurements. When the magnitude of these vectors exceeds a predefined threshold, they are replaced by estimates of accelerometer and magnetometer measurements obtained using the previous orientation information. Another disadvantage is the requirement to compute a matrix inversion.

The gradient descent algorithm (GDA) [10] is a strategy similar to the GNA, for which the iterative equation is presented in (3.22).

$$x_{n+1} = x_n - \mu J_r^{\mathrm{T}} r(x_n) \tag{3.22}$$

where μ is known as the gain or learning rate. The advantage is that GDA does not require a matrix inversion such as in GNA, allowing for faster update rates. Performance results presented have the same level of accuracy of a KF approach with much lower computational loads.

Solutions like GNA or GDA are iterative minimization solutions, which in the cases presented are reduced to a single iteration. This is considered acceptable when the convergence rate is equal or greater than the rate of change of the orientation. When the sensor measurements are biased (e.g., under magnetic disturbance or external accelerations), GNA and GDA will be subject to slow convergence.

An EKF is proposed in [24], where it is assumed that the gyroscope bias is negligible. The states modelled are a quaternion representing orientation and the magnetometer bias to account for local variations of the magnetic field. The variance parameters of the accelerometer and magnetometer are modified according to thresholds, due to the known sensitivity of the EKF to biased measurements. These thresholds protect against external accelerations and magnetic disturbances by diminishing the effect of accelerometer and magnetometer sensors in the final estimation. In extreme conditions, the filter estimate will be affected only by the gyroscope measurement.

One option available in the KF framework is to reduce the number of parameters to be estimated by the filter. If the errors of the state are modelled instead of the states themselves, the dimension of the state parameter can be reduced, effectively improving the computation of the filter equations. The states of interest need to be updated outside the KF and take into account the estimated error. This configuration is known as indirect KF (IKF) and one such

configuration is proposed in [29], where the orientation error, accelerometer and gyroscope bias are the states estimated. The magnetometer sensor only contributes to the yaw angle and an adaptive algorithm which estimates and corrects for bias in the accelerometer measurements, is also included to account for external accelerations.

The author in [30] examined the performance of KFs versus CFs under simple motion and walking motion scenarios. The CF performed better than the KF both in terms of orientation error (with CF estimates between 60% to 70% better than KF estimates) and time taken to compute an estimate (with the time to compute an update of 280 μs and 1.3 ms for the CF and KF respectively). It is also noted that the microcontroller used in [30] is able to perform single-cycle multiplications. A WSN based on the CC2530 system-on-chip (SoC) [31], such as the one used in this work, uses an 8-bit 8051 microcontroller, which does not possess this functionality. Under these circumstances, multiplication operations have a significant impact in the algorithm efficiency, especially in the case of the KF where a matrix inversion is computed. The work in [32] also compared performances of orientation estimation using EKF versus orientation estimation using CF under typical scenarios of human motion, where it is shown that there is not a significant difference among the errors found for each solution.

The CF and KF solve the problem of drift from the gyroscopes by estimating bias errors and/or by combining accelerometers and magnetometers. The KF requires a model of the dynamics involved and provides not only an estimate but also the uncertainty of the estimate, feature which is absent when using CFs. On the other hand, the CF solution is easier to implement since it does not depend on dynamic models, requiring only that the inputs are spectral complements of each other.

3.5 Improving Distance Estimates

Using MEMS sensors in INS results in fast error accumulation, even in static condition scenarios such as [3]. If the IMU is subject to external accelerations, even higher error accumulation is expected. In the context of human motion, the INS can be used to identify gait cycle parameters in order to detect steps (time between two footfalls on opposite feet) or strides (time between two footfalls of the same foot). This is known as a pedestrian dead reckoning (PDR) system and results from a segmentation of the INS position estimates into a step/stride and heading system (SHS) [33]. The information of the SHS will produce a

position estimation error that, instead of unbound error growth over time as in the case of the INS, will exhibit error growth as a percentage of the distance travelled.

PDR systems have been studied and applied in several different fields in the medical area to analyse gait cycle and monitor healing progress of patients in rehabilitation, in the context of first responders to help fire-fighters in critical missions and in virtual reality and commercial applications for navigation. The step/stride detection (SD) algorithm depends on the type of sensors used and the location where the IMU is attached to the body. The step information enables the application of pseudo-measurements commonly known as zero-velocity updates (ZVU) when the foot is planted on the floor and zero-angular-rate updates (ZAU) when the person is not walking (i.e., the person is still). An alternative to the distance estimation through double integration of acceleration is to estimate each step/stride length (SL) by inferring distance from the measured data.

3.5.1 Stride Detection

The gait cycle of a healthy person is typically divided primarily into stance and swing phases [34], as depicted in the stride example of Figure 3.4 (adapted from [35]).

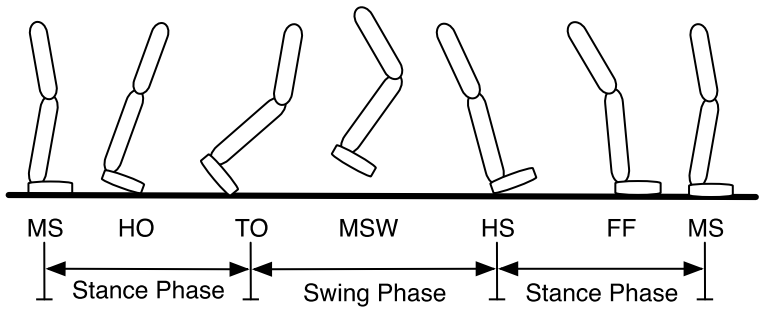

Figure 3.4: Gait cycle.

In the stance phase, the foot is in contact with the floor. Starting in the mid-stance (MS), the transition to the swing phase involves the foot pushing the body forward while lifting the heel (heel-off - HO) from the floor, until toe-off (TO) occurs. The swing phase starts when the foot is no longer in contact with the floor and swings forward (mid-swing - MSW) until the heel-strike (HS), which marks the end of the swing-phase and the beginning of the stance phase. The opposite foot repeats this sequence of events but out of phase, since when one foot is in HS, the other is in HO.

SD algorithms are mainly characterized in [33] as stance detection or step cycle detection. Stance detection algorithms are typically threshold-based and involve identifying

periods of inactivity in the IMU measurements [36], which correspond to the periods where the foot is planted in the floor. In [37] a general framework is derived to characterize stance detection algorithms, for which the most commonly used methods are the acceleration moving variance, the acceleration magnitude and the angular rate energy. Stance detection is usually accomplished by placing the sensor on the foot.

An example of SD using the acceleration moving variance is implemented in [38], where the IMU is attached to the foot. The magnitude of the acceleration is computed for every sample, while the acceleration variance is computed for a window of 15 samples at 100 Hz. The thresholds are chosen empirically and are applied to the acceleration variance. Variances above 2 m/s^2 identify the swing phase and variances below 1 m/s^2 identify the stance phase. A step is detected when the swing phase ends and the stance phase starts. The reported percentage of error is 0.1 % of the real number of steps.

The gyroscope based algorithm from [39] using a foot-mounted IMU is also implemented and tested in [38]. The magnitude of the gyroscope measurements is computed for every sample and the resulting signal is filtered in order to avoid small fluctuations. An empirical threshold value of 1 rad/s was used, reporting a percentage of error of 0.2 % of the real number of steps. An algorithm using the magnetometer is also implemented in [38], which high-pass filters the magnetometer signal before applying the same procedure for the gyroscope signal. The threshold value for the magnetometer algorithm is not provided. The percentage of errors reported is 0.94 %.

The work in [40] uses the pitch angle of a sensor placed in the trousers' pocket. The pitch angle is obtained from an orientation estimation method using UKF, applied to accelerometer, gyroscope and magnetometer measurements. A simple fixed threshold is used for peak detection of the pitch angle, which according to the authors does not vary with the user's velocity. In a challenging test including stairs, an acceleration magnitude algorithm detected 87 % of the steps, while the authors' proposed method detected all steps.

Stride cycle detection involves searching the sensor data for patterns that identify one or a subset of the events depicted in Figure 3.4, typically resorting to peak detection and zero crossing. Spectral analysis, template matching and autocorrelation can also be applied, with added computational complexity [41]. Event detection is implemented in [34] using accelerometer signals, by searching the measurements for a specific order of the events during a normal step, with the sequence being: opposite foot strike, TO, initial swing, terminal swing

and foot strike. Although author reports errors in the order of 10 % of the distance travelled, no report is given about the accuracy of the SD algorithm.

Authors in [42] look for parameters in the gyroscope measurements that conform to a trend signal that is typical for the gyroscope output when placed in the foot. These parameters are then seen as events that are fed to a finite state machine. After applying filtering, a SD accuracy of 100 % is reported, in the form of detected ZVU intervals.

The accelerometer can be placed in the waist in order to detect hip movements while walking [43]. Slope changes in the averaged vertical acceleration axis indicate a step. To improve the step-counting accuracy, the slope changes or peaks should be detected at appropriate times, during a time window of approximately ±15 %, since the step frequency has a tendency to maintain within these limits during steady state walking. Authors in [17] also use a hip mounted accelerometer and apply the threshold to the acceleration energy instead of the acceleration variance. In [44] authors place an accelerometer in the ankle to detect the swing phase and the heel touch down of the step. Multiple thresholds are applied to detect each event, with a SD accuracy of 99 %.

Under steady walking, both stance and step cycle detection present good SD accuracy values, near 100 %. Issues arise when the user is not steadily walking, during very slow motion (e.g., slowly walking in a waiting line), while turning, sidestepping or walking intermittently, or when SD is used in irregular floors, stairs and access ramps. The signal patterns change under these conditions, giving rise to missed steps. Also, SD applied to mobility-impaired persons can report errors as high as 29 % [33]. When a person steps onto elevators, escalators or moving walkways, step data is either absent or highly biased from external motions.

3.5.2 Step Length Estimation

Step or stride length estimation is typically applied having in consideration a specific model that, such as in the SD case, depends on the location of the sensor. The further away the IMU is from the foot, the higher the abstraction necessary for estimating SL is. This type of estimation is typically dependent on a calibration procedure, to adjust parameters of the model to each user. In [43], where the accelerometer is located in the hip, the leg is seen as a lever of fixed length when the foot is on the floor and the stride length is estimated as:

$$Stride \approx \frac{2 \times Bounce}{\alpha} \tag{3.23}$$

where *Bounce* is the vertical displacement of the hip and α is the angle between the leg and the vertical direction. By empirical demonstration, the angle α is replaced by a constant K and the vertical displacement is given by the difference between the maximum (A_{max}) and minimum (A_{min}) acceleration of the hip. The stride length is given by equation (3.24).

$$Stride \approx \sqrt[4]{A_{max} - A_{min}} \times K \tag{3.24}$$

The K parameter is typically used as a calibration value that differs between users [38], [40]. Errors between 0.30 % and 0.78 % of the distance travelled were reported in [38] for different walking speeds.

The SL estimation in [40], where the IMU is located in the trousers' pocket, is accomplished by applying the pitch angle used for SD, described in equation (3.25)

$$SL = a \cdot \Delta\theta + b \tag{3.25}$$

where $\Delta\theta$ is the pitch amplitude in degrees, and parameters a and b are the slope and intercept respectively, found by applying linear regression to data collected for each user. Authors reported a mean error of 0.15 % of the distance travelled, with trials performed at different speeds.

SL estimation applied to handheld IMUs is studied in [45], where the SL is given by equation (3.26):

$$s = h \cdot \left(a \cdot f_{step} + b\right) + c \tag{3.26}$$

where h is the user's height, f_{step} is the frequency of the step and a, b and c are calibration parameters. Errors between 2.5 % and 5 % of the total travelled distance are reported.

On the other hand, systems that apply the IMU closer to the foot either estimate the SL using empirical approximations or using motion models that do not depend on calibration parameters. The work in [44] uses equation (3.27), obtained from experiments, applied to acceleration measurements collected by a sensor located in the ankle of the subject.

$$Stride(m) = 0.98 \times \sqrt[3]{\frac{\sum_{k=1}^{N} |A_k|}{N}} \tag{3.27}$$

where A_k is the measured acceleration during a stride cycle. This simple method achieved 5 % errors in total distance travelled.

A shank-mounted IMU is used in [46] to estimate SL, speed and slope in each gait cycle. The authors use an inverted pendulum model of walking due to the IMU being located in the shank. For each gait cycle, the acceleration is resolved to the world-frame by integrating gyroscope measurements. Double integration is applied to the world-frame acceleration measurements in order to estimate SL, with initial conditions for velocity and position set to zero. The authors present the results for speed and slope estimates during walking, which exhibit an error between 5 % and 13 % at different walking speeds and under different slopes.

One popular solution for SL estimation is to take advantage of pseudo-measurements (ZVU and ZAU) to provide a reset mechanism to the integration procedures, which can be applied directly to the SL estimation or to reduce integration drift in the INS.

3.5.3 Exploring Pseudo-Measurements

Given the cyclical nature of walking, pseudo-measurements of velocity and angular rate can be inferred from the state of the gait cycle. For a foot-mounted IMU, when the gait reaches the stance phase, the velocity of the foot is known to be zero. As such, this information is used to limit the drift error by forcing the velocity of the foot-mounted INS to zero (ZVU), thus resetting the integration errors. This enables the integration procedure to be performed only for short periods of time (smaller than the step period, in the order of half a second), during which the drift accumulation is typically negligible. The ZVU is the most versatile method since it can be used to estimate displacement in any direction, as opposed to other methods that assume the step/stride is performed in the forward direction. It can also be used to resolve vertical displacements, such as climbing stairs or access ramps [15], [47].

ZVUs are implemented in [48] where the integration cycle is applied only during the swing phase. In [15], ZVUs are applied to a 15-state EKF estimating biases for orientation, angular rate, position, velocity and acceleration. This is further integrated with GPS and magnetometer measurements in order to correct for heading drift, achieving 0.3 % error of the total distance travelled in both indoor and outdoor scenarios.

The authors in [49] use a CF to estimate orientation and apply ZVUs to the integration of the gravity-corrected world-frame acceleration measurements. SL estimation errors of 1.1

% of travelled distance are reported for an outdoor scenario. The work in [39] applies a similar strategy to the integration of the acceleration measurements to both indoor and outdoor scenarios. As expected, outdoor scenarios generally exhibit lower heading error than indoor scenarios, due to magnetic interferences. Errors due to magnetic disturbances range from 1 % of distance travelled in outdoor scenario to 16 % of distance travelled in indoor scenario.

When the user is still (i.e., not walking), the angular rate can also be inferred as zero. This pseudo-measurement can be used to limit the heading drift of the INS. ZAUs are used in [47], [50], [51] to improve heading estimates using KF-based solutions. Another solution to improve heading estimates is the method employed in [51], in which the corridors in buildings are assumed as straight paths. This method enables heading error estimation and correction when the straight corridor assumption is true. When this is not the case, the positioning error increases with the duration of the circular path.

As a concluding remark, the work in [52] studies the effects of modelling sensor biases when applying ZVUs, showing that the *innovation* sequences from a KF are correlated with the steps. Insufficient bandwidth is identified as one possible reason for this correlation, due to the extreme dynamics that the foot is subject to during heel-strike.

3.6 References

[1] C. Gentile, N. Alsindi, R. Raulefs, and C. Teolis, *Geolocation Techniques*. Springer, 2013.

[2] S. Sukkarieh, E. M. Nebot, and H. F. Durrant-Whyte, ‘A high integrity IMU/GPS navigation loop for autonomous land vehicle applications’, *IEEE Transactions on Robotics and Automation*, vol. 15, no. 3, pp. 572–578, Jun. 1999.

[3] J. O. Woodman, ‘An introduction to inertial navigation’, Cambridge, United Kingdom, 2007.

[4] K. Mohamadabadi, ‘Anisotropic Magnetoresistance Magnetometer for inertial navigation systems’, Ecole Polytechnique, 2013.

[5] E. R. Bachmann, R. B. McGhee, X. Yun, and M. J. Zyda, 'Inertial and Magnetic Posture Tracking for Inserting Humans into Networked Virtual Environments', *Proc. of the ACM symposium on Virtual reality software and technology VRST*, p. 9, 2001.

[6] Vectornav, 'VectorNav Support Library: Calibration.' [Online]. Available: http://www.vectornav.com/support/library/calibration.

[7] IEEE, '1293-1998 - IEEE Standard Specification Format Guide and Test Procedure for Linear, Single-Axis, Non-Gyroscopic Accelerometers', 2011.

[8] M. J. Caruso, 'Applications of magnetic sensors for low cost compass systems', in *IEEE 2000. Position Location and Navigation Symposium (Cat. No.00CH37062)*, 2000, pp. 177–184.

[9] D. W. Allan, N. Ashby, and C. C. Hodge, 'The Science of Timekeeping', 1997.

[10] S. O. H. Madgwick, A. J. L. Harrison, and R. Vaidyanathan, 'Estimation of IMU and MARG orientation using a gradient descent algorithm', in *2011 IEEE International Conference on Rehabilitation Robotics*, 2011, vol. 2011, pp. 1–7.

[11] D. Fox, J. Hightower, L. Liao, D. Schulz, and G. Bordello, 'Bayesian filtering for location estimation', *IEEE Pervasive Computing*, vol. 2, no. 3, pp. 24–33, 2003.

[12] F. Evennou and F. Marx, 'Advanced Integration of WiFi and Inertial Navigation Systems for Indoor Mobile Positioning', *EURASIP Journal on Advances in Signal Processing*, pp. 1–12, 2006.

[13] N. Castaneda and S. Lamy-Perbal, 'An improved shoe-mounted inertial navigation system', in *International Conference on Indoor Positioning and Indoor Navigation*, 2010, no. September.

[14] G. Glanzer, T. Bernoulli, T. Wiessflecker, and U. Walder, 'Semi-autonomous indoor positioning using MEMS-based inertial measurement units and building information', *2009 6th Workshop on Positioning, Navigation and Communication*, vol. 2009, pp. 135–139, Mar. 2009.

[15] E. Foxlin, 'Pedestrian tracking with shoe-mounted inertial sensors', *IEEE Computer Graphics and Applications*, vol. 25, no. 6, pp. 38–46, 2005.

[16] B. Krach and P. Roberston, 'Cascaded estimation architecture for integration of foot-mounted inertial sensors', in *Position, Location and Navigation Symposium, 2008 IEEE/ION*, 2008, no. 1, pp. 112–119.

[17] T. Gadeke, J. Schmid, M. Zahnlecker, W. Stork, and K. D. Muller-Glaser, 'Smartphone Pedestrian Navigation by Foot-IMU Sensor Fusion', in *Ubiquitous Positioning, Indoor Navigation, and Location Based Service (UPINLBS)*, 2012, pp. 1–8.

[18] R. G. Brown and P. Y. C. Hwang, *Introduction to Random Signals and Applied Kalman Filtering*. 1997.

[19] W. T. Higgins, 'A Comparison of Complementary and Kalman Filtering', *IEEE Transactions on Aerospace and Electronic Systems*, vol. AES-11, no. 3, pp. 321–325, 1975.

[20] R. E. Kalman, 'A New Approach to Linear Filtering and Prediction Problems', *Transactions of the ASME-Journal of Basic Engineering*, vol. 82, no. Series D, pp. 35–45, 1960.

[21] M. S. Grewal and A. P. Andrews, 'Applications of Kalman filtering in aerospace 1960 to the present', *IEEE Control Systems Magazine*, vol. 30, no. 3, pp. 69–78, 2010.

[22] E. Brookner, *Tracking and Kalman Filtering Made Easy*. John Wiley & Sons, Inc, 1998.

[23] S. Julier and J. Uhlmann, 'Unscented Filtering and Non Linear Estimation', *Proceedings of the IEEE*, vol. 92, no. 3, pp. 401–422, 2004.

[24] A. M. Sabatini, 'Estimating three-dimensional orientation of human body parts by inertial/magnetic sensing', *Sensors*, vol. 11, no. 2, pp. 1489–1525, 2011.

[25] X. Yun, E. R. Bachmann, and R. B. McGhee, 'A simplified quaternion-based algorithm for orientation estimation from earth gravity and magnetic field measurements', *IEEE Transactions on Instrumentation and Measurement*, vol. 57, no. 3, pp. 638–650, 2008.

[26] T. Ozyagcilar, 'Implementing a tilt-compensated eCompass using accelerometer and magnetometer sensors', 2012.

[27] Y. Tian, H. Wei, and J. Tan, 'An adaptive-gain complementary filter for real-time human motion tracking with MARG sensors in free-living environments', *IEEE Transactions on Neural Systems and Rehabilitation Engineering*, vol. 21, no. 2, pp. 254–264, 2013.

[28] J. L. Marins, X. Y. X. Yun, E. R. Bachmann, R. B. McGhee, and M. J. Zyda, 'An extended Kalman filter for quaternion-based orientationestimation using MARG sensors', *Proceedings 2001 IEEE/RSJ International Conference on Intelligent Robots and Systems. Expanding the Societal Role of Robotics in the the Next Millennium (Cat. No.01CH37180)*, vol. 4, pp. 2003–2011, 2001.

[29] Y. S. Suh, 'Orientation estimation using a quaternion-based indirect Kalman filter with adaptive estimation of external acceleration', *IEEE Transactions on Instrumentation and Measurement*, vol. 59, no. 12, pp. 3296–3305, 2010.

[30] A. D. Young, 'Comparison of Orientation Filter Algorithms for Realtime Wireless Inertial Posture Tracking', in *2009 Sixth International Workshop on Wearable and Implantable Body Sensor Networks*, 2009, pp. 59–64.

[31] T. Instruments, 'CC253x System-on-Chip Solution for 2.4-GHz IEEE 802.15.4 and ZigBee® Applications', 2012.

[32] E. Bergamini, G. Ligorio, A. Summa, G. Vannozzi, A. Cappozzo, and A. M. Sabatini, 'Estimating Orientation Using Magnetic and Inertial Sensors and Different Sensor Fusion Approaches: Accuracy Assessment in Manual and Locomotion Tasks', *Sensors*, pp. 18625–18649, 2014.

[33] R. Harle, 'A Survey of Indoor Inertial Positioning Systems for Pedestrians', *IEEE Communications Surveys & Tutorials*, vol. 15, no. 3, pp. 1281–1293, Jan. 2013.

[34] R. G. Stirling, 'Development of a Pedestrian Navigation System Using Shoe Mounted Sensors', University of Alberta, 2004.

[35] K. De Koster, 'Gait.' [Online]. Available: http://www.physio-pedia.com/Gait.

[36] A. Olivares, J. Ramírez, J. M. Górriz, G. Olivares, and M. Damas, 'Detection of (In)activity Periods in Human Body Motion Using Inertial Sensors: A Comparative Study', *Sensors*, vol. 12, no. 12, pp. 5791–5814, 2012.

[37] I. Skog, P. Händel, J.-O. Nilsson, and J. Rantakokko, 'Zero-velocity detection - An Algorithm Evaluation', *IEEE transactions on bio-medical engineering*, vol. 57, no. 11, pp. 2657–2666, 2010.

[38] A. R. Jimenez, F. Seco, C. Prieto, and J. Guevara, 'A comparison of Pedestrian Dead-Reckoning algorithms using a low-cost MEMS IMU', in *2009 IEEE International Symposium on Intelligent Signal Processing*, 2009, pp. 37–42.

[39] R. Feliz, E. Zalama, and J. G. García-Bermejo, 'Pedestrian tracking using inertial sensors', *Journal of Physical Agents*, vol. 3, no. 1, pp. 35–42, 2009.

[40] E. M. Diaz and A. L. M. Gonzalez, 'Step detector and step length estimator for an inertial pocket navigation system', in *2014 International Conference on Indoor Positioning and Indoor Navigation (IPIN)*, 2014, no. 2, pp. 105–110.

[41] A. Brajdic and R. Harle, 'Walk detection and step counting on unconstrained smartphones', in *Proceedings of the 2013 ACM international joint conference on Pervasive and ubiquitous computing - UbiComp '13*, 2013, p. 225.

[42] S. K. Park and Y. S. Suh, 'A zero velocity detection algorithm using inertial sensors for pedestrian navigation systems.', *Sensors (Basel, Switzerland)*, vol. 10, no. 10, pp. 9163–78, Jan. 2010.

[43] H. Weinberg, 'Using the ADXL202 in pedometer and personal navigation applications', 2002.

[44] J. W. Kim, H. J. Jang, D.-H. Hwang, and C. Park, 'A Step, Stride and Heading Determination for the Pedestrian Navigation System', *Journal of Global Positioning Systems*, vol. 3, no. 1&2, pp. 273–279, Dec. 2004.

[45] V. Renaudin, M. Susi, and G. Lachapelle, 'Step Length Estimation Using Handheld Inertial Sensors', *Sensors*, vol. 12, no. 12, pp. 8507–8525, Jun. 2012.

[46] Q. Li, M. Young, V. Naing, and J. M. Donelan, 'Walking speed and slope estimation using shank-mounted inertial measurement units', in *2009 IEEE International Conference on Rehabilitation Robotics*, 2009, pp. 839–844.

[47] A. R. Jiménez, F. Seco, F. Zampella, J. C. Prieto, and J. Guevara, 'Ramp Detection with a Foot-Mounted IMU for a Drift-Free Pedestrian Position Estimation', in *International Conference on Indoor Positioning and Indoor Navigation*, 2011, no. September.

[48] F. Cavallo, A. M. Sabatini, and V. Genovese, 'A step toward GPS/INS personal navigation systems: Real-time assessment of gait by foot inertial sensing', *2005 IEEE/RSJ International Conference on Intelligent Robots and Systems, IROS*, pp. 109–113, 2005.

[49] X. Yun, J. Calusdian, E. R. Bachmann, and R. B. McGhee, 'Estimation of Human Foot Motion During Normal Walking Using Inertial and Magnetic Sensor Measurements', *IEEE Transactions on Instrumentation and Measurement*, vol. 61, no. 7, pp. 2059–2072, Jul. 2012.

[50] A. R. Jiménez, F. Seco, J. C. Prieto, and J. Guevara, 'Indoor pedestrian navigation using an INS/EKF framework for yaw drift reduction and a foot-mounted IMU', in *2010 7th Workshop on Positioning, Navigation and Communication*, 2010, no. section IV, pp. 135–143.

[51] A. R. Jiménez, F. Seco, F. Zampella, J. C. Prieto, and J. Guevara, 'Improved Heuristic Drift Elimination (iHDE) for Pedestrian Navigation in Complex Buildings', in *International Conference on Indoor Positioning and Indoor Navigation*, 2011, no. September.

[52] J. Nilsson, I. Skog, and P. Händel, 'A note on the limitations of ZUPTs and the implications on sensor error modeling', in *2012 International Conference on Indoor Positioning and Indoor Navigation (IPIN)*, 2012, no. November, pp. 13–15.

Chapter 4

RSS Positioning Performance Comparison

Received signal strength (RSS) based positioning is a popular approach in wireless sensor networks (WSNs) since RSS is readily available within the radio module. Due to typical WSN energy consumption and computational constraints, low complexity positioning solutions are desired. The aim of this chapter is to compare positioning methods suitable for WSNs that best fit the indoor scenario. As such, a practical implementation of RSS based positioning using wireless sensor nodes is realized. Positioning calculation is compared using three types of positioning methods compatible with WSNs in an indoor test scenario: map-matching (also known as fingerprinting), approximate positioning and exact positioning algorithms.

Map-matching solutions are mainly used in large areas, such as office settings and warehouses with several divisions. This comparison differs from the usual approach, since the fingerprinting solution is implemented in a smaller predefined space of a room, without walls in between access points.

The goal is to study positioning techniques that are compatible with real-time positioning in WSN, having low-power and low complexity as requirements, yet presenting the best accuracy possible under such conditions.

4.1 Hardware Platform

The wireless sensor nodes communicate using the IEEE 802.15.4 medium access control (MAC) protocol, working on the 2.4 GHz frequency band. The development kit CC2530DK [1] from Texas Instruments is used in this work. The CC2530 is a system-on-chip (SoC) solution that contains an 8051 microprocessor, a radio transceiver and general I/O (input/output) peripherals. The CC2530 radio has a sensitivity of -97 dBm and a maximum transmission power of +4.5 dBm. The modules are equipped with the Antenova M2M 2.4 GHz swivel antenna [2].

Figure 4.1: CC2530 development board (left) and battery board (right) with evaluation modules.

The test scenario used is composed by four anchor nodes and one sensor node. Each anchor node is composed by a CC2530 evaluation module and a battery board powered by two AA batteries. The sensor node is composed by a development board and an evaluation module. The development board contains necessary hardware to interface with the USART (universal synchronous asynchronous receiver transmitter), used to communicate through standard RS-232 serial port.

4.2 Experimental Setup

The anchor's role is to broadcast beacon messages periodically, so sensor nodes can receive these messages and locate themselves. The test bed is a room with 10×4.7 m free space area, as shown in Figure 4.2. Anchor locations are depicted as green circles, along with distances to walls and the three supporting beams are depicted as squares. Black dots indicate calibration points. A calibration point was also taken at each anchor location.

Anchors are placed in the corners of the mentioned area on top of a stand, 1.2 meters above ground. The stands used are made of plastic, so no extra interferences affect the radio messages. Numbered from 1 to 4, each anchor broadcasts one beacon message periodically, at the start of each 100-millisecond superframe.

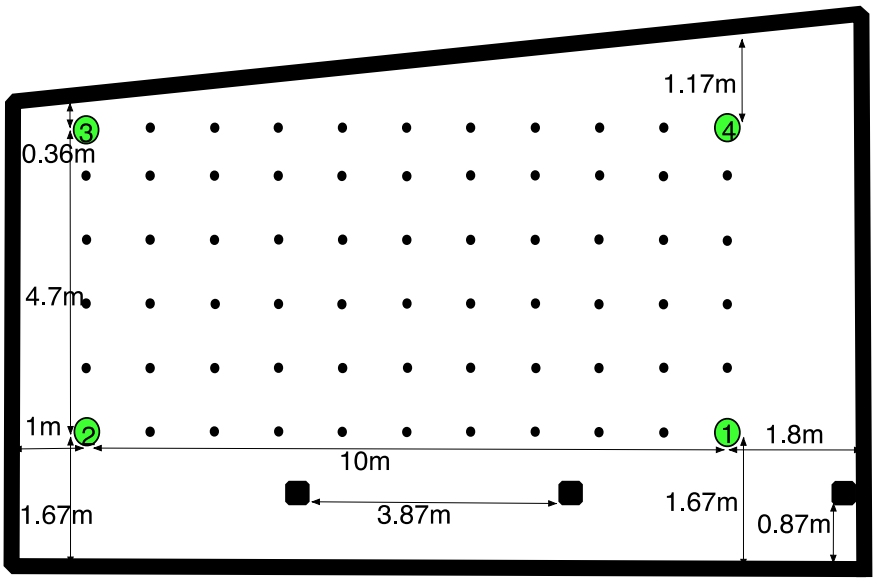

Figure 4.2: Experimental setup scenario.

In order to have synchronized beacon messages from anchors, a simple scheme was adopted. As soon as anchor 2 receives beacon message from anchor 1, anchor 2 begins broadcasting its own beacon periodically, and so forth. Anchor nodes bypass the usual CSMA/CA (carrier sense multiple access/collision avoidance) in their transmissions, so timings between transmissions do not overlap. Messages arrive sequentially and free of collision since all anchors transmit in different time instants.

Using the sequence number in the beacon messages, the sensor node detects lost beacons during data collection and inserts a value of -127, indicating an invalid RSS sample. Since the goal is to assess accuracy of positioning algorithms for our use case scenario, nodes

were only used to obtain real data from the test site, leaving calculations to be performed in an offline phase.

4.2.1 Propagation Model Calibration

The testing area used does not have walls between devices, and therefore the multiwall model was discarded and the one-slope model was used. The one-slope model was used as the linear (in the coefficients) non-polynomial model, to find the *n* parameter of the one-slope model:

$$M(x) = c_1\Phi_1(x) + c_2\Phi_2(x) \tag{4.1}$$

with $\Phi_1 = 1$ and $\Phi_2 = 10 \times \log_{10}(x)$, where a reference distance of 1 meter was used. The model coefficients are calculated by minimizing the squared error between the model and the measurements taken at the site:

$$S = \sum_{i=1}^{N} (f_i - M(x_i))^2 \tag{4.2}$$

The solution is found by solving a system of equations in augmented matrix form:

$$\left[\begin{array}{cc|c} \sum_{i=1}^{N}\Phi_1\Phi_1 & \sum_{i=1}^{N}\Phi_1\Phi_2 & \sum_{i=1}^{N}\mathrm{f_i}\Phi_1 \\ \sum_{i=1}^{N}\Phi_2\Phi_1 & \sum_{i=1}^{N}\Phi_2\Phi_2 & \sum_{i=1}^{N}\mathrm{f_i}\Phi_2 \end{array}\right] \tag{4.3}$$

A best-fit value is calculated using samples taken at different distances from the anchor nodes.

4.2.2 Positioning Algorithms

Three different types of algorithms were tested in this performance comparison: map-matching, approximate and exact positioning methods. The usual two-phase approach was employed for the map-matching solution. During the offline phase, a sensor node was used to collect calibration points in the area confined by the four anchor nodes. At each grid point position, true *x* and *y* values and body orientation (e.g., north, west, south and east) was recorded.

A calibration point is composed by average, minimum, maximum and standard deviation values obtained from the RSS indication field in beacon messages. For each

calibration point, 100 RSS samples were collected from all anchor nodes, followed by computation and storage of the calibration point in the radio map database.

The radio map was created with a grid resolution of one square meter (one point each meter along each axis). Since the positioning area is 4.7 meters wide, the last column of the grid has a smaller resolution of 0.7 square meters. The test field is covered by a total of 66 points, with 4 sampling directions on each point, amounting to a total of 264 calibration points. After collecting all calibration points during the offline phase, the corresponding database was created. Each entry of the table is composed by: position (real position coordinates x, y and direction d) and average RSS for each anchor node. The minimum, maximum and standard deviation for each calibration point were also stored. Although these values have not been used in the position calculation process, they allow a qualitative initial evaluation of the fingerprinting map created.

During the online phase, the sensor node obtains RSS samples and stores them. At the end of a test run (e.g.: after collecting 100 samples), RSS data is uploaded to the personal computer (PC) running MATLAB and the position is computed using the weighted k-nearest neighbours (WKNN) algorithm.

The data collected during the online phase for the map-matching solution is also used to compute positions using the approximate and exact positioning solutions. For the approximate positioning method, weighted centroid localization (WCL) is applied, where two different parameters are used as weights to compute position: the RSS and the distance obtained from the path loss model. In the exact positioning method, the linear least squares (LLS) algorithm is used, where the path loss model is first applied to the RSS for conversion into a distance estimate. This distance is then served as input for the LLS method to find the position of the sensor node.

4.3 Results

One aspect of RSS positioning that is essential to its performance is the body influence. Two sets of samples were collected, with one set being obtained with the user's body near the receiving antenna (body present - BP), the other set without the body influence (body not present - BNP). A set is composed by several test runs; each test run contains 100 RSS samples. Position estimation is computed for each sample in a test run, thus no averaging was used in the tests presented.

All sample sets were taken in positions where a calibration point exists. The BP sample set is composed by 79 test runs, from which 66 were taken facing the north direction. The remaining 13 test runs were randomly chosen across the positioning area, with different orientations. The BNP sample set is composed by 12 test runs randomly chosen and do not have an orientation associated since the body is not present.

The height of the sensor nodes is the same as the anchor nodes (1.2 meters above ground). The mean and standard deviation of the absolute error (Euclidean distance between the calculated position and the true position) were the metrics chosen as performance indicators. Performance evaluation results for each algorithm are presented, in order to find the best parameter values for the experimental setup. A comparison between all positioning algorithms is also presented. The results obtained for the propagation model calibration are presented next.

4.3.1 Propagation Model Calibration

Two parameters are required to calibrate the one-slope propagation model: the RSS at the reference distance and the path loss exponent (PLE). For the first parameter, a reference distance of 1 meter was used. This is the usual choice found in literature, which simplifies computation of distances by the low power sensor nodes.

Twelve datasets of RSS measurements were collected at different distances from each of the anchors and applied equations (4.1), (4.2) and (4.3) to find the one-slope model parameters. Table 4.1 presents the data collected, where the coefficients from the one-slope model were calculated for each dataset.

The average value of each coefficient was used in the propagation model, presented in equation (4.4).

$$RSS_{OS}(d) = -37.72 - 10 \times 2.19 \times \log_{10}(d) + \chi_{\sigma} \quad (4.4)$$

The RSS measurements for the propagation model were collected with the body near the receiving antenna, and in line-of-sight (LOS) to each anchor node, which is the typical application scenario.

Table 4.1: Propagation model measurements.

Dataset	RSS at distance d_0	Exponent n
1	-30.88	3.88
2	-45.91	0.12
3	-32.18	1.81
4	-31.06	2.76
5	-36.09	3.17
6	-55.19	-0.16
7	-20.42	3.99
8	-34.76	2.72
9	-34.82	2.38
10	-47.71	1.40
11	-48.75	1.41
12	-34.84	2.74
Average	-37.72	2.19

4.3.2 Map Matching

The radio map is a representation of the propagation conditions that the algorithms were subject to. Figure 4.3 illustrates the average RSS for each of the anchor nodes obtained from all calibration points.

The plots from Figure 4.3 were obtained by averaging all calibration points in a given *x* and *y* position for all four directions. The values depicted clearly correlate with the position of the anchor nodes, where the strongest RSS values appear in the area where the anchor is located. The worst-case calibration point had a standard deviation of 6 dBm. When the distance to the transmitting antenna is the smallest and both antennas are in line-of-sight, a difference of 6 dBm in received RSS power implies a best-case scenario position variation of approximately 1 meter.

Two parameters were tested in the map-matching solution: the number of neighbours *K* and the norm used *p*. The mean error (ME) and the standard deviation (STD) are presented in Figure 4.4.

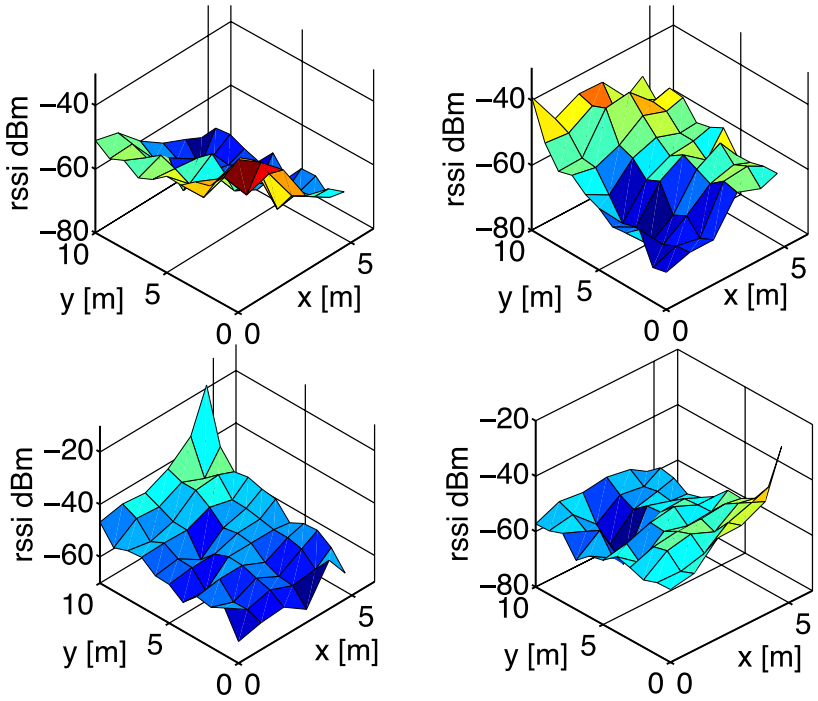

Figure 4.3: Average RSS fingerprint map.

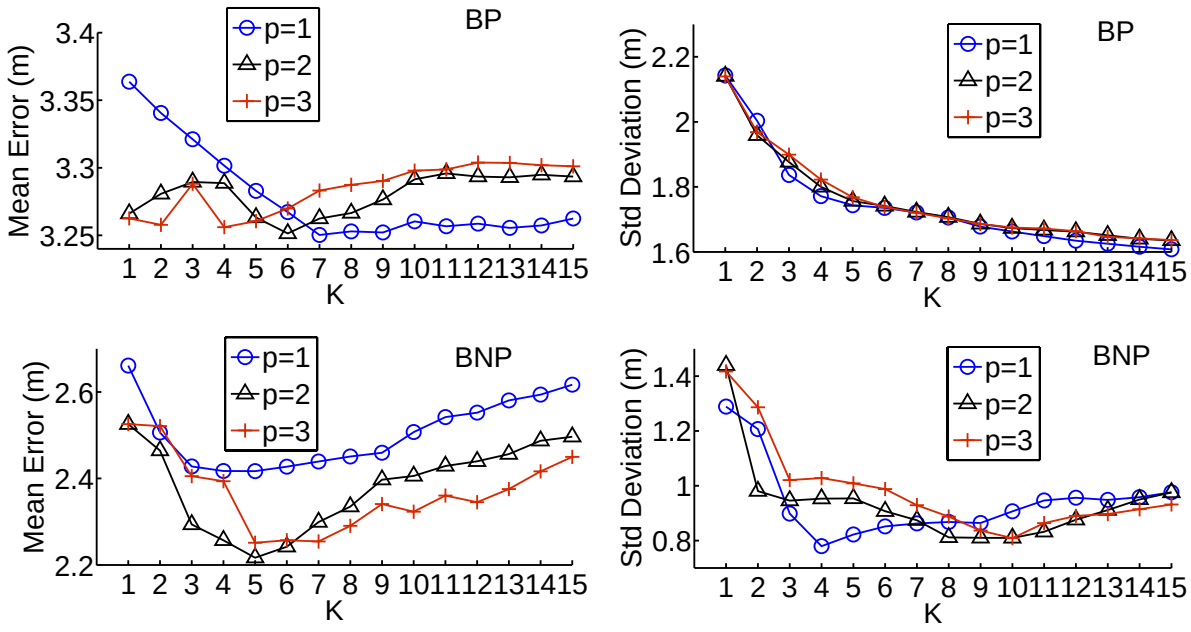

Figure 4.4: Mean and standard deviation for WKNN with different values of K and p.

The body influence is presented for each of the p-norms tested: L1-norm (Manhattan), L2-norm (Euclidean) and L3-norm. In the BP case, the ME variation between K=1, equivalent to the nearest neighbours (NN) algorithm, and the other values of K is not significant. This can be explained due to the positioning system area and calibration point density. Since the area is small (47 m^2) and the density of calibration points is high (264 calibration points), the

NN algorithm tends to perform as good as WKNN. Other works, such as [3], also pointed out this outcome, yet under a different environment. Note that a map-matching solution with NN as the positioning algorithm only needs to find one nearest neighbour, which is computationally faster than the WKNN case. A trade-off between the number *K* of neighbours and calibration point density is therefore possible when producing the radio map.

In the BNP case, the value *K* has a more important influence than in the BP case, where for *p*=2 and *K*=5, ME reaches a minimum of approximately 2.2 meters. This scenario where body influence is not present is, of course, a best-case scenario, which does not happen when the system is to be used by a person. Yet, it shows a boundary of positioning error that deterministic frameworks could provide in this environment, if accounting the body influence in the position calculation.

The STD values exhibit a monotonic decrease, with the increase of K in the BP case. Differences between norms are negligible. In the BNP case, STD values reach a minimum of 0.8 meters for *p*=1 and *K*=4.

4.3.3 Approximate Positioning

Two weights for the WCL algorithm were tested: RSS and distance using the one-slope path-loss model. For the RSS used as weight (RWCL), the exponent *e* was varied. Results are presented in Figure 4.5.

In contrast with other works [4], [5] the optimum *e* parameter was found to be between 2 (BP) to 6 (BNP), where a trade-off between the ME and the STD exists. As the parameter *e* increases beyond 4 in the BP case, and beyond 6 in the BNP case, the ME and STD also increase. With a high *e* value, the position is strongly influenced by the anchor node with the greater RSS reading. Thus, in limit conditions, the calculated position would be the same as that of the anchor node with higher RSS in the field.

Again, body influence plays a very important role. As an example, for an exponent of *e*=4, the ME in the BNP case is approximately half of the ME in the BP case. In the case of STD, an improvement of more than 50% in the BNP case is also achieved.

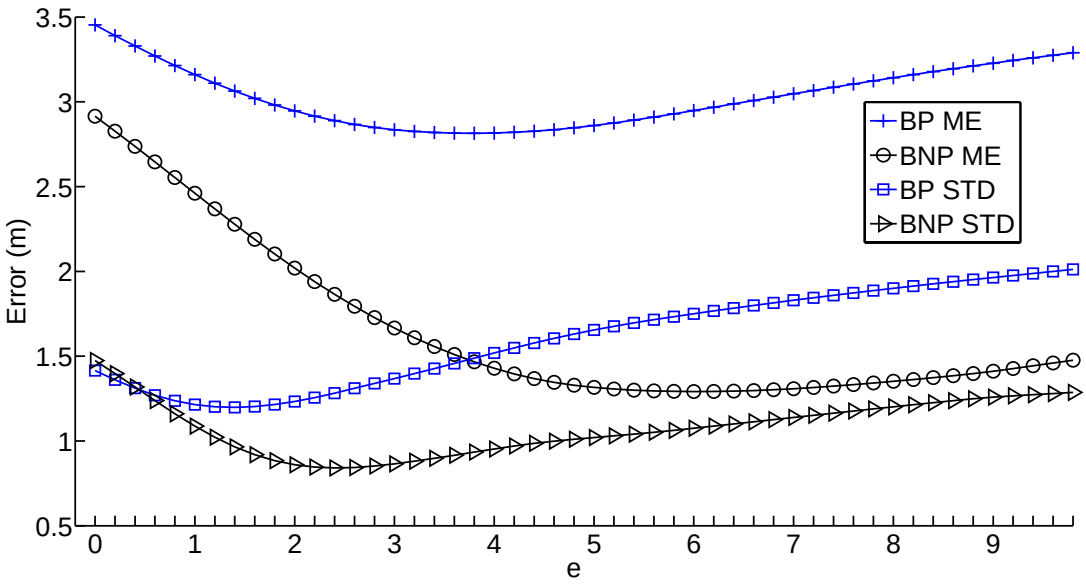

Figure 4.5: Mean and standard deviation for RWCL with different values of exponent *e*.

For the distance used as weight (DWCL), two parameters can be varied: *e* (same as in RWCL), and the PLE *n* from the one-slope model. Results are presented in Figure 4.6.

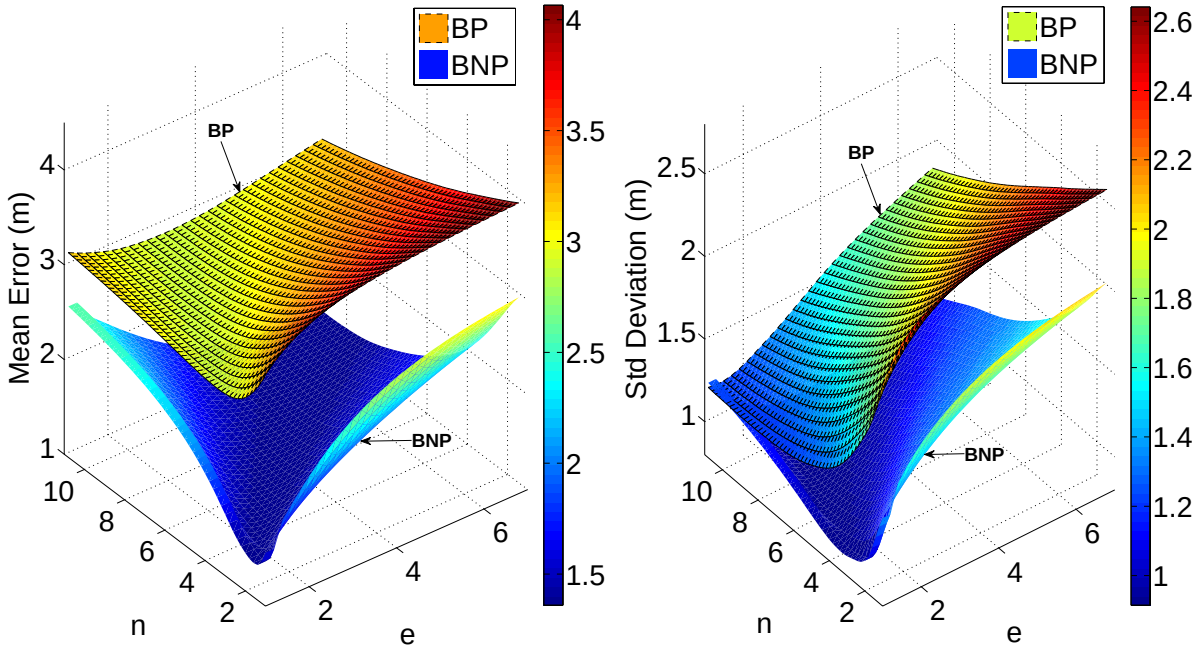

Figure 4.6: Mean and standard deviation for DWCL with different values of PLE *n* and parameter *e*.

A resolution of 0.2 in both parameters was used. Performance wise, the DWCL results are very similar to those obtained in RWCL. The minimum ME of 1.36 meters is achieved for n=2.2 and e=1.4 in the BNP case, while in the BP case, minimum ME was 2.92 meters with n=3.4 and e=1. In both the ME and the STD results, there is a balance between parameters. By increasing n, distances from the propagation model become smaller, which have more

weight. When *e* is increased, the distance from the propagation model is also increased (in module), thus balancing each other's effect. This explains the "saddle" effect in Figure 4.6, where the increase of both does not affect the performance indicators.

The value of *n*=2.2 obtained in the BNP case is also very similar to the value obtained by linear regression of *n*=2.19. This suggests that the use of linear regression is an appropriate method of determining PLE *n* when LOS conditions are assured in the PS. Under non-line-of-sight (NLOS) conditions to some anchor nodes, the optimum value of *n* tends to increase when compared with the LOS case.

4.3.4 Exact Positioning

The influence of the parameter *n* of the one-slope model, used in the RSS to distance conversion, was tested. The results for the LLS algorithm are depicted in Figure 4.7.

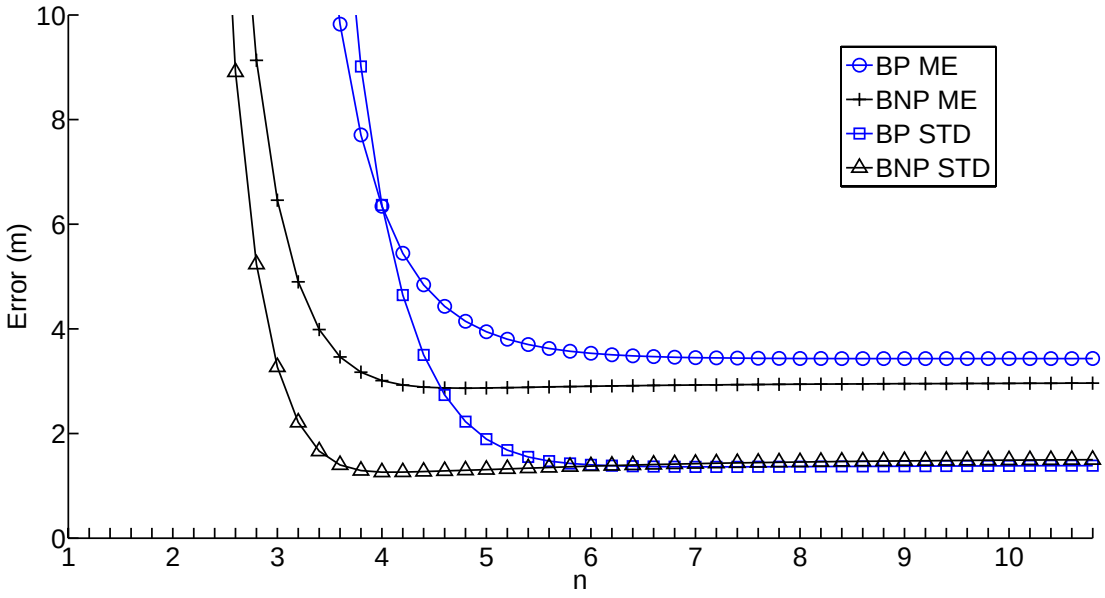

Figure 4.7: LLS mean and standard deviation for different values of PLE *n*.

Increasing the value of *n* produces a dampening effect on the error, since the estimated circumferences around each anchor node become smaller. Even though the mean error and the standard deviation decrease, the PS exhibits a saturated behaviour, since using *n*=6 is approximately the same as using *n*=10. Positioning error increases very rapidly for values of *n* smaller than 4. For a value of *n*=2.19, the one-slope model estimates the ME to around 1000 meters, which is many orders higher than the positioning area itself.

4.3.5 Algorithm Comparison

To evaluate the algorithm's sensitivity to noisy measurements, a simple simulation was made: given a set of positions (x, y) from our test setup, the real distance from all anchor nodes to each position was calculated. An error was added to this calculated distance and served as input to each algorithm that uses distances. For the RSS based algorithms, distances were converted to RSS using the inverse of the one-slope model with parameters d_0=1 m, n=2.19 and $RSS(d_0)$=-37.72 dBm. Results are presented in Figure 4.8.

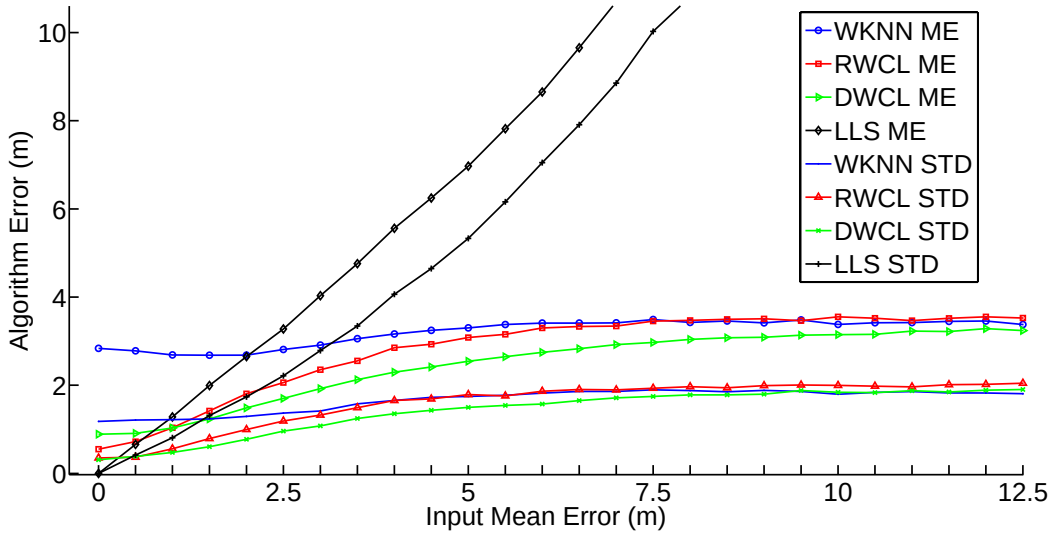

Figure 4.8: Error sensitivity comparison between algorithms tested.

Only the LLS algorithm exhibits zero error under exact distance estimates. However, the error increases rapidly with the noise in the LLS case, while the other algorithms exhibit resilience to increasingly erroneous estimates.

In order to compare the positioning algorithms, only the best parameter values for each of the algorithms used were considered. Under these best values, the cumulative distribution function (CDF) of the ME was calculated and plotted for each algorithm. To have a frame of reference when comparing algorithms, a fictitious positioning algorithm called static centre position (SCP) was added to each CDF plot. This algorithm simply returns the centre position of the PS area, for any input. The CDF for WKNN and LLS algorithms is presented in Figure 4.9.

Regarding the WKNN algorithm, the body influence is evident. In the BNP case, an error of 3 meters is achieved with a probability of around 70%, while in the BP case an error of the same magnitude is achieved with a probability of only 40%.

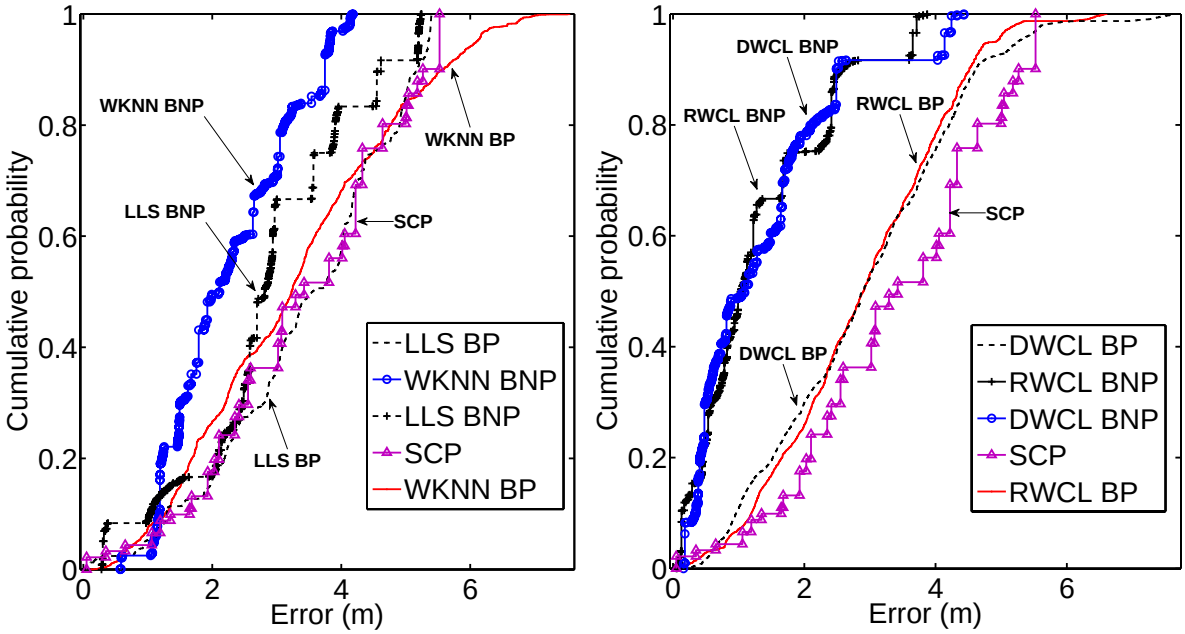

Figure 4.9: Cumulative distribution functions for all algorithms tested.

The body presence has a bigger impact on WCL than in the map-matching solution. In spite of that, the WCL algorithms present slightly better results than WKNN when under body influence. When body is not present, WCL produces the best position estimates of all algorithms tested. Considering a probability of around 70%, WCL improves from an accuracy of 4 meters in the BP case to approximately 1.8 meters in the BNP. Between RWCL and DWCL, different parameter values lead to an equivalent performance.

This implies that the use of RSS is the best weighting solution in WCL for our setup, since it is simpler than using a propagation model, avoiding the calibration phase for the propagation model parameters and the distance calculations.

In the LLS case, the body presence had less influence than the other algorithms. LLS had the worst performance, where the BNP case obtained a performance at the same level of the BP case for the other algorithms. When compared with SCP, LLS can even sometimes perform worse.

In general, WCL and WKNN have similar weak performances in the BP case. If the body influence is removed (the BNP case), WCL algorithms can perform significantly better than WKNN. In addition to this, WCL also has reduced complexity and no offline phase when compared to WKNN. Little overhead is needed to allow nodes to compute their position, since nodes only need to know the coordinates of the anchor nodes.

4.4 Discussion

Propagation models typically model large-scale fading propagation under LOS, not accounting for body influence or multipath effects. These issues severely affect the propagation models' correlation between distance and the RSS measurements. The distances estimated are severely biased, heavily depending on body orientation, LOS/NLOS condition and proximity to other objects, walls or obstructions. The comparison between the results obtained for the BP and BNP cases demonstrate how strong the body influence is. Given these observations, it is important to account for body influence when estimating the position using RSS.

Although more information from the propagation environment is embedded in the map-matching solution, which includes different body orientations, the results obtained did not compensate such effort when compared to WCL algorithm. Approximately two hours were needed to collect all calibration points in our small test environment. If a bigger area was involved, the offline phase map creation would be harder to accomplish without resorting to other mapping techniques.

The performance obtained from the WCL solutions is equivalent to the map-matching solution in the BP case. WCL solutions provided the best position estimates in the BNP case. From the results obtained, the RWCL provided overall better results than map-matching, with the advantage of having lower complexity and easier setup. Approximate positioning algorithms tend to perform better in this kind of environment due to its error resilience. In the case of DWCL, in spite of using a propagation model calibrated to the specific test scenario, using the distance as weight did not improve position estimates when compared to simply using the RSS parameter.

Under exact distance measurements, the LLS technique yields the exact position. However, under erroneous distance measurements, the LLS performance is greatly affected. The LLS solution provided the weakest results, due to distances rarely being correctly estimated under our indoor test scenario. Clearly, LLS algorithm cannot be used with RSS methods in such an environment. It needs more accurate methods to detect distance between nodes and cannot be used as positioning algorithm when such are unavailable.

The algorithms tested showed poor positioning capabilities in our setup scenario when the body influence is present. When the body influence is not present, positioning accuracy

improves significantly, with the exception of LLS, which performs approximately the same as the SCP. Between all three types of positioning algorithms, body influence was small in the LLS case, medium in the map matching solution, and highest in the WCL algorithms.

Anchor node placement is a very important issue in RSS positioning systems that has not been addressed here. A minimum number of anchor nodes were employed, with an anchor node placement assuring always a total of four non-collinear points. Increasing the number of anchor nodes in the positioning area is another solution to further reduce positioning error. This measure needs to be taken with caution, since increasing number of anchor nodes also increases algorithm complexity, especially in the case of WKNN.

4.5 References

[1] T. Instruments, 'CC253x System-on-Chip Solution for 2.4-GHz IEEE 802.15.4 and ZigBee® Applications', 2012.

[2] Antenova, 'Titanis 2.4 GHz Swivel SMA Antenna Product Specification', 2015.

[3] V. Honkavirta, T. Perala, S. Ali-Loytty, and R. Piche, 'A comparative survey of WLAN location fingerprinting methods', in *2009 6th Workshop on Positioning, Navigation and Communication*, 2009, vol. 2009, pp. 243–251.

[4] J. Blumenthal, R. Grossmann, F. Golatowski, and D. Timmermann, 'Weighted Centroid Localization in Zigbee-based Sensor Networks', *2007 IEEE International Symposium on Intelligent Signal Processing*, pp. 1–6, 2007.

[5] F. Reichenbach and D. Timmermann, 'Indoor Localization with Low Complexity in Wireless Sensor Networks', *2006 IEEE International Conference on Industrial Informatics*, pp. 1018–1023, Aug. 2006.

Chapter 5

Body Effect in RSS Based Positioning

The influence of the human body in antenna systems has significant impact in the received signal strength (RSS) of wireless transmissions. Accounting for body effect is generally considered as being able to improve position estimation based on RSS measurements. As such, the work from the previous chapter is augmented with the information of user orientation. By inferring the user's orientation we are effectively inferring line-of-sight (LOS)/non-line-of-sight (NLOS) conditions between sensor and anchor nodes. With this information, this work seeks to assess if accounting for body influence can improve the position estimate under indoor conditions.

Several measurements were performed within the experimental setup scenario, where the sensor node is now equipped with an inertial measurement unit (IMU) containing inertial and magnetic sensors. A model of the RSS attenuation induced by the body is created using experimental measurements collected in a controlled environment and applied in real-time to the positioning system. The body attenuation model enables the compensation of RSS

measurements collected by the sensor node, by taking into account attenuation effects from NLOS and body proximity.

A real-time path loss exponent (PLE) estimation method using RSS information from neighbour anchors is also implemented and evaluated. The weighted centroid localization (WCL) is chosen in this work as the positioning algorithm, since it provided the best results in the previous chapter. The performance of WCL is evaluated to assess the effect produced by incorporating the body effect into the localization algorithm.

5.1 Hardware Platform

The CC2530 development kit from the previous chapter was used in this work. The anchor nodes are the same as in the previous chapter, while the sensor node has been redesigned. The sensor node was replaced by an evaluation module and two extra boards, one board containing the battery and the sensor platform (containing inertial and magnetic sensors, such as the sensor node described in [1]), and the other board containing a secure digital card (SDC) to store data. These boards are interconnected through 20-pin header connectors, allowing a modular approach for rapid prototyping.

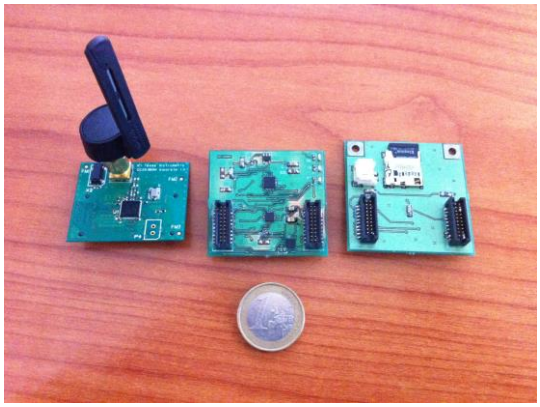

Figure 5.1: Sensor node prototype. The CC2530 module is shown on the left, the sensor and battery board in the middle and the SDC board on the right.

The sensor platform integrates an InvenSense MPU6000 [2] with a Honeywell HMC5883L [3]. The MPU6000 embeds an accelerometer, a gyroscope and allows integration with an external sensor via I^2C (inter-integrated circuit) protocol. The noise figures are 0.005 º/s and 400 μg at 10 Hz for the gyroscope and accelerometer respectively. The HMC5883L magnetic sensor noise is 5 milli-gauss. The MPU6000 collects samples from each sensor and stores them in a first-in-first-out (FIFO) buffer. We used a sampling frequency of 100 Hz. The

data stored in the FIFO from all three sensors are read using the serial peripheral interface (SPI) protocol in a single burst at a 1 MHz clock frequency, using the serial port and the direct memory access (DMA) controller from the CC2530.

When the term IMU is used from now on, it will refer to this sensor setup composed of accelerometer, gyroscope and magnetometer, which enable the determination of device's orientation. The data collected from the RSS and the IMU is stored in a file on the SDC for offline processing in MATLAB.

5.2 Orientation Measurement

Only the accelerometer and magnetometer sensors were used to determine orientation in this work. Prior to measuring orientation, a calibration procedure is performed to compensate for offsets in the sensors. The minimum and maximum value of each axis is obtained by manually aligning the sensing axis with gravity, for the calibration of the accelerometer, and the magnetic north for the calibration of the magnetometer. The minimum and maximum values are then used in equation (5.1) to produce uniform values from -1 to 1:

$$u = \frac{Reading - Min}{\frac{Max - Min}{2}} - 1 \tag{5.1}$$

A tilt-compensated e-compass method using rotation quaternions was implemented to determine orientation. Figure 5.2 depicts the sensor coordinate system used in the IMU.

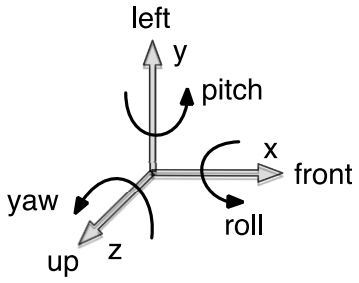

Figure 5.2: Sensor coordinate system

The orientation measurement consists in finding the Euler angles (roll, pitch and yaw*)* between the sensor coordinate system and the global coordinate system, where gravity is aligned with the –*z*-axis and the projection of the magnetic north in the azimuth plane is aligned with the +*x*-axis. First the roll and pitch angles are computed with the accelerometer data, using equations (5.2) and (5.3):

$$roll = tan^{-1}\left(\frac{-g_y}{-g_z}\right) \tag{5.2}$$

$$pitch = tan^{-1}\left(\frac{g_x}{\sqrt{g_y^2 + g_z^2}}\right) \tag{5.3}$$

where g_x, g_y and g_z are the normalized gravity vector components, which are measured by the accelerometer sensor when there are no external forces acting on the sensor node. Using the *atan2* and *atan* methods in MATLAB for roll and pitch angles respectively produces angles in canonical form. Roll varies between ±180º and pitch varies between ±90º. Two rotation quaternions are created using equations (5.4) and (5.5), for the roll and pitch angles obtained from the accelerometer readings.

$${}^{b}_{w}\boldsymbol{q}_{\boldsymbol{roll}} = \left(\cos\frac{roll}{2}, \sin\frac{roll}{2}, 0, 0\right) \tag{5.4}$$

$${}^{b}_{w}\boldsymbol{q}_{\boldsymbol{pitch}} = \left(\cos\frac{pitch}{2}, 0, \sin\frac{pitch}{2}, 0\right) \tag{5.5}$$

The notation ${}^{b}_{w}\boldsymbol{q}$ denotes the quaternion $\boldsymbol{q}$ that rotates from the body frame (b) to the world frame (w) (or inertial frame) aligned with the gravity and the magnetic north vectors.

The tilt rotation quaternion is computed by simply multiplying the pitch and roll quaternions.

$${}^{b}_{w}\boldsymbol{q}_{\boldsymbol{tilt}} = {}^{b}_{w}\boldsymbol{q}_{\boldsymbol{roll}} \otimes {}^{b}_{w}\boldsymbol{q}_{\boldsymbol{pitch}} \tag{5.6}$$

The yaw angle is computed by first applying the inverse of the tilt rotation, which brings the magnetic vector into the azimuth plane:

$$\boldsymbol{h} = {}^{b}_{w}\boldsymbol{q}_{\boldsymbol{tilt}} \otimes (0, \boldsymbol{m}) \otimes {}^{b}_{w}q^{*}_{tilt} \tag{5.7}$$

where the magnetic vector $\boldsymbol{m}$ is converted to a quaternion with scalar part equal to zero. The yaw angle is then computed using equation (5.8):

$$yaw = tan^{-1}\left(\frac{-h_y}{h_x}\right) \tag{5.8}$$

where h_x *and* h_y are the normalized rotated version of the magnetic vector components. The yaw angle is computed using the *atan* method and varies between ±180º. Finally a rotation quaternion is created using half of the yaw angle:

$${}^{b}_{w}\boldsymbol{q}_{\boldsymbol{yaw}} = \left(\cos\frac{yaw}{2}, 0, 0, \sin\frac{yaw}{2}\right) \tag{5.9}$$

Multiplying the yaw quaternion by the tilt quaternion produces the full orientation of the sensor node in quaternion format:

$$ {}^{b}_{w}\boldsymbol{q_f} = {}^{b}_{w}\boldsymbol{q_{tilt}} \otimes {}^{b}_{w}\boldsymbol{q_{yaw}} \tag{5.10} $$

5.3 Path Loss Estimation

When deploying a wireless sensor network (WSN) in an indoor environment, PLE estimation is accomplished by performing several power measurements at different distances from a transmitting node. These measurements are then used to compute a best-fit constant value for the PLE parameter, to be used in the positioning area. This task was performed in the previous chapter. Here a different approach is explored, which uses the distance information that is configured in the anchor nodes of the positioning system. Given that each anchor is assigned a location, distances between anchors are known. Since nearby anchor nodes also receive the beacons broadcasted, a PLE estimate can be obtained from this information.

In the previous chapter, anchor nodes were configured to send beacon messages periodically (100-millisecond superframe). The anchor nodes in this work were configured to additionally include RSS information from other anchor nodes in the beacon messages. During a superframe, the sensor node will receive one beacon message from each anchor node, with each beacon message containing a list of RSS readings that the respective anchor node received from other anchor nodes in communication range. With RSS and distances between anchor nodes, path loss exponent estimation for each link is obtained using equation (5.11), which is derived from the one-slope model (equation (2.12) from chapter 2).

$$ n = \frac{R_A - P_0}{-10 \cdot log_{10}(d)} \tag{5.11} $$

where R_A is the RSS received by the anchor node for a specific link and P_0 is the RSS at the reference distance of 1 meter. Assuming that all four anchor nodes from our positioning scenario have full connectivity, each anchor will capture RSS from all other three anchors and broadcast this information in the beacon message. The sensor node uses this information to infer the PLE for each anchor. Figure 5.3 depicts an iteration of the algorithm, to which we refer to as closest link path loss (CLP). First the sensor node computes the initial position estimate using the RSS received from the anchor nodes using WCL algorithm. This initial

position estimate, together with the known anchor coordinates is used to find the node and anchors displacement vectors (vectors 2,1 2,N 2,3 and 2,4 in Figure 5.3).

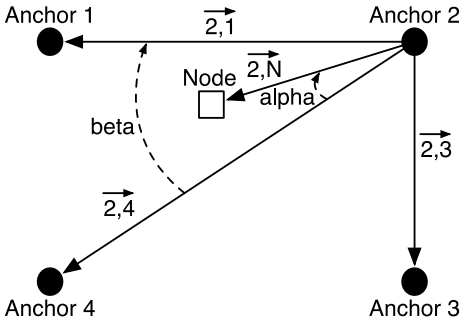

Figure 5.3: Closest link path loss algorithm iteration example for anchor 2.

Using the cross product rule with the *z* component set to zero, the area of the parallelograms formed by each anchor displacement vector and the node displacement vector are computed. The two smallest areas are chosen, which correspond to the links closer to the node's initial position estimate. Next, a linear interpolation is used to find the PLE of the sensor node's link to the anchor, by using the angle between the two closest links (beta angle) and the angle between one of the links and the user displacement vector (alpha angle). The angles are computed using the dot product and a linear interpolation is used to find the PLE using equation (5.12).

$$n = n_{i,1} \times \frac{\beta - \alpha}{\beta} + n_{i,2} \times \frac{\alpha}{\beta} \tag{5.12}$$

where $n_{i,1}$ and $n_{i,2}$ are the PLEs of the closest links to the node's estimated position, beta is the angle between the closest links, and alpha is the angle between one of the closest links and the user displacement vector. This PLE (n) represents the state of link attenuation from the previous superframe, and allows estimation of the distance between the sensor node and the respective anchor node by using equation (5.13), which also derives from the one-slope model:

$$d = 10^{\left(\frac{R_S - P_0}{-10n}\right)} \tag{5.13}$$

where *Rs* is the RSS received by the sensor node, P_0 is the RSS at the reference distance and n is the PLE obtained from equation (5.12). This procedure is repeated for each anchor node, and the distances obtained for each anchor are then used in the WCL algorithm to estimate the position of the sensor node.

The goal associated with this procedure is to use as much RSS information as possible, in order to capture path loss changes caused by the user's body or the dynamic environment.

5.4 Evaluation of Body Effect in RSS

Body effect experiments were carried out in two different environments, the positioning area of 4.7 m by 10 m (approximately 50 m^2) used in the previous chapter and an anechoic chamber. Figure 5.4 details the anechoic chamber setup.

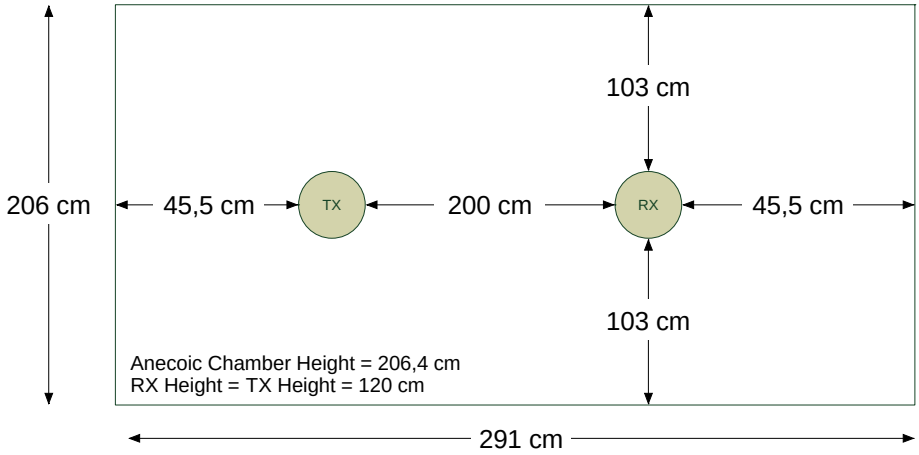

Figure 5.4: Anechoic chamber setup.

To evaluate body effect on RSS, three sets of measurements were collected: static with body influence (case 1), where the device is placed on the user's body while the user is standing still; static without body influence (case 2), where the device is placed on top of a plastic stand; and dynamic (case 3), where the device is placed on the user's body and the user performs a 360º rotation. For all scenarios the device is always placed at waist level, 1.2 m above the ground. The goal is to distinguish between device effects (hardware effects such as antenna placement in the device and radiation pattern) and body effects, as well as between static and dynamic situations.

The anechoic chamber tests provide a controlled environment without external interferences. It allows us to determine the multipath and shadow fading caused by the body alone, since other multipath components from wall and ground reflections are severely attenuated or non-existent in this type of environment. The positioning scenario tests provide real data for comparison with controlled environment data.

Data capture is accomplished by the sensor node, which receives messages from a transmitter node placed at the same height and at a distance of 2 m. The sensor node simply stores the RSS values from the received messages and the raw IMU data in a file on the SDC.

5.5 Attenuation Model

We consider that the RSS that the sensor node receives from each anchor node is influenced by the user's orientation according to an attenuation model that relates the relative attenuation with the user's orientation. First, a reference orientation relating the positioning setup coordinate system to the global coordinate system is required (e.g., the positioning setup coordinate system offset relative to the magnetic north). This reference orientation was initially measured in our positioning scenario. To find the relative angle between the user's orientation and an anchor node, the user location on the positioning scenario is also needed. If the WCL algorithm is used to find this position, an additional error is added in the relative angle estimation and therefore, to avoid this additional error, the real position logged during the data collection phase (such as in the map-matching offline phase of the previous chapter) was used in order to compute the anchor direction. This allows the inclusion of orientation information with a much smaller error than using WCL to find position, which can be seen as a best-case scenario where orientation information is the best possible.

Anchor direction relative to the sensor node is found using equation (5.14), by computing the difference between the location of the sensor node $\boldsymbol{p_s}$ and the location of the anchor node $\boldsymbol{p_a}$.

$$\boldsymbol{a} = \boldsymbol{p_s} - \boldsymbol{p_a} \tag{5.14}$$

The orientation of the sensor node is corrected by multiplying the IMU orientation quaternion by another quaternion representing the north offset angle, measured in the positioning setup coordinate system using equation (5.15).

$$\boldsymbol{{}^{b}_{w}q_c} = \boldsymbol{{}^{b}_{w}q_{imu}} \otimes \boldsymbol{{}^{b}_{w}q_{offset}} \tag{5.15}$$

With both the world (inertial) coordinate frame and the local coordinate frames of the positioning area aligned, the sensor node's forward direction is obtained by multiplying the resulting rotation quaternion by a 3D vector pointing in the *x*-axis direction (i.e., 0º roll, 0º pitch and 0º yaw), using equation (5.16):

$$\boldsymbol{b} = \boldsymbol{{}^{b}_{w}q_c} \otimes (0, \boldsymbol{d}) \otimes \boldsymbol{{}^{b}_{w}q_c^{*}} \tag{5.16}$$

where $\boldsymbol{d}$ is the *x*-axis direction vector (i.e., vector [1,0,0]) forming the vector part of a quaternion with zero scalar part and $\boldsymbol{{}^{b}_{w}q^{*}_{c}}$ is the quaternion conjugate. The scalar part of quaternion $\boldsymbol{b}$ from equation (5.16) is discarded and the 3D orientation vector is given by the vector part. Discarding the *z* component of the 3D vector representing the sensor direction, the relative angle between sensor and anchor direction is simply given by the angle between two vectors:

$$\alpha = cos^{-1}\left(\frac{\boldsymbol{a}\cdot\boldsymbol{b}}{\|\boldsymbol{a}\|\cdot\|\boldsymbol{b}\|}\right) \tag{5.17}$$

$$r = \boldsymbol{a}\times\boldsymbol{b} \tag{5.18}$$

Vectors **a** and **b** represent anchor direction and sensor direction respectively. Since the angle will always be the smallest angle between both vectors, multiplying the angle by the sign of the rotation axis produces absolute orientation. The angle produced by equations (5.17) and (5.18) will be used to lookup the attenuation value of the model collected in the anechoic chamber. A linear interpolation is used when no information is available for the angle detected by the sensor node (e.g., between two points in the attenuation model).

5.6 Results

This section presents the results for the experiments carried out in the proposed scenarios. RSS data collected to study the body effect is presented in polar plots. Units for RSS data are dBm and angles are in degrees. Regarding positioning algorithm performance, the parameters found in the previous chapter, which maximize WCL accuracy, were used as default parameters in this work. When using the raw RSS readings for WCL the exponent *e* was set to 3.4 (same as RWCL in the previous chapter). For distances (obtained from the one-slope model) being used as weights in CLP the exponent *e* of 1 and the reference power P_0 of -37.72 were used (same as DWCL in the previous chapter). The performance indicator chosen is the Euclidean distance between real position and estimated position. Cumulative distribution functions and geographical error distributions are presented for each algorithm, with and without body effect compensation.

5.6.1 Body Effect in RSS

A manual orientation measurement was performed inside of the anechoic chamber, using markers placed in the floor. For the positioning scenario, orientation is obtained using

the IMU after performing the calibration procedure. The sensor node is either fitted to the user at waist level in case 1 (static with body influence) and case 3 (dynamic with body influence) or placed on top of a plastic stand in case 2 (static without body influence) at the same height (1.2 meters) as the user's waist. Rotations are performed along the vertical axis (*z*-axis) in a counter-clockwise direction, with 0º being the orientation facing the anchor node (LOS) and 180º being the opposite direction (NLOS). Due to space constraints inside the anechoic chamber, the distance between sensor and anchor nodes was fixed to 2 meters in both test scenarios. For cases 1 and 2, the sensor node is oriented accordingly, and 100 RSS samples are collected. For case 3, the user performs a 360º turn during approximately 60 seconds. Since the sensor is placed at waist level, some interference is expected due to the arms when the body is present (cases 1 and 3). The user's arms were in a resting position along the torso. Results are summarized in Figure 5.5, where RSS values are presented. The body effect experiments in the positioning scenario were performed with a minimum distance to the walls of 2 meters.

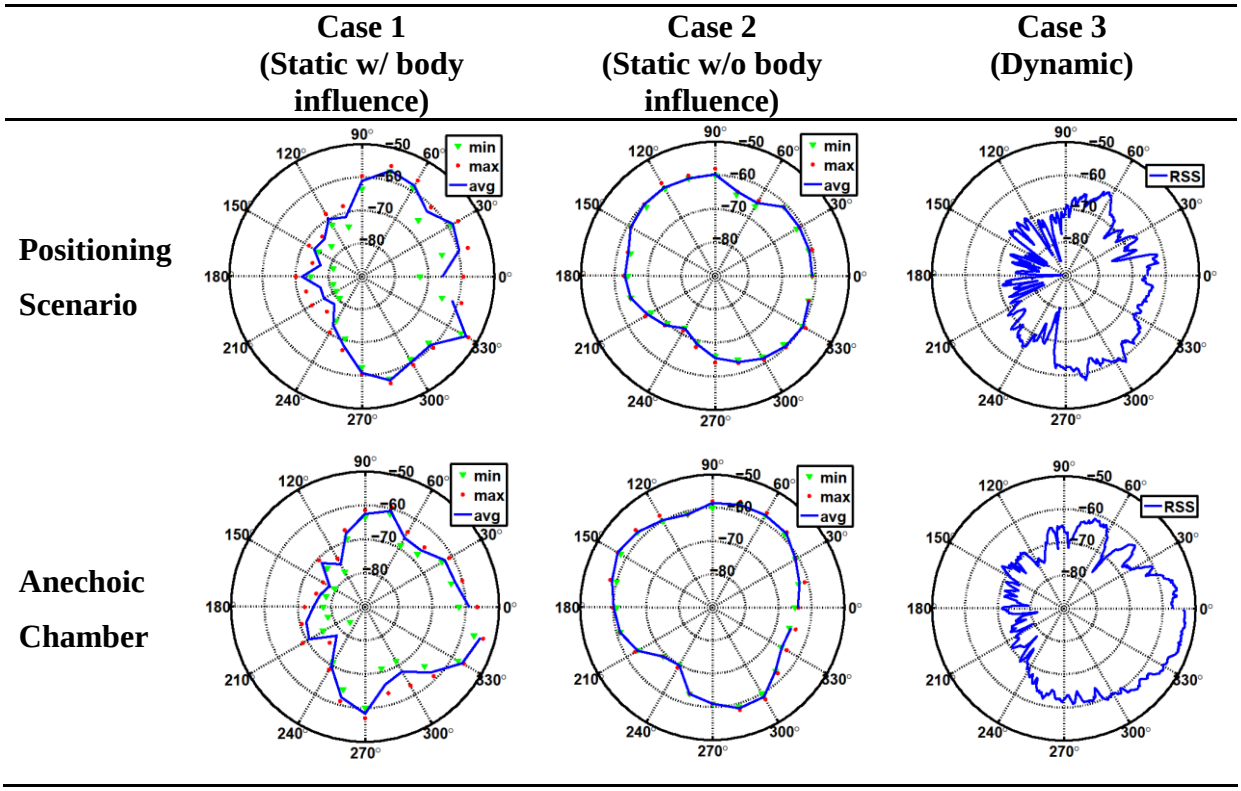

Figure 5.5: Effect of the human body on the RSS under different scenarios.

There is a clear trend in the summarized plots from Figure 5.5, where higher RSS attenuation can be seen whenever the body is blocking the LOS. Both scenarios from cases 1 and 3 exhibit this NLOS effect for orientations between 90º and 270º.

The RSS levels depicted in the anechoic chamber and positioning scenarios of case 2 are a function of antenna radiation pattern, antenna placement in the PCB and scenario conditions. There is minimum practical difference between both scenarios in case 2, implying that for our positioning scenario, the minimum distance of 2 meters to the walls is sufficient for signals reflecting of the walls not to be detected by the receiver, and thus not influence the positioning algorithm error. These reflections are dependent on wall material, which has been studied in works such as [4] and is outside the scope of this work.

The RSS variance increases significantly in case 3 when compared with the other cases, due to the user's motion during the test. It is important to note that the RSS variance increases for both scenarios under dynamic conditions. In the case of the positioning scenario, these variations are generally higher.

The body effect data collected does not appear to agree with superposition of attenuation effects, since the attenuation profile observed in static conditions when the body effect is present is not identifiable in the case where the body is not present.

The RSS variance exhibited in the plots from Figure 5.5 is solely due to the user's body, which is the only source of motion in the experiments. When the user's body is removed from the test scenarios, plots for minimum, maximum and average RSS overlap, which indicates that no variations occurred.

The data collected from the anechoic chamber scenario was used to create the body attenuation model presented in Figure 5.6.

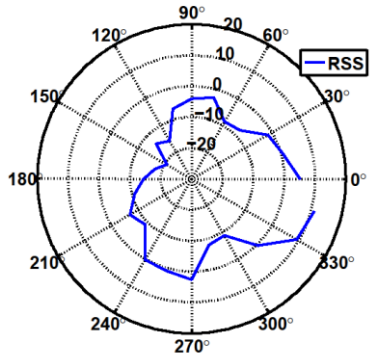

Figure 5.6: Body attenuation model (units are in dB).

The attenuation model is the result of a combination of multipath and shadowing propagation conditions imposed by the presence of the body inside the anechoic chamber. The model is effectively the difference between the RSS obtained when the body is near the receiving node (case 1) and the RSS obtained when the body effect is not present (case 2).

5.6.2 Body Effect in Algorithm Performance

The body attenuation model obtained in the previous section is used in this section by adding the corresponding RSS attenuation value to the RSS received from each anchor node, according to the angle between the user's orientation and the anchor node direction. These compensated RSS values are then served to the positioning algorithm and a new estimate of position is computed.

In order to experimentally study the body effect in algorithm performance, three sets of data were collected in the positioning scenario. The first set was collected with the sensor node held in the user's hand at approximately 20 cm away from the body (referred to as off-body-20 dataset). The second set was collected with a distance between body and sensor node of 10 cm (referred to as off-body-10 dataset). The last set was collected with the sensor node attached to the user's body at waist level using a Velcro strap (referred to as on-body dataset). These datasets were served as inputs to the WCL and CLP algorithms, generating output estimates without the body effect compensation (WCL and CLP), with the body effect compensation using the true position logged during data collection (WCL+B true pos and CLP+B true pos) and with the body effect compensation using WCL to produce the initial position estimate (WCL+B est pos and CLP+B est pos). Datasets were collected in different days, at approximately the same hour of the day. Algorithm performance for the off-body-20, off-body-10 and on-body datasets is presented in Figure 5.7, Figure 5.8 and Figure 5.9 respectively.

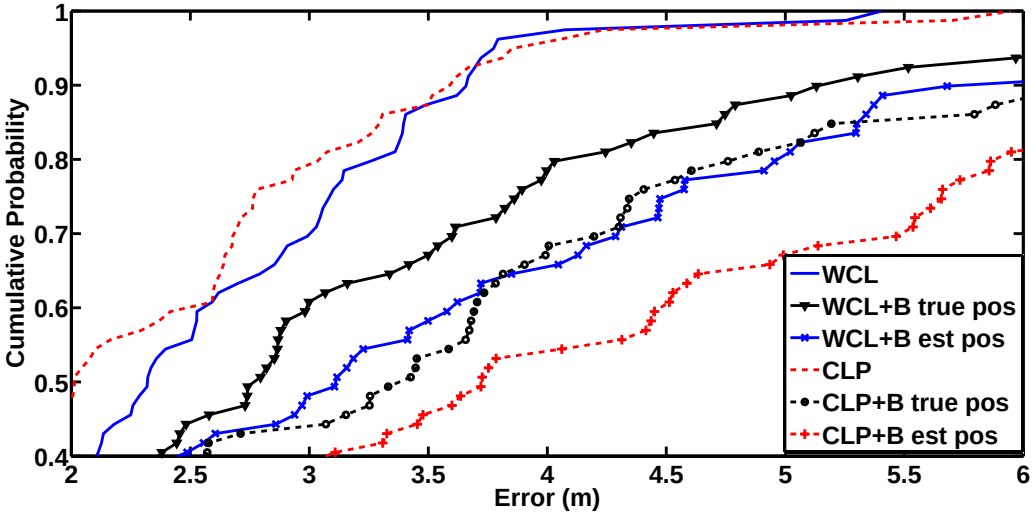

Figure 5.7: Performance results for the off-body-20 dataset.

The results obtained for the off-body-20 dataset show that the position estimated by each algorithm worsens when the body orientation is accounted, with WCL+B using the true position degrading from 3.03 m to 3.61 m (+19%) compared to WCL, and CLP+B using the true position degrading from 2.69 m to 4.3 m (+59%) compared to CLP, analysing performances at 70% probability. A lower performance was expected using the estimated position, compared to the true position, when inferring orientation, which is consistent with the results, as can be seen in Figure 5.7.

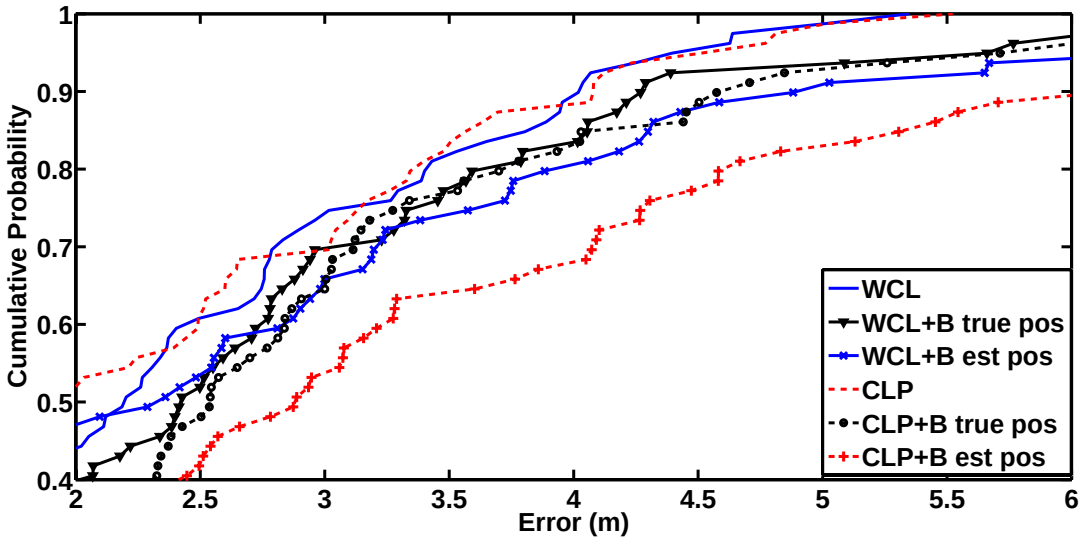

Figure 5.8: Performance results for the off-body-10 dataset.

The off-body-10 dataset also consistently presented worse performance when accounting body orientation, yet with lesser impact than in previous dataset. WCL+B using the true position degraded from 2.83 m to 3.22 m (+13%) compared to WCL, and CLP+B using the true position produced slightly worse results, from 3.02 m to 3.12 m (+3%), compared to CLP, when analysing performance at 70% probability. Using the estimated position to infer orientation had lesser impact in performance for this dataset, compared to the previous dataset, although still presenting worse performance. WCL actually performed better in the off-body-10 dataset than in the off-body-20 dataset, which was contrary to our expectations. The algorithms that account for the body effect improved when compared to their performances in the previous dataset, yet still presenting worse performance than the simpler versions that don't account the body influence.

Results for the on-body dataset scored the lowest positioning accuracy from all datasets. On the other hand, there were improvements when comparing individually each algorithm with its body effect counterpart, with WCL+B using the true position improving

from 3.85 m to 3.6 m (-6%) compared to WCL, and CLP+B improving from 4.36 m to 3.61 m (-17%) compared to CLP, at 70% probability. Using the estimated position for the body effect compensation did not improve the location estimates obtained by WCL and CLP algorithms.

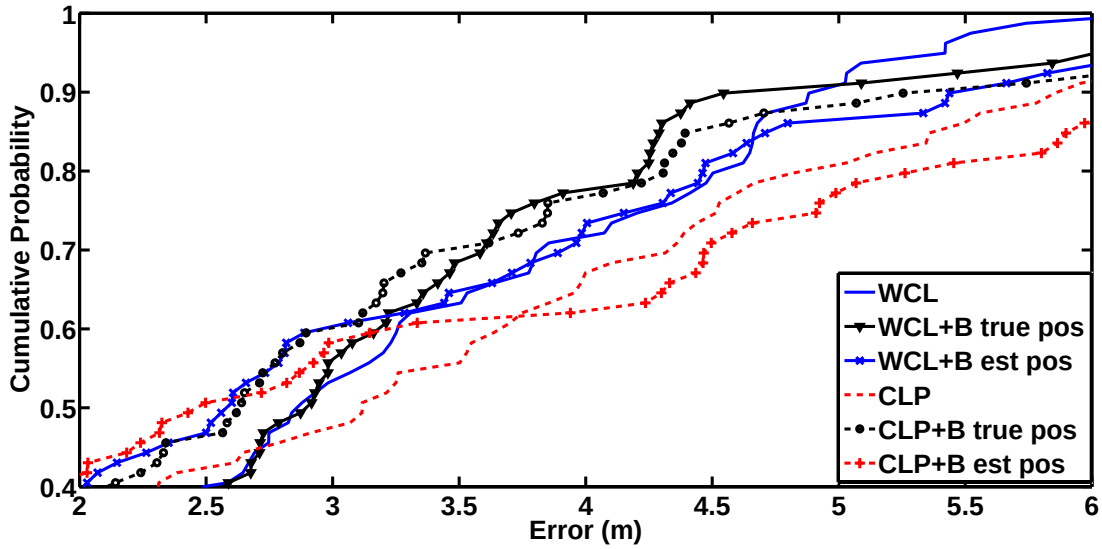

Figure 5.9: Performance results for the on-body dataset.

Overall, for the off-body-20, off-body-10 and on-body datasets, CLP (with an accuracy of 2.69 m, an improvement of 11% compared to WCL), WCL (with an accuracy of 2.83 m) and WCL+B using the true position (with an accuracy of 3.6 m, an improvement of 6% compared to WCL), respectively, presented the highest accuracy marks under our test conditions at 70% probability. When comparing WCL and CLP to their counterparts that account the body influence using the estimated position, which is the real use case scenario, the body attenuation model consistently worsened the accuracy. On-body dataset showed lesser degradation of accuracy (in the order of 3%), off-body-10 showed average degradation of accuracy (14% and 35% for WCL and CLP respectively) and off-body-20 showed higher degradation of accuracy (42% and 105% for WCL and CLP respectively). Results are summarized in Table 5.1.

Table 5.1: Algorithm performance results for 70% cumulative probability.

	WCL	**WCL+B true pos**	**WCL+B est pos**	**CLP**	**CLP+B true pos**	**CLP+B est pos**
Off-Body-20	3.03m	3.61m	4.31m	2.69m	4.3m	5.53m
Off-Body-10	2.83m	3.22m	3.23m	3.02m	3.12m	4.09m
On-Body	3.85m	3.6m	3.96m	4.36m	3.61m	4.49m

In Figure 5.10, Figure 5.11 and Figure 5.12, the geographical distribution of the positioning error is presented for each algorithm, with respect to the off-body-20, off-body-10 and on-body datasets, respectively. The tests were performed with only one user inside the area. If more users were present, the error distribution would certainly generate different error patterns.

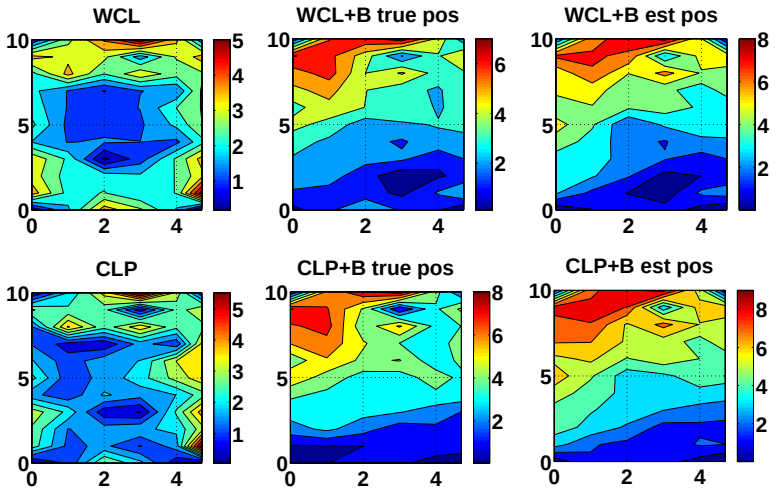

Figure 5.10: Geographical distribution of positioning error for off-body-20 dataset. Axes are in meters.

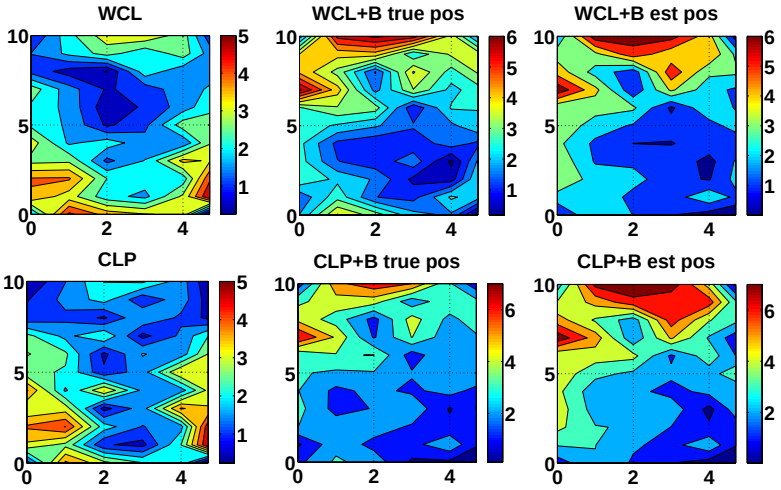

Figure 5.11: Geographical distribution of positioning error for off-body-10 dataset. Axes are in meters.

It is clear from the geographical error distributions that different positions are subject to different error magnitudes due to the propagation conditions of the scenario. Differences in error distributions are larger between datasets and smaller across positioning algorithms. Overall, the error is generally smaller near an anchor node and larger further away. The centre of the positioning area also has a tendency to exhibit lower error.

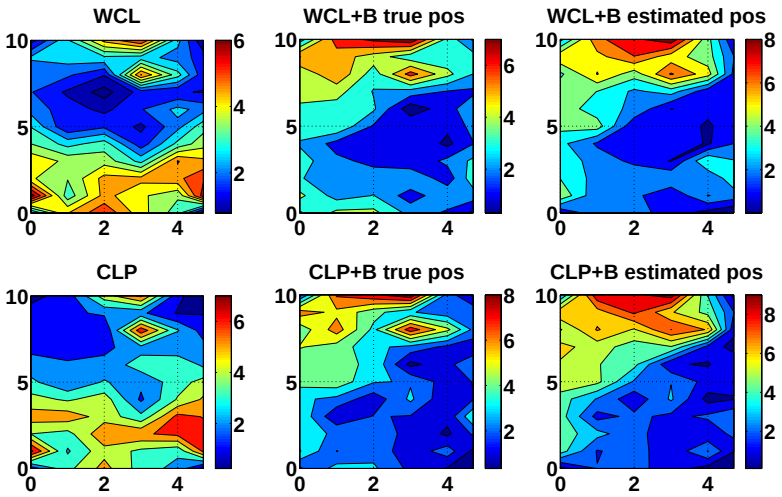

Figure 5.12: Geographical distribution of positioning error for on-body dataset. Axes are in meters.

As a final result presented in this section, the difference between the RSS received by the sensor node and a theoretical RSS that would have been received by the sensor node in ideal conditions were computed, in order to show the RSS deviation from the empirical model that is encountered in the field. Using the real position of the sensor node logged during data collection and the one-slope model, theoretical RSS values were computed for each anchor using the real distances. For this calculation the PLE n=2.19 and P_0=-37.72 dBm parameters found in the previous chapter were used. The probability distributions (calculated using the *ksdensity* method from MATLAB) for the body attenuation model and the RSS difference for all three datasets are depicted in Figure 5.13. The body attenuation distribution was also plotted for comparison.

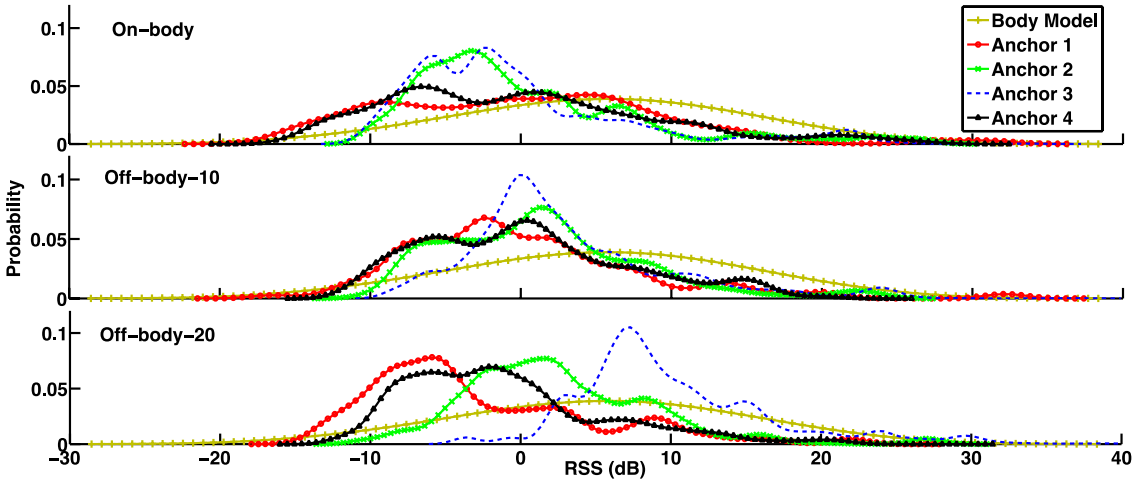

Figure 5.13: Probability distributions for the difference between real and theoretical RSS received from anchor nodes. Body attenuation model distribution is plotted for comparison

In the case of the on-body dataset, the distributions of anchors 1 and 4 are similar to the distribution of the body model, which is related to the improvements seen in this dataset when accounting body influence. Distributions for anchors 2 and 3 differ significantly from the body model, meaning that while anchors 1 and 4 are generally correctly compensated using the body model, anchors 2 and 3 deteriorate the distance estimate. For the off-body-10 and off-body-20 datasets, differences between the model and anchors are bigger, which explain why the body influence compensation produced worse results compared to not accounting body influence. It can also be seen that RSS difference is more closely approximated by tailed distributions, rather than Gaussian, as is generally assumed due to the central limit theorem.

5.7 Discussion

In the previous chapter, the WCL algorithm was tested with and without body influence in the same positioning scenario as in this work, and the performance was improved from 4.0 m to 1.8 m (for a 70% probability) when the body was removed from the scenario, a 55% improvement in position accuracy. Body influence in RSS is widely known to induce error in the position estimation. Accounting for body influence, such as in [5], provided a major impact, improving location estimates. In order to remove or minimize this bias effect caused by the body in the previous chapter, a body attenuation model was created and applied in the same positioning scenario.

Considering the best-case scenario (when the body attenuation model was applied using the true position to estimate orientation), only minor improvements on the positioning error were obtained for the on-body dataset. For the datasets where the sensor node is distanced from the body, the body attenuation model consistently deteriorated the performance. This could be explained due to the model being created using on-body data and, as such, it was more likely to produce better results when applied to the on-body dataset. However, this best-case scenario cannot be used in a real use-case (which would use the estimated position to infer orientation), since the body attenuation model consistently deteriorates accuracy in all datasets, despite the controlled environment with only the user in the positioning area. These results suggest that the shadowing component caused by the body plays a minor role in the RSS when compared to the multipath component imposed by the environment. The higher attenuation found in the positioning scenario also stands in agreement with this suggestion.

The distance from the sensor node to the user's body is an important parameter, as evidenced by the differences in performance between datasets. The closer the sensor node is to the body, the worse the positioning algorithms performed in general. The multipath and shadowing component that originates from the body presence is intensified with the inverse of the distance between the body and the receiving antenna, reducing the accuracy achieved by the positioning algorithms tested.

The PLE estimation method used in the CLP algorithm explores the fact that the anchor nodes are configured with their own location. This enables the use of inter-anchor node RSS and distance information in the PLE estimation. The CLP algorithm achieved its highest positioning accuracy of 2.69 m in the off-body-20 dataset, an improvement of 11% compared to WCL. The additional RSS information transmitted in the beacon messages sent by anchor nodes used in the CLP algorithm increased the overhead significantly. However, the algorithm performance has not improved with this added information for the case of the on-body dataset, which is the use-case of interest for a personal positioning system. Given the result obtained for the off-body-20 dataset for the CLP, this PLE estimation method could also outperform the raw RSS used in WCL if the human body was not present in the scenario. These results show that there is a weak correlation between RSS and distance in our indoor environment, where RSS more closely resembles a proximity inference metric than a distance inference metric. These results are also specific to the IEEE 802.15.4 physical layer in the 2.4 GHz frequency band, which is the protocol implemented by the CC2530 hardware modules used in this work.

Using more anchor nodes is a solution to improve localization accuracy; yet, to increase anchor number in the test scenario, precautions would be necessary for the following reasons: extra anchors inside the positioning area would not be possible to add since they would need to be at the same height as other anchors, and, as such, would pose an obstacle to the user inside the positioning area; increasing the number of anchor nodes would increase complexity and the overhead in CLP would grow exponentially.

The distance between anchor nodes and walls is another important parameter to consider when deploying RSS positioning systems. Using a minimum distance of 2 meters from walls, the RSS collected by the sensor node in the positioning setup is approximately the same as the RSS collected in the anechoic chamber. The anchors in our positioning scenario had much lower distances from walls, with 0.36 m in the worst case, and 1.8 m in the best

case. These smaller distances affect especially anchors 2 and 3, for which the RSS distributions from Figure 5.13 differed significantly from other anchors. Further testing would be necessary to find an optimum wall distance that maximizes the efficient use of an indoor space with minimal impact in algorithm performance. The height of the anchor and sensor node with respect to the ground is also an important parameter, which was made constant in this work. The height influences the ground reflected wave, which can add constructively or destructively to the direct path wave, greatly influencing the RSS.

5.8 References

[1] P. Macedo, J. Afonso, L. Rocha, and R. Simões, 'A telerehabilitation system based on wireless motion capture sensors', in *International Conference on Physiological Computing Systems, PhyCS 2014*, 2014, pp. 55–62.

[2] InvenSense, 'MPU-6000 and MPU-6050 Product Specification', 2013.

[3] Honeywell, '3-Axis Digital Compass IC HMC5883L', 2010.

[4] E. Damosso and L. M. Correia, 'Cost Action 231: Digital Mobile Radio Towards Future Generation Systems, Final Report.', 1999.

[5] F. Della Rosa, L. Xu, J. Nurmi, C. Laoudias, M. Pelosi, and A. Terrezza, 'Hand-grip and body-loss impact on RSS measurements for localization of mass market devices', *2011 International Conference on Localization and GNSS (ICL-GNSS)*, pp. 58–63, 2011.

Chapter 6

Stride and Heading System for WSN in Indoor Environment

The inertial measurement unit (IMU) used in the previous chapter is, in itself, a standalone form of positioning system that can be applied in order to improve position estimates, as such, a stride and heading system (SHS) is implemented in this work.

The location where the IMU is placed in the body plays a very important role in terms of algorithm selection, leading to different performances between implementations. A solution often adopted in the literature is the placement of the IMU on the foot. This location enables simple detection algorithms based on thresholds, due to the high dynamics sensed during the human gait cycle. Detecting steps or strides is typically accomplished by applying a threshold to the signal of interest from the accelerometer or gyroscope sensors (magnetometer sensor is also possible, although presenting higher detection error) [1].

Applying a constant threshold presents a disadvantage: the threshold is chosen under specific conditions, which, when not present, incur in errors in the stride detection (SD) algorithm. A filter is usually applied in order to remove undesired momentary variations, along with additional restrictive conditions (e.g., by using a timer with a predefined interval to

avoid false detections between strides [2]) to further reduce detection errors. The threshold method is typically employed to accurately detect inactivity periods, in order to apply zero-velocity updates (ZVUs) to correct drift errors during these time instants [2]–[4]. This is considered the most versatile method due to the decomposition of the stride length in each axis of the world coordinate system, enabling the detection of motion in any direction, including height changes during a walk. An algorithm with less versatility than the latter, similar to the ZVU applied to the ankle, is presented in [5] which performs a stride-by-stride integration of the gyroscope and accelerometer signals, detecting forward movement and height changes.

ZVUs provide the initial conditions for the integration of accelerations related to the duration of a single stride (i.e., integration is reset every stride and gravity is corrected from the accelerations), achieving accuracies in the order of 0.3% to 3% of total travelled distance (TTD). Another strategy to infer SL is to apply a model or an empirical formula to the data collected by the IMU during one stride [6], [7], resulting in accuracies between 3% to 8% of TTD. The latter methods, although exhibiting lesser accuracy than the former methods that use ZVUs, have lower computational complexity and are therefore of interest to this work.

Following an approach similar to the works in [7]–[9] and having in consideration that the algorithms are to be applied to devices with low computational capabilities, we implement SD and stride length (SL) estimation by placing the IMU in the ankle of the user. The sensor module is attached in a fixed position and orientation on the user's ankle. The ankle is chosen for the position of the IMU since its angular velocity pattern allows a better segmentation of the gait cycle. Also, by placing the IMU in a specific orientation, a simplification in the SD algorithm is possible, by searching the data stream for events only in one axis of the gyroscope, which is the axis that senses the majority of the rotations observed in the sagittal plane (y-axis or pitch axis in this work). Since the typical stride movement is in its majority localized in this axis, initial IMU offsets or misalignments do not influence significantly the event detection. The stride length (SL) estimation, however, has a strong dependency on misalignments of the sensor node. These misalignments translate into angular velocities observed in all axes, which cannot be disregarded as in the case of SD. It is therefore necessary to account for angular velocity observed by the sensor in these axes, in order to reduce errors in SL estimation.

6.1 Stride Detection

The goal in this work is to robustly detect strides by placing the node in a specific position and orientation, so the body axes of the gyroscope are (at least) coarsely aligned with the global vertical and forward axes. The misalignment of the node can be seen as a common issue when placing the IMU in the ankle, therefore robustness against misalignment conditions is desirable in a real use-case scenario. When placing the sensor node in the user's ankle, the *x*-axis (forward direction axis) of the IMU is aligned with the direction of movement. The rotations in the sagittal plane are sensed mainly by the *y*-axis of the gyroscope, which is used in the algorithm to detect the phases of the gait cycle. The *y*-axis in this work is filtered using a second order Butterworth low pass filter with a cut-off frequency of 4 Hz (such as in [5]). A plot of the *y*-axis of the gyroscope measurements during one stride is presented in Figure 6.1.

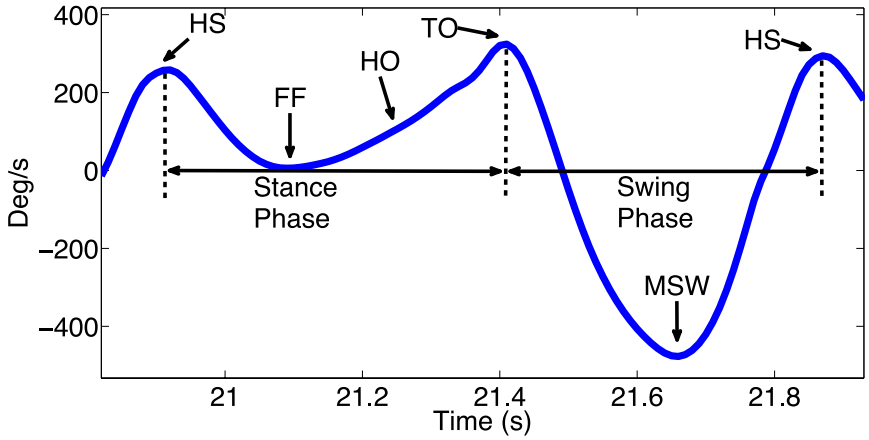

Figure 6.1: Filtered gyroscope measurements for steady walking, collected from an IMU placed in the ankle.

During steady walking, all the states from both phases of the gait cycle are clearly identified during a stride. Some states can be missing from the data stream under specific conditions, such as walking in uneven terrain, climbing stairs, walking uphill or downhill. Another cause for missing states from the gait cycle is related to health or disability issues of the user. For a normal person, when the stride ends in the MSW (mid-swing), the heel-strike (HS) state is typically missing in the measurements, depending on how abruptly the foot stops the stride. These issues are generally known to influence pedestrian navigation, yet some of these issues are highly uncommon, such as uneven terrain in indoor environment. Taking into consideration the issues described, a SD algorithm was developed and is presented in Figure 6.2.

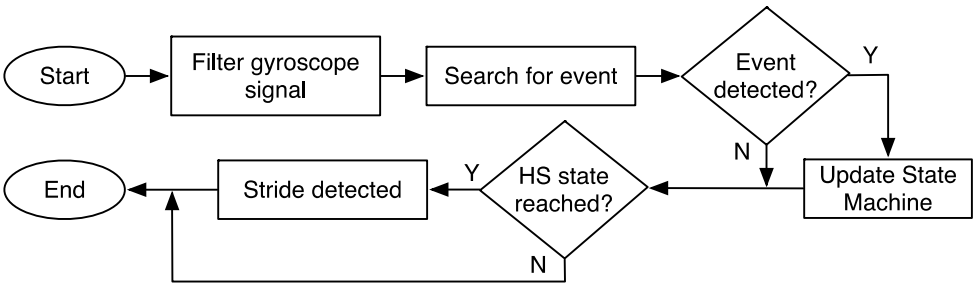

Figure 6.2: Proposed SD algorithm.

At every new measurement collected from the IMU, the main gyroscope axis is filtered and used in the search for events by comparing the current and the previous filtered sample, with knowledge of the previous state of the gyroscope signal (e.g., rising or falling). A set of events is identifiable:

- An upper peak (UP), when the gyroscope signal changes the slope from positive to negative.
- A zero crossing (ZC), when the gyroscope signal changes sign.
- A lower peak (LP) when the gyroscope signal changes the slope from negative to positive.
- A combination of both UP and ZC (UPZC), and LP and ZC (LPZC), which can happen if the update rate of the gyroscope is not fast enough to detect a peak before a ZC occurs.

Whenever an event is detected, it is used to update the finite state machine (FSM) depicted in Figure 6.3.

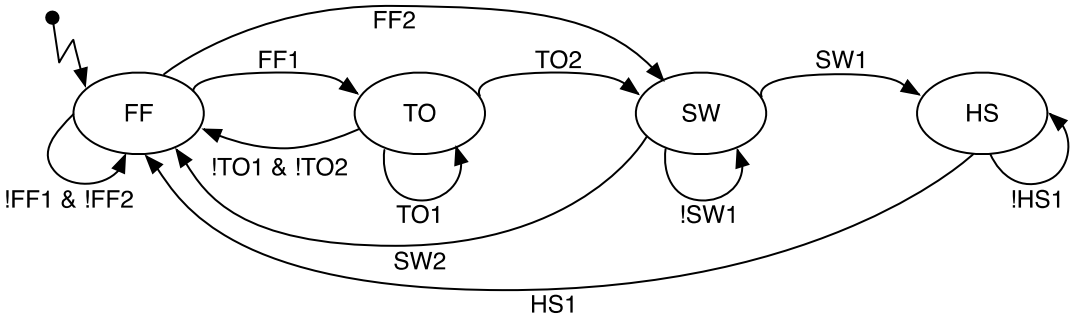

Figure 6.3: Finite state machine applied in stride detection using gyroscope measurements.

The symbols "!" and "&" in the transitions between states in the FSM represent NOT and AND logical operations, respectively. The conditions for each state transition are described as follows:

- FF1: the event is UP and the previous filtered value is higher than the threshold.
- FF2: the event is UPZC and the previous filtered value is higher than the threshold.
- TO1: the event is UP.
- TO2: the event is ZC.
- SW1: the event is ZC or LPZC and the stride is valid.
- SW2: the event is ZC and the stride is invalid.
- HS1: the event is UP or UPZC.

The FSM starts in the foot-flat (FF) state, where it searches for the UP event. When this event is detected and the previous filtered sample is higher than the predefined threshold, the transition to the toe-off (TO) state occurs. By using a threshold, part of the false positive UP events that would trigger a transition to the TO state are discarded. The FSM can also transit to the swing phase directly if the UPZC occurs (e.g., due to a slow update rate or faster stride speed).

Occasionally, in the TO state, multiple UP events can occur either due to walking in irregular pavements or due to slow walking. As such, the FSM stays in the TO state if the UP event is found. The transition from TO state to the swing (SW) state occurs when the ZC is detected; if the event detected is not a ZC, the FSM goes to the initial state to start searching for the UP event again.

After entering the SW state, the FSM searches for a ZC event, which typically appears immediately before the HS. When this event is found, a stride is evaluated. A stride is considered valid only when the maximum absolute value of the current filtered sample during the SW state was higher than the threshold.

The SD algorithm is controlled by the threshold parameter (used in TO detection and stride validation). This threshold applied is less rigid than the typical thresholds applied in other methods, since the decision of SD does not solely depend on this minimum threshold value.

6.2 Stride Length Estimation

Two methods are used to implemented SL estimation in this work: a simple method with lower computation complexity, which integrates the angular velocity from the gyroscope during the time interval when the user swings the leg forward; and an improved method with higher computation complexity based on the algorithm applied in [5], where the integration of the ankle acceleration is performed for the duration of the gait cycle.

For the simple method, a pendulum is used as an approximation model to the SL estimation, as presented in Figure 6.4.

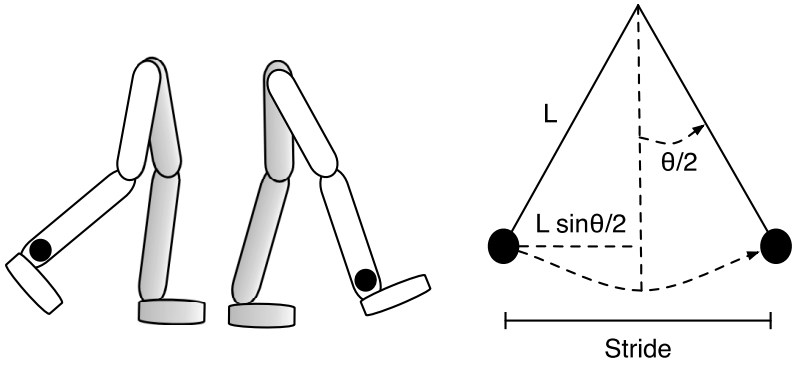

Figure 6.4: Pendulum model approximation for stride length estimation.

This model depends on the user's leg length, for which the method applied in [10] was used to find this parameter, by measuring the distance between the medial malleolus and the anterior superior iliac spine. Under the assumption that the angle described by the ankle after the TO until the HS phase is proportional to the stride, the SL is given by:

$$SL_1 = 2 \cdot L \cdot \sin\frac{\theta}{2} \tag{6.1}$$

where L is the leg length in meters and θ is the angle in radians, obtained by the gyroscope integration of the movement observed by the IMU in the sagittal plane. In order to avoid trigonometric calculations in the sensor node, equation (6.2) can be applied instead of equation (6.1).

$$SL_2 = L \cdot \theta \tag{6.2}$$

Equation (6.2) computes the length of the arc described by the ankle motion, which is used as an approximation of the actual SL.

The state information from the SD algorithm is used in order to accomplish the integration of the forward swing of the leg. Due to the filtering step applied to the main gyroscope axis, the true start of the SW state of the SD algorithm is delayed, compared to the raw gyroscope data. Performing the gyroscope integration when the FSM enters the SW state would depend on the delay introduced by the filter. Instead, the integration is performed when the FSM is either in the TO or SW states and only when the angular velocity of the raw gyroscope main axis is negative. Only the main gyroscope axis is filtered and used as input to the FSM. The integration is performed using the raw gyroscope measurements from all axes, therefore reducing computation complexity by not carrying out the filtering of all axes. The integration is reset every time the FSM enters the TO state, preventing the integration of angles that do not belong to the current stride.

When the user performs a turn while walking, a bias can also incur in the SL estimation, since the integration is accounting for other movements besides the pendulum motion of the stride. Turning while walking does not often occur, since people tend to walk in straight paths. This bias in SL is generally small and can be disregarded due to its low frequency during walking.

For the improved method, the algorithm from [5] is applied, using the state information derived in the SD algorithm to find the ankle vertical event. When this event is detected, the ankle is considered vertical, and as such, the angle of the IMU with the vertical axis is zero. This provides the initial condition for the integration of the gyroscope data using equation (6.3), starting from the quaternion identity (i.e., quaternion vector [1, **0**]):

$$ {}^{b}_{w}\boldsymbol{q_i} = {}^{b}_{w}\boldsymbol{q_{i-1}} + \frac{1}{2}\,{}^{b}_{w}\boldsymbol{q_{i-1}} \otimes \boldsymbol{\omega} \cdot \Delta t \tag{6.3} $$

where $ {}^{b}_{w}\boldsymbol{q_{i-1}} $ is the previous iteration of the gyroscope based quaternion rotation from body frame (b) to world frame (w), $\otimes$ denotes the quaternion multiplication, $\boldsymbol{\omega}$ is a quaternion with zero scalar part and vector part equal to the filtered angular velocity sample from the gyroscope (in rad/s) and Δt is the sampling period. The acceleration in world frame is computed using equation (6.4):

$$ {}^{w}\boldsymbol{a} = {}^{b}_{w}\boldsymbol{q_i} \otimes {}^{b}\boldsymbol{a} \otimes {}^{b}_{w}\boldsymbol{q_i}^{*} \tag{6.4} $$

where $ {}^{b}\boldsymbol{a} $ is the filtered acceleration sample in the body frame and $ {}^{b}_{w}\boldsymbol{q_i}^{*} $ is the quaternion conjugate of the current orientation estimate. The acceleration in world frame is given by the vector part of quaternion $ {}^{w}\boldsymbol{a} $. The effect of gravity is present in this acceleration, and in [5] it

is removed by simply subtracting gravity (9.81 m/s^2) from the vertical axis (*z*-axis). Since the zero-angle in the ankle vertical event is an approximation, it is not guaranteed that the gravity vector is precisely vertical with respect to the body frame. This vertical gravity assumption therefore depends on: misalignments (such as in the previous SL method) during the placement of the IMU; the anatomy of the user's leg, which might not allow a perfectly vertical position for the IMU (also depending on the IMU's size); and the user's posture during the ankle vertical event when walking. Instead of using the assumed vertical axis from the world frame, the filtered body frame acceleration sampled during the vertical ankle event is used as an approximation to the gravity vector, in order to estimate a possible tilt angle, which would otherwise influence the removal of gravity during the full integration of the stride cycle.

The ankle vertical event is detected in this work whenever the FSM is in the FF state and a LP or a LPZC event is detected. When a HS state is detected by the FSM, a flag is used to mark that a SD occurred. When the ankle vertical event is detected and this flag is active, the SL is evaluated prior to the reset of the integrated velocity and displacement of the ankle.

6.3 Orientation Estimation

The algorithm for orientation estimation in low computational capacity devices is typically the bottleneck of the system. The maximum update frequency will depend on how fast orientation can be estimated, since this is usually the most computationally intensive operation performed. In addition, high update frequencies are recommended in order to fully capture the user's movement. For this reason, complexity is a crucial aspect that needs to be taken into account when selecting the orientation algorithm. Since the envisioned use case is pedestrian navigation in indoor environment, which is typically affected by magnetic disturbances, coping with these disturbances is also a requirement. The low complexity requirement and the application of the IMU to the human body exclude the Kalman filter (KF) option, since not only this type of filter requires higher computational capacity as compared to the complementary filter (CF), but it has also been shown to provide lower accuracy than the CF, due to the increased complexity of the process model and absence of the control input [11]. The CF solution is therefore adopted in this work.

Two types of orientation estimates can be derived from the sensors contained in the IMU: through gyroscope integration and through vector observations (from the accelerometer

and magnetometer sensors), which give an estimate of the direction of gravity and the direction of the magnetic north respectively. For the two-vector observation (TVO) method, several well-known algorithms exist, among which are the triad [12] and the factored quaternion algorithm (FQA) [13]. These solutions produce an orientation estimate with a single sample of the vector observations and decouple the magnetometer influence in the roll and pitch angles, affecting only the yaw (or azimuth) angle. This feature is of interest, especially in environments with magnetic disturbances.

Several CFs are available in the literature [14]–[16] that fuse information from both types of orientation estimates. We analysed these filters in terms of robustness against external influences (accelerations and magnetic interferences), and with the notable exception of [16], orientation accuracy was rapidly and severely affected. To improve robustness against external influences, we propose a generic algorithm that can be applied to a CF structure using any TVO algorithm in combination with gyroscope integration.

Several sources of error affect the orientation algorithms used in an attitude and heading reference system (AHRS): external influences (acceleration or magnetic disturbances), sensor calibration errors and white noise that causes drift when integrated. By combining two complementary sources of orientation information, the CF removes the drift that would be observed if using only the gyroscope integration method and attenuates influences from external acceleration and magnetic disturbances that would be observed if using only the TVO method.

The CF is governed by a single parameter that is the cut-off frequency, which can be seen as a weighting factor between both orientation estimates. When under external influences, the TVO method becomes unreliable. This in turn influences the final orientation estimate of the CF. External accelerations due to impacts or repetitive motions and magnetic disturbances that occur when near metallic objects deteriorate the orientation estimate. As an illustration of these signals in pedestrian navigation, the module of accelerometer and magnetometer data collected while walking with an IMU attached to the ankle is presented in Figure 6.5.

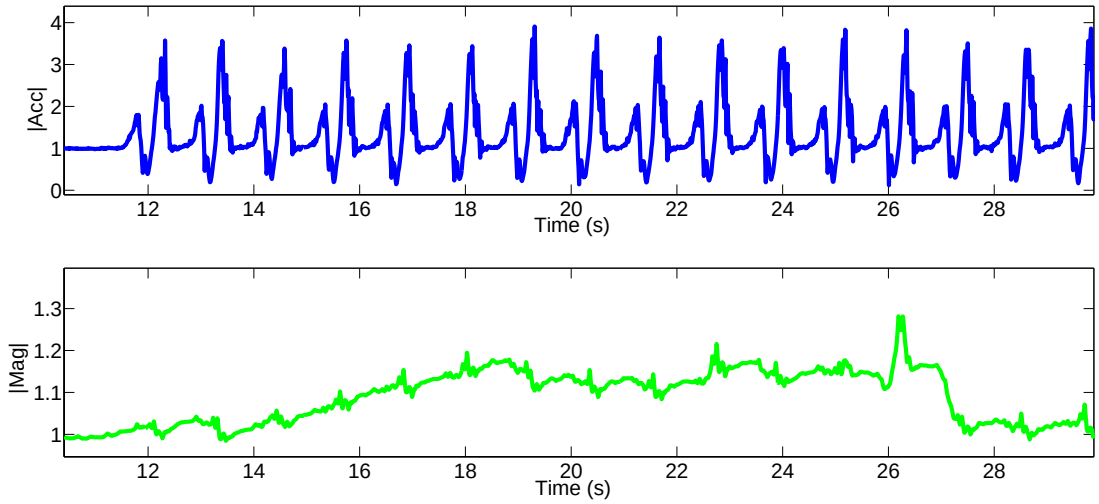

Figure 6.5: Normalized accelerometer (top) and magnetometer (bottom) data collected from a walk with an IMU attached to the ankle.

External accelerations in human walking are typically high frequency variations, lasting less than a second. Magnetic disturbances do not share this property. They are constant and environment dependent when the user is not moving. When the user is moving, the magnetic vector norm undergoes changes. The closer the IMU is to metallic objects, the greater the influence in the magnetic disturbance.

It is clear that both high and low frequency variations occur when walking in an indoor environment. Furthermore, the magnetometer calibration is valid for the specific location where it took place, as can be seen by the unitary module of the magnetic vector at the beginning of the walk.

The orientation estimation is accomplished by applying the CF presented in the block diagram of Figure 6.6.

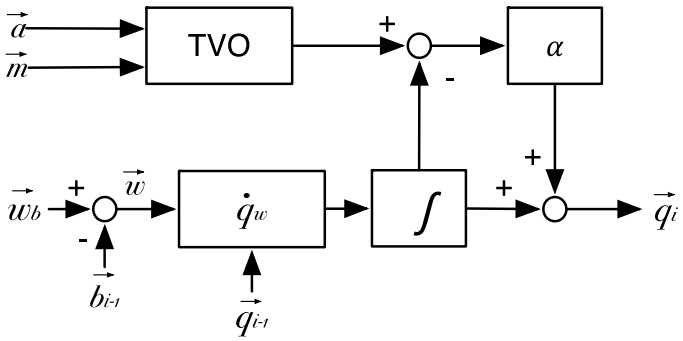

Figure 6.6: Block diagram of the orientation estimation using a CF.

Two orientation estimates are obtained by employing a TVO method (such as [13], [17]) and the gyroscope integration. These estimates are then applied to the CF, which is governed by the parameter α, which depends on the desired time constant τ and the sampling period Δt:

$$\alpha = \frac{\Delta t}{\tau + \Delta t} \tag{6.5}$$

The bias $\boldsymbol{b_{i-1}}$ from the gyroscope is first removed from the gyroscope sample and the gyroscope orientation estimate is obtained by integrating the bias-free angular velocity using equation (6.3).

The error is computed by finding the element-by-element difference between the TVO and the gyroscope orientation quaternions:

$$\boldsymbol{{}^{b}_{w}q_{e} = {}^{b}_{w}q_{tvo} - {}^{b}_{w}q_{g}} \tag{6.6}$$

The final orientation estimate is the element-by-element sum of the gyroscope orientation quaternion and the error quaternion with each of its components multiplied by the α parameter:

$$\boldsymbol{{}^{b}_{w}q_{i} = {}^{b}_{w}q_{g} + {}^{b}_{w}q_{e} \cdot \alpha} \tag{6.7}$$

Quaternion normalization is necessary at this stage in order to avoid accumulation of rounding errors.

One issue arises when applying CF to fuse orientation estimates in quaternion space. A quaternion q and its symmetric $-q$ represent the same rotation, e.g., rotating about an axis e by an angle θ and rotating about an axis $-e$ by an angle $-\theta$ are identical rotations. If the TVO method derives a quaternion that is symmetric to the gyroscope integration method, the error estimate of the CF will no longer estimate orientation errors. This in turn forces the current orientation q to converge to $-q$, by performing a 360-degree turn about an arbitrary axis, until both orientation estimates are numerically equal. The algorithms in [14], [16] avoid this by applying the CF to the estimation of the gravity and north magnetic vectors. This condition is avoided in this work by simply negating the components of the TVO quaternion when its dot product with the gyroscope quaternion is negative.

Increased robustness against external influences is an important property of indoor positioning systems. Increasing the order of the filter is a natural option, so a stronger attenuation of these unwanted signals would take place. Instead, a more flexible option is

considered, by applying the operations depicted in the block diagram of Figure 6.7 to the resulting orientation from the CF.

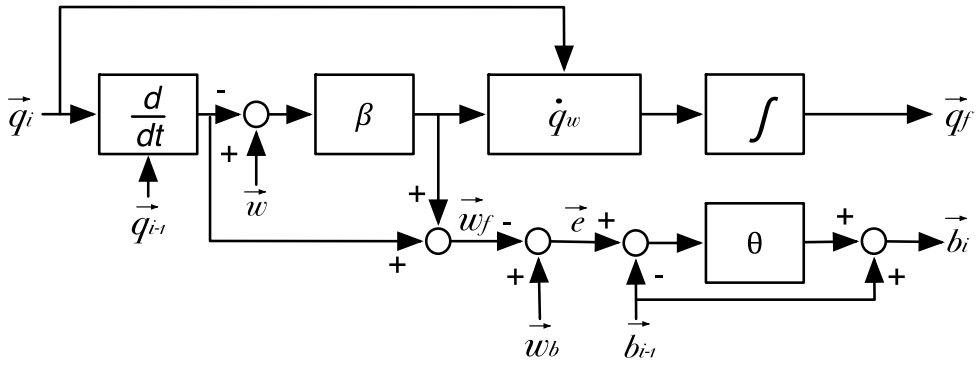

Figure 6.7: Block diagram of the external influence compensation and bias estimation.

The estimate of the angular velocity observed by the CF is first computed by finding the angular velocity observed between successive iterations, using equation (6.8).

$$ {}^{b}\dot{\boldsymbol{q}}_{\boldsymbol{\omega}} = \frac{2}{dt}\left({}^{\boldsymbol{b}}_{\boldsymbol{w}}\boldsymbol{q}^{*}_{i-1} \otimes {}^{\boldsymbol{b}}_{\boldsymbol{w}}\boldsymbol{q}_{\boldsymbol{i}}\right) \tag{6.8} $$

Since the angle difference between iterations is small, the vector part of the result of equation (6.8) will be equivalent to the angular velocity (due to the small angle approximation of the *sin* function). The difference between this angular velocity and the gyroscope sample is the correction factor that the TVO algorithm is imposing on the CF. By simply multiplying this difference with a constant β lesser or equal to one, a percentage of the correction factor is removed.

Since the TVO algorithm uses the accelerometer to estimate the tilt angle and the magnetometer to estimate the yaw angle, the β constant becomes a two-element vector, where the first element influences the *x* and *y* components of the angular velocity correction (roll and pitch angles) and the second element influences the *z* component (yaw angle). The main goal behind the external influence compensation method is to provide a simple parameterization of the confidence that should be assigned to the corrections of the accelerometer and magnetometer readings, under the condition that the gyroscope bias is known, either by offline calibration or online bias estimation.

Gyroscope bias estimation is an important part of the AHRS due to its time varying nature. It is typically addressed in KFs, yet seldom addressed in CF implementations, apart from notable exceptions such as [18]. A simple way to find the bias of a gyroscope is to

average the samples of a static sensor node over a small period of time, since the true angular velocity is known (zero). Using only the TVO method to infer angular velocity is not possible due to the magnitude of the error in the orientation estimate. For example, an orientation estimate with an error of 0.22 degrees at 100 Hz update rate (which is the case of the TVO method for the IMU used in this work, demonstrated in the next section) would exhibit high angular velocity error (22 º/s minimum) even when the node is actually static. The angular velocity from the CF is computed using equation (6.8). The gyroscope bias is estimated by low pass filtering the difference between the CF's angular velocity and the angular velocity observed by the gyroscope, and using this averaged bias estimate in the next iteration to correct the gyroscope sample. The same cut-off frequency of the CF is used in low pass filtering of the bias estimation, in order to achieve a stable bias estimate. Since the operation depicted in Figure 6.7 is selectively increasing the time constant of the CF for the roll, pitch and yaw angles, any modification in the time constant must also be reflected in the coefficients of the low pass filter of the bias estimation, i.e., equation (6.5). The coefficient for the bias estimation is obtained using equation (6.9), applied using each component of the β parameter:

$$\theta = \frac{\Delta t}{\frac{\tau}{\beta} + \Delta t} \tag{6.9}$$

For β equal to zero, the bias in the lower branch of Figure 6.7 does not change, thus no bias estimation is possible, since in this case only the gyroscope is effectively being used in the orientation estimation. It is important to highlight that, since the TVO method is not reliable under external influences, bias estimation should only occur when the IMU is stationary or when no external influences are detected.

6.4 Sensor Characterization

The Allan variance (AVAR) test was applied to the IMU used in this work in order to quantify the noise levels affecting the inertial navigation. Measurements from the three sensors contained in the IMU were collected at a frequency of 100 Hz for a period of 12 hours, where the sensor node was kept stationary. The AVAR for an averaging time *t* is computed by splitting a long sequence of data into *M* bins of length *t* (e.g., bins with *t* seconds of data). The average value y_i is then calculated for each bin *i*. The AVAR is obtained using equation (6.10).

$$AVAR(t) = \frac{1}{2(M-1)} \sum_{i=1}^{M-1} (y_{i+1} - y_i)^2 \tag{6.10}$$

The bin number and bin size varies according to the averaging time, with the smaller bin size given by twice the sampling time. A larger bin size implies higher error in the results due to the smaller number of bins *M* used in equation (6.10).

The Allan deviation is the square root of the AVAR. The parameters of interest are simply read directly from the plot in logarithmic scale. These parameters are related to the slopes and minimum values, which are caused by different random processes. Quantization noise typically appears at the start of the averaging time, with a slope of -1. White noise is identified in the plot as the region with a slope of -0.5. The random walk is measured by fitting a straight line through the slope and reading its value at t = 1 s. Bias instability is given by the minimum value, which is found in the flat region of the plot. The results for the accelerometer, gyroscope and magnetometer sensors are presented in

Figure 6.8,

Figure 6.9 and Figure 6.10, respectively. A summary of the values of interest is presented in Table 6.1

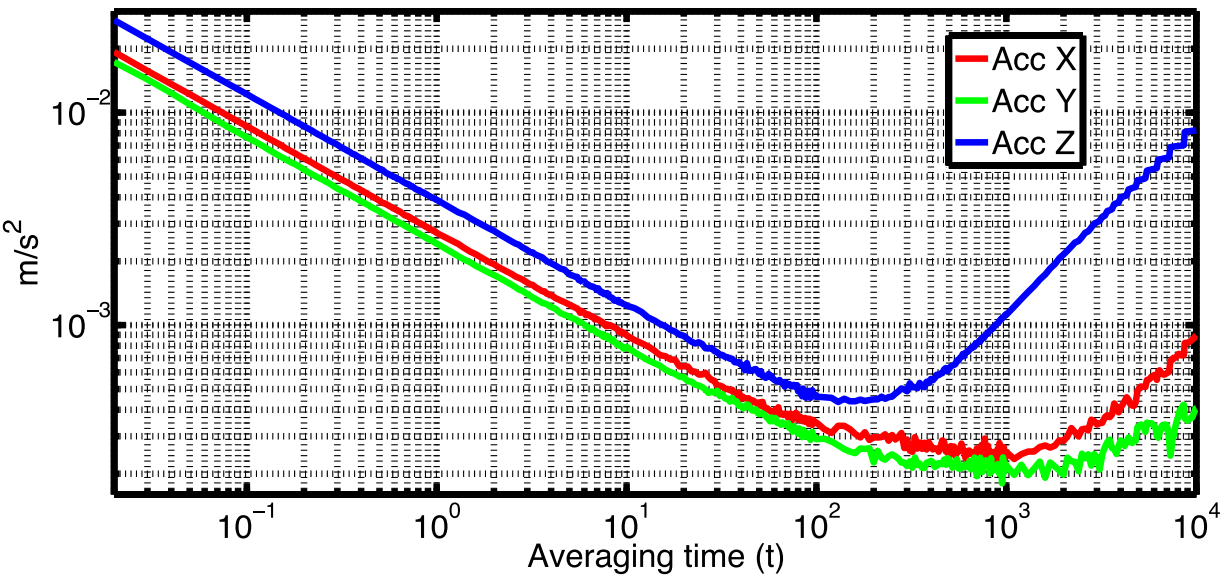

Figure 6.8: Allan deviation for the accelerometer sensor.

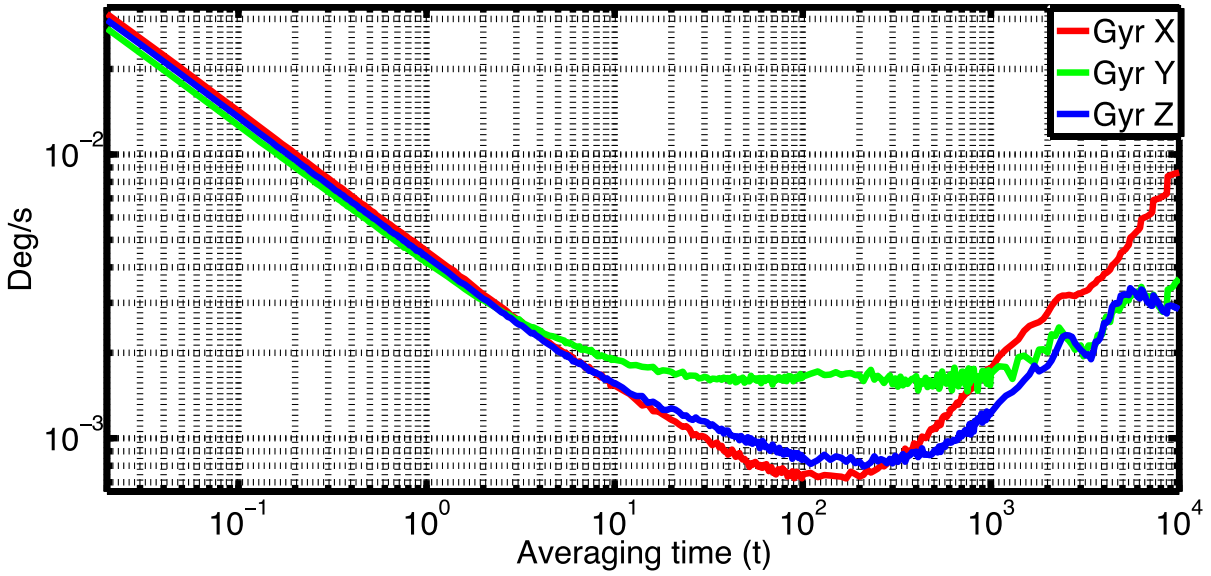

Figure 6.9: Allan deviation for the gyroscope sensor.

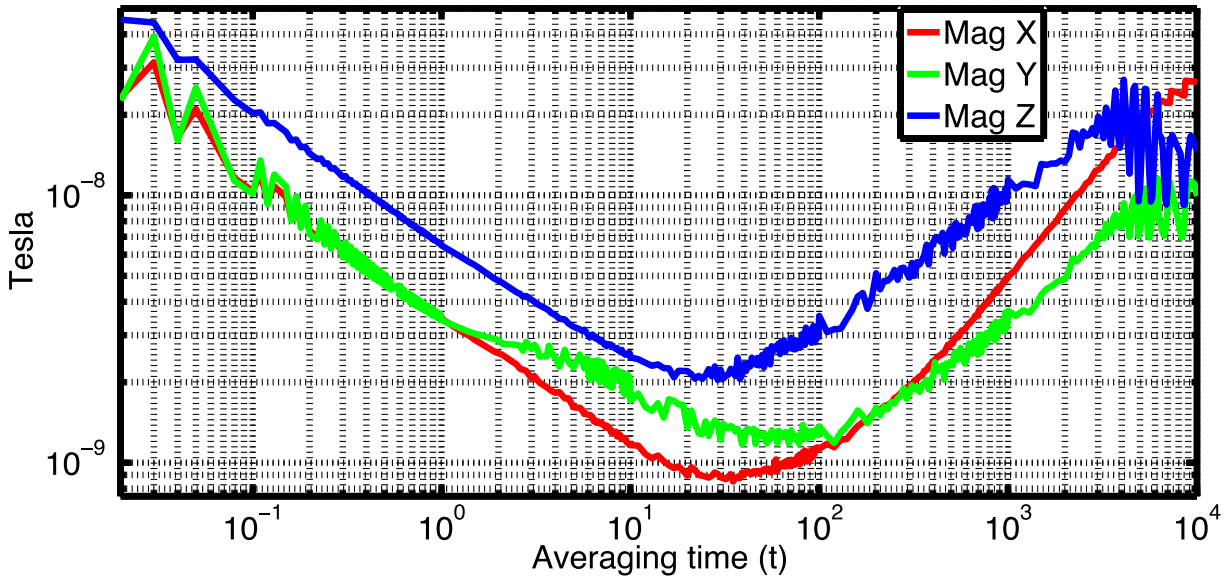

Figure 6.10: Allan deviation for the magnetometer sensor.

The absence of a slope of -1 in every axis shows that quantization noise is negligible for all sensors at the sampling frequency used. For the magnetometer sensor, some interference is visible in the low frequency range, which is normal, since the data collection was not performed in a controlled environment; as such, it was susceptible to external magnetic interferences.

Table 6.1: Summary of Allan deviation values for bias instability and random walk.

Sensor	Axis	Bias Instability	Random Walk
Accelerometer MPU6000	X	0.224×10^{-3} m/s^2 (950 s)	2.714×10^{-3} m/s^2
	Y	0.180×10^{-3} m/s^2 (950 s)	2.425×10^{-3} m/s^2
	Z	0.435×10^{-3} m/s^2 (130 s)	3.891×10^{-3} m/s^2
Gyroscope MPU6000	X	0.722×10^{-3} º/s (170 s)	4.559×10^{-3} º/s
	Y	1.46×10^{-3} º/s (750 s)	4.165×10^{-3} º/s
	Z	0.795×10^{-3} º/s (210 s)	4.386×10^{-3} º/s
Magnetometer HMC5883L	X	0.851×10^{-9} T (35 s)	3.455×10^{-9} T
	Y	1.172×10^{-9} T (39 s)	3.413×10^{-9} T
	Z	2.04×10^{-9} T (29 s)	6.496×10^{-9} T

The angle random walk (ARW) is calculated by applying equation (6.11) to the random walk noise obtained for each axis of the gyroscope.

$$ARW\left[°/\sqrt{h}\right] = 60 \times ND\left[\frac{°/s}{\sqrt{Hz}}\right] \tag{6.11}$$

In the worst-case value (gyroscope's *x*-axis) from Table 6.1, a value of 0.274 º/√h is obtained, which is similar to the value of 0.3 º/√h calculated from the datasheet specifications.

Both the accelerometer and the magnetometer are used to obtain an absolute estimate of the orientation. The random walk noise imposes the limit on the accuracy that can be achieved. Taking the random walk value for the worst-case accelerometer axis *z*, dividing by the value of gravity due to the normalization of the accelerometer reading in the TVO algorithms, and converting the result to degrees, an error of approximately 0.022 degrees is obtained. However, this error is achieved when only the acceleration from gravity is sensed by the accelerometer, and when the accelerometer samples are averaged over a 1 second interval. Since each measurement is being used to compute the angle estimate at 100 Hz, the error is 0.22 degrees (one decade above due to the slope of -0.5 in the AVAR plot).

Following a similar analysis for the magnetometer case, a value between 25 to 65 micro-Tesla is expected in the absence of magnetic disturbances, which imposes a worst-case error angle of approximately 0.15 degrees.

This analysis does not consider the calibration influence and can be seen as a best-case scenario under perfect calibration values. Under normal conditions, the angle is affected by

sensor bias, scale factor, axis misalignments, temperature and non-linearity in the sensor outputs.

6.5 Experimental Setup

An evaluation of the SHS was performed to each of its components: the SD/SL and the AHRS. For both components, the evaluation was performed using data collected from an IMU attached to the ankle of the user, while performing a specific set of routes. The data collection experiments were conducted at University of Minho, Campus of Azurém.

Two subjects were asked to perform a specific set of routes within the experimental setup. Three routes were planned for the subjects to follow: a straight line path where the person walks from one point to the other and back, without making any turn while walking (green line); a path around the Hall, which includes turns (blue line); and a path that, besides including turns, also includes stairs and irregular pavements (red line). The footprint of the area is presented in Figure 6.11.

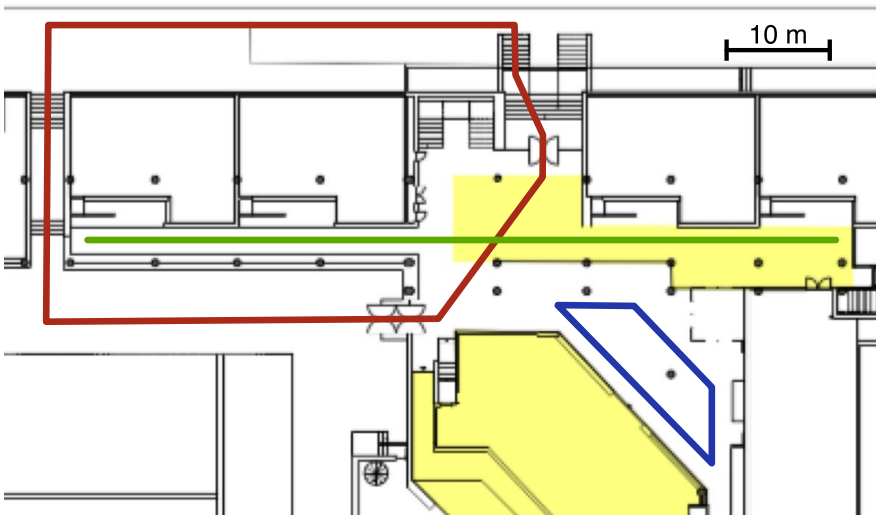

Figure 6.11: Footprint of the experimental setup with the routes performed by the subjects.

The goal of each route is to present different degrees of difficulty for the SD and SL algorithms, with features typical in indoor environment. A distance-measuring wheel was used to obtain the true length of each route, in order to infer the accuracy of the SL estimation algorithm. For the route with stairs, the length included the vertical and horizontal length of each stair. The subjects were asked to perform the routes two times, under normal and fast walking paces, in order to have different speeds to compare between the results. Since all routes start and finish in the same point, the orientation algorithm's resilience to indoor

conditions are observed by the deviation between start and finish points in the end of each route.

The hardware platform from the previous chapter is also used in this work. The sensor node collects measurements from the IMU at a frequency of 100 Hz. This update rate is necessary for the gyroscope to be able to measure the dynamics of the foot during the gait cycle. The gyroscope, accelerometer and magnetometer dynamic ranges were set to 1000 º/s, 4 g and 0.88 gauss respectively. These ranges guaranteed that no sensor output saturation occurred during the experiments and the signals of interest remained well within range in order to avoid non-linear behaviours.

Manual calibration was performed on site for each of the IMU's sensors. For the accelerometer and magnetometer, minimum and maximum values were found by manually aligning the sensing axis with the direction of gravity or local magnetic field. For the gyroscope, bias values were found by simply averaging the gyroscope outputs while the sensor is static. A manual calibration for the scale factor of the gyroscope was also carried out by performing multiple 360-degree rotations in each axis while manually adjusting the scale factor, in order to obtain 0-degree angle when the sensor returns to the original orientation. Temperature calibration was not performed. To reduce the temperature effect, the sensor was powered on for several minutes prior to the data collection, so a working temperature could be achieved. With the exception of the red route from Figure 6.11, where a portion of the route is performed in outdoor environment, all other routes were performed indoor, for which temperature variation is small.

6.6 Results

6.6.1 Stride Detection

The SD algorithms from [1], [19] were also implemented and evaluated for the same datasets collected, in order to have a basis for comparison. Although [1], [19] are applied to the foot, the algorithms can also be used when the IMU is placed in the ankle. All algorithms apply a low pass filter to the signals of interest before processing. The authors in [19] do not clearly state what type of filter is used, as such we applied a median filter, such as performed in [1].

The user performs each route and counts the total number of strides taken from start to finish, in order to estimate the SD error. The algorithm described in section 6.1 is applied with the threshold parameter configured to 50 º/s, a value that was found empirically during the algorithm trials. The threshold effectively constrains how small or slow is the stride that the algorithm can detect. A value of 50 º/s is well below the normal angular velocity during slow walking.

A sample of the state of the SD algorithm during a stride is presented in Figure 6.12, where the states implemented in the SD algorithm are overlapped with the filtered *y*-axis gyroscope signal.

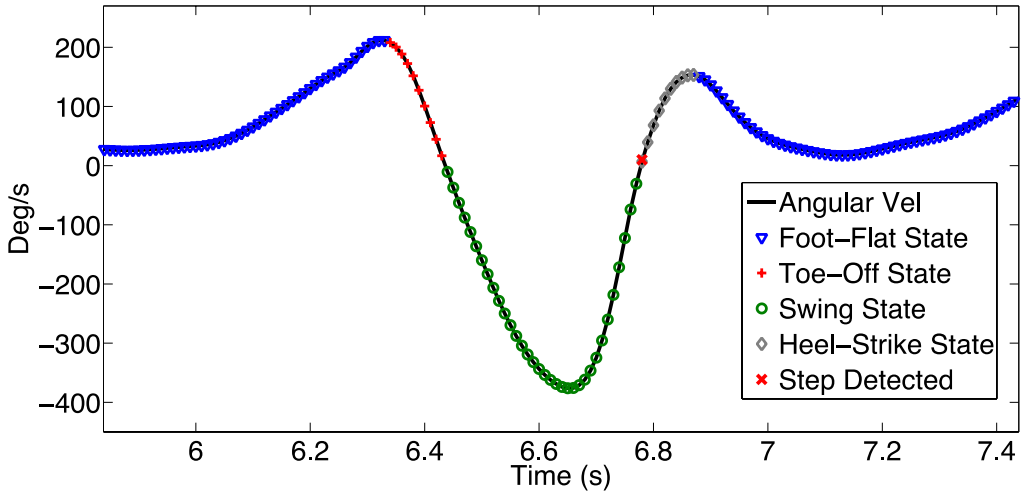

Figure 6.12: State identification of the SD algorithm during the gait cycle.

The states implemented by the SD algorithm are clearly identified. The TO state is detected when the UP event is observed for a value of angular velocity above the threshold. This is followed by a rapid decrease in angular velocity, which happens during the forward leg swing. During the leg swing, the FSM searches for a ZC event. When this event is found, a stride is evaluated by verifying if the minimum value of the filtered gyroscope axis is greater in absolute value than the threshold. The verification of this condition triggers the transition to the HS state, which signals the SD event.

The results for the routes performed by subject A and B are presented in Table 6.2 and Table 6.3 respectively.

Table 6.2: SD count and error percentage results for subject A.

Route	True Count	SD Algorithm	Jimenez [1]	Feliz [19]
Blue Normal	33	33 (0%)	33 (0%)	37 (12.1%)
Blue Fast	29	29 (0%)	29 (0%)	33 (13.8%)
Green Normal	106	106 (0%)	107 (0.9%)	109 (2.8%)
Green Fast	84	84 (0%)	84 (0%)	86 (2.4%)
Red Normal	101	101 (0%)	102 (1%)	111 (9.9%)
Red Fast	94	94 (0%)	91 (3.2%)	95 (1.1%)
Σ |Error|	0	0 (0%)	5 (1.1%)	24 (5.4%)

Table 6.3: SD count and error percentage results for subject B.

Route	True Count	SD Algorithm	Jimenez [1]	Feliz [19]
Blue Normal	33	33 (0%)	33 (0%)	34 (3%)
Blue Fast	27	28 (3.7%)	30 (11.1%)	29 (7.4%)
Green Normal	105	105 (0%)	106 (0.9%)	112 (2.8%)
Green Fast	80	80 (0%)	81 (1.3%)	82 (2.5%)
Red Normal	98	98 (0%)	101 (3.1%)	109 (11.2%)
Red Fast	88	91 (3.4%)	77 (12.5%)	94 (6.8%)
Σ |Error|	0	4 (0.9%)	19 (4.4%)	29 (6.7%)

The stride detection algorithm is able to deal with different terrain conditions, without affecting the SD performance. All strides were correctly detected in the results of subject A for each of the routes performed. Subject A counted a total of 447 strides, in routes that included stairs, slopes and irregular terrain. By manually analysing the gyroscope data, all the strides are clearly identified and the count of 447 is also confirmed. The proposed SD algorithm was able to detect all strides correctly. The typical threshold based algorithms that were used in the comparison also presented good overall performances.

The SD algorithm for subject B showed errors in the number of strides counted for the fast paced trials. By analysing the data in these trials, it can be concluded that the difference in the count of 3 strides in the red route and 1 stride in the blue route are related to the time instants when the user performed turns or halts the walk. In both cases where error in SD was found, stride count from the subject was smaller than algorithm SD count. This indicates that

the true strides are correctly detected and some marginal signals during special events of the walk are falsely detected as strides.

6.6.2 Stride Length Estimation

Each of the routes depicted in Figure 6.11 were measured using a distance-measuring wheel, for which the green, red and blue route distances were 127.6, 136.1 and 42.05 meters, respectively. Lengths of 82 cm and 86 cm were measured for the legs of subject A and B, respectively, using a measuring tape, according to the method used in [10]. Since the ZVU method described in [1] cannot be applied with the IMU placed in the ankle, we compare the SL estimation of this work to the method described in [6] (which is compared in [1] to the ZVU method) and to the method described in [5], which also applied the IMU to the ankle. These methods also filter the IMU signals with a 4^{th} order and a 2^{nd} order Butterworth filters in the frequencies of 3 Hz and 4 Hz, respectively. The method in [6] uses a calibration parameter, which was empirically determined for each subject using the data collected for the green route under normal pace. This route was selected for this purpose since it does not have any turns while walking. Calibration values of 0.656 and 0.660 were found for subjects A and B respectively. This calibration value is used throughout all the routes performed by the subject. Equation (6.2) is used for the simple SL estimation method, since it provides the simplest calculation method.

For the method in [6] the SD algorithm used is the same as in [1], which was evaluated in the previous section. For the remaining methods, and since the method in [5] does not specify the algorithm used in the SD, the method for SD of this work was used. The results for subject A and B are summarized in Table 6.4 and Table 6.5 respectively.

Table 6.4: Route distance error in meters and percentage of TTD for subject A.

Route	Simple Method	Improved Method	Weinberg [6]	Li [5]
Blue Normal	0.22 (0.5%)	0.40 (1%)	-2.72 (-6.5%)	-1.51 (-3.6%)
Blue Fast	-2.48 (-5.9%)	0.53 (1.3%)	-7.16 (-17.0%)	-1.51 (-3.6%)
Green Normal	2.93 (2.3%)	-0.66 (-0.5%)	0.05 (0%)	-6.82 (-5.3%)
Green Fast	-11.11 (-8.7%)	1.11 (0.87%)	-26.47 (-20.7%)	-5.22 (-4.1%)
Red Normal	-9.01 (-6.6%)	-1.02 (-0.7%)	-14.04 (-10.3%)	-7.84 (-5.8%)
Red Fast	-15.32 (-11.3%)	-3.84 (-2.8%)	-25.99 (-19.1%)	-11.78 (-8.7%)
Σ |Error|	41.07 (6.7%)	7.56 (1.2%)	76.43 (12.5%)	34.68 (5.7%)

Part of the error from the total length of the route also depends on the number of strides detected, since there is no SL estimation if a stride is not detected. The simple method performed approximately at the same level of the other more complex algorithms in the normal pace trials. For the faster pace, this method consistently underestimated the SL. In the case of equation (6.1), the underestimation of the SL would be greater, which would result in higher percentage of error. The use of equation (6.2) compensates this underestimation effect and also unburdens the sensor node from trigonometric calculations.

Table 6.5: Route distance error in meters and percentage of TTD for subject B.

Route	Simple Method	Improved Method	Weinberg [6]	Li [5]
Blue Normal	-0.71 (-1.7%)	1.19 (2.8%)	-2.30 (-5.5%)	-4.72 (-11.2%)
Blue Fast	-3.27 (-7.8%)	1.24 (2.9%)	-4.19 (-10.0%)	-4.09 (-9.7%)
Green Normal	1.09 (0.9%)	2.79 (2.2%)	-0.07 (0.1%)	-16.44 (-12.9%)
Green Fast	-13.09 (10.3%)	7.27 (5.7%)	-21.55 (-16.9%)	-11.39 (-8.9%)
Red Normal	-10.77 (-7.9%)	5.42 (4.0%)	-11.16 (-8.2%)	-14.40 (-10.6%)
Red Fast	-17.97 (-13.2%)	4.72 (3.5%)	-36.53 (-26.8%)	-16.70 (-12.3%)
Σ |Error|	46.90 (7.7%)	22.63 (3.7%)	75.80 (12.4%)	67.74 (11.1%)

Subject B, although not very different than subject A in terms of leg length, exhibited a faster pace than subject A, both in the normal and fast pace trials. This faster pace can explain the lower accuracy results from subject B compared to subject A, due to the underestimation of the SL under these conditions. The overall error percentage from all routes performed is comparable to the results obtained from the method in [5], which uses an higher computation complexity algorithm.

It is clear that the method in [6] is highly dependent on the calibration procedure, specially when under different walking paces, where the error percentage greatly increased for the faster pace trials. Even though the SD errors in Table 6.2 for the method used for this SL estimation algorithm are low (1.1% and 4.4%), the errors in the SL estimation where the highest (12.5% and 12.4%). This indicates a lower correlation with SL when this method is used with an IMU in the ankle.

In the case of the method in [5], the main reason that can explain the overall lower performance compared to the improved method presented in this work is the misalignment of the IMU with regard to the assumptions made in the algorithm. These misalignments are

addressed in the improved method, which not only resolved the accelerations in three dimensions, but also estimated the initial tilt of the IMU during the ankle vertical event using the accelerometer sample at the event instant. The improved method achieved overall lower error percentage, exhibiting improvements up to a factor of four, compared to the method in [5], where a two dimensional approach was used.

6.6.3 Stride and Heading System

For the results of the orientation algorithm proposed in this work, the algorithms from Madgwick and Gallagher in [14], [16] were also implemented, in order to provide a basis for comparison. The algorithm in [14] depends on two parameters, k_1 and k_2, which are used in the algorithm to control the influence of the gravity and magnetic vectors in the orientation. The method in [16] depends on a single parameter β, which is related to the correction step of the GDA, used in the fusion of the gravity and magnetic vector information. The orientation algorithm from this work uses a parameter α, which is related to the time constant of the CF by equation (6.4), along with the two-element vector $\boldsymbol{\beta}$ depicted in Figure 6.7, used to control the effect of external influences in the gravity and magnetic vectors. The Triad algorithm described in [17] was used as the TVO algorithm due to its simplicity and low computational demand. Note that the work in [14] also uses this method, while applying a different fusion algorithm with the acceleration and magnetic vectors.

The parameters for each of the algorithms where empirically determined using the data from the green route. The parameters that produced the best overall result for each of the algorithms were constant throughout the remaining routes from Figure 6.11. For Madgwick AHRS [16], a β parameter of 0.001 was used, which filtered most of the magnetic interferences that heavily affect the orientation in indoor environment. For Gallagher AHRS, k_1 and k_2 were set to 0.05 and 0.03 respectively. For the AHRS in this work, the α parameter was set to 0.0099 (equivalent to a time constant of 1 second) and the $\boldsymbol{\beta}$ vector was set to [0.001, 0.001].

The improved SL estimation method from this work was used, since it provided the best overall results in the previous section. The AHRS algorithms are executed at every new sample from the IMU. When a stride is detected, the current orientation computed by the AHRS is used to find the heading direction of the user.

The map of the location is presented in the background of the reconstructed routes, for clarity. The trajectories were rotated and scaled accordingly and overlaid in the map. In order to reduce the influence of this process, the initial orientation is chosen according to the orientation of the first three strides, from which the true orientation is known. All routes start at location $x = 0$ and $y = 0$, and this location was moved to the approximate starting position on the map. The reconstructed trajectories of the data from the normal walking pace of subject A for the green, blue and red routes are presented in Figure 6.13, Figure 6.14 and Figure 6.15, respectively.

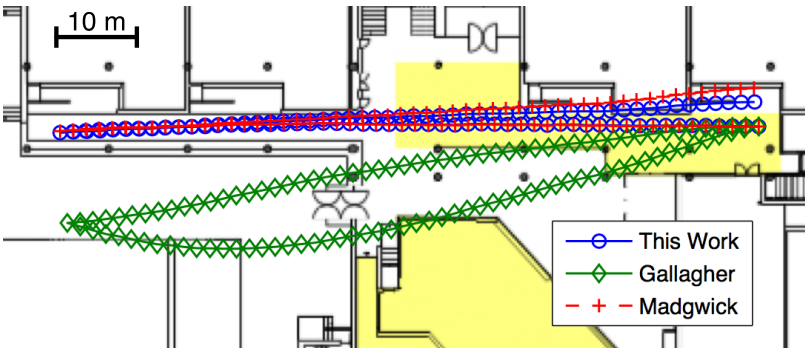

Figure 6.13: SHS results for the green route.

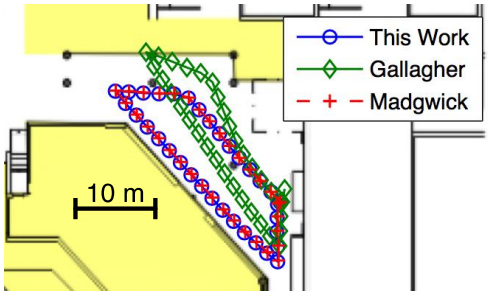

Figure 6.14: SHS results for the blue route.

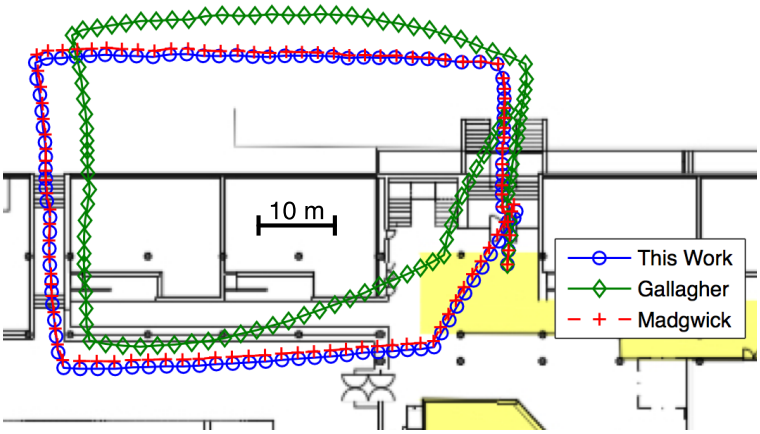

Figure 6.15: SHS result for the red route.

The parameters used in the AHRS algorithms for these experiments are very restrictive in terms of the amount of rotation that the accelerometer and magnetometer impose in the final orientation. The gyroscope contributes with most of the orientation changes, while the residual effect from the remaining sources is used mostly in eliminating the drift that would originate from solely using the gyroscope integration to infer orientation.

The resilience to magnetic interferences is clearly observed in the green route trial, where the main orientation is preserved for the entire length of the hallway. Notice that despite the deviation when returning to the starting point, the orientation itself is very close to the real orientation. This small deviation, when sustained for several successive strides, causes the trajectory to drift slowly. It can be seen that the performances of this work and [16] are very similar.

The results obtained for the red route reveal a greater discrepancy between the true route and the route obtained from the SHS. In this route, the user crosses a door (into outdoor environment) after the first three strides and climbs up two sets of stairs. At the top of the stairs a left turn is taken and a straight path with a small downhill slope is traversed on irregular pavement. A left turn is taken crossing the building, during which the user climbs down two sets of stairs. At the end of these stairs, another left turn is taken and the user enters the building and crosses the hallway to the starting point. Several sources contribute to this discrepancy, from higher magnetic variations in the transitions from indoor to outdoor, temperature variations, stairs and irregular pavement. All orientation algorithms tested performed worse in this route. The distance between the start and the finish point coordinates for each route is presented in Table 6.6.

Table 6.6: Distance in meters and error as a percentage of TTD between start and finish points.

Route	This Work	Madgwick	Gallagher
Green	2.24 (1.8%)	3.52 (2.8%)	1.31 (1%)
Blue	0.29 (0.7%)	0.20 (0.5%)	1.18 (2.8%)
Red	4.84 (3.6%)	5.42 (4%)	13.80 (10.1%)

This type of comparison is usually applied in comparing the AHRS performance [2], yet, as can be seen in the case of the green route, even though Gallagher AHRS had the worst performance in orientation during the walk, it finished closer to the start point than all other

algorithms. This was the exception with regard to the other trials, which appropriately reflect the overall performance observed in each of the trajectories.

The orientation algorithm in this work is effectively composed by three components: the CF, the external influence compensation method and the bias estimation. The normalized computation time required to perform each of these tasks was determined using the *tic toc* function from MATLAB. A normalization of the processing time was performed with regard to the time taken to compute the orientation in the simplest case (only CF component). Each iteration execution time was averaged in order to obtain a reliable estimate, using the longest dataset collected. This procedure was repeated 10 times (nearly 150000 iterations) from which mean and standard deviation values were computed. Table 6.7 presents the results.

Table 6.7: Normalized processing time for each AHRS.

	This Work			**Madgwick**	**Gallagher**
	CF only	**No Bias**	**Full**		
Mean	1	1.574	1.619	1.413	1.372
STD	0.0053	0.00639	0.00637	0.0151	0.0056

Given an application scenario that requires orientation capabilities with low computational requirements, the CF only is the most suitable method, combining two types of orientations. Bias estimation can also be incorporated into the algorithm with a small penalty in the processing time. The full solution tested in this work, although slightly slower than the other solutions, incorporates bias estimation and presents the advantage that the algorithm can be configured based on the level of disturbances that are expected. An IMU in the waist, for example, is not subject to the same level of impacts and magnetic disturbances compared to an IMU placed in the ankle or the foot. Similarly, a walk in an outdoor scenario far from buildings and man-made structures will certainly encounter much smaller magnetic interferences compared to a walk in an indoor scenario.

6.7 Discussion

The SD method described enables accurate SD in different conditions that can be encountered in the indoor environment. The SD and SL enables the system to track the distance travelled by the user. Coupling this information with the orientation of the user from

an AHRS enables a stride-by-stride trajectory tracking, effectively providing an autonomous relative positioning system.

Instead of following a generic approach in the device placement, which would be compatible with any initial orientation, this work restricted the device placement to a specific location and orientation. This simplification reduced the computational burden to the sensor node, since only one axis is used in the SD algorithm. Since the device is strapped directly to the ankle of the user (and not to a shoe in the case of the foot mounted), no extra movement appears in the measurements derived from torsions in the shoe. On the other hand, by attaching the node to the ankle, some minor disturbances were expected due to the leg muscles that are activated during specific instants of the gait cycle. By applying a low pass filter to the signal of interest, these disturbances were greatly attenuated and did not influence the stride count.

This work highlighted the influence of misalignments that can occur when the user places the device in the ankle or due to posture or anatomy features of the user. To counter this effect, a three-dimensional approach must be used in order to provide accurate displacement information. The importance of these misalignments was also demonstrated in the improved SL estimation method, by comparing the performance of the method used in [5] to the solution proposed in this work.

In the case of the simple SL estimation method, a consistent underestimation of the SL was observed in the faster pace trials. One possible explanation for this is due to a greater contribution to the SL from the supporting foot during mid-swing. Since the gyroscope cannot detect this contribution, the SL has a tendency to be underestimated. By using equation (6.2), the SL is overestimated according to the model from Figure 6.4. This overestimation is countered by the fact that the model does not account for the SL contribution from the supporting foot.

When using the simple SL method, the leg length parameter becomes a very important scaling factor in determining the correct SL. This requires the user to measure and configure this parameter correctly. Other methods were experimented to measure this scaling factor, from which it was found that [10] was not only precise in terms of how to measure the leg length, but also produced consistent results in terms of distance travelled in the experimental trials. Further data collection and analysis with different users is necessary to confirm the accuracy and validity of this approach across users of different heights.

Ideally, the magnetometer absolute value would be unitary along the entire walk. This is seldom the case in indoor environment. Even with a perfect orientation algorithm that could account for changes in magnetic disturbances, orientation information would still be dependent on the location where the system initiated. Therefore, the Earth's magnetic field is not sufficient to provide an accurate and self-contained reference for the heading angle in indoor environment. Possibly either a stronger artificial magnetic reference could be used or, a higher layer of the navigation system should be responsible for the global correction of the heading angle produced by the AHRS, according to the current location of the user.

The orientation algorithm proposed allows a simple parameterization, through a preliminary evaluation of the level of external influences that the IMU is subject to in the required application. The method provides a generic approach to the fusion of two orientation algorithms. In the case of low computational devices, the bias estimation and external influence components of the orientation algorithm can be removed in order to lower computational requirements, allowing for design choices according to the application context.

6.8 References

[1] A. R. Jimenez, F. Seco, C. Prieto, and J. Guevara, 'A comparison of Pedestrian Dead-Reckoning algorithms using a low-cost MEMS IMU', in *2009 IEEE International Symposium on Intelligent Signal Processing*, 2009, pp. 37–42.

[2] X. Yun, J. Calusdian, E. R. Bachmann, and R. B. McGhee, 'Estimation of Human Foot Motion During Normal Walking Using Inertial and Magnetic Sensor Measurements', *IEEE Transactions on Instrumentation and Measurement*, vol. 61, no. 7, pp. 2059–2072, Jul. 2012.

[3] A. R. Jiménez, F. Seco, J. C. Prieto, and J. Guevara, 'Indoor pedestrian navigation using an INS/EKF framework for yaw drift reduction and a foot-mounted IMU', in *2010 7th Workshop on Positioning, Navigation and Communication*, 2010, no. section IV, pp. 135–143.

[4] E. Foxlin, 'Pedestrian tracking with shoe-mounted inertial sensors', *IEEE Computer Graphics and Applications*, vol. 25, no. 6, pp. 38–46, 2005.

[5] Q. Li, M. Young, V. Naing, and J. M. Donelan, 'Walking speed and slope estimation using shank-mounted inertial measurement units', in *2009 IEEE International Conference on Rehabilitation Robotics*, 2009, pp. 839–844.

[6] H. Weinberg, 'Using the ADXL202 in pedometer and personal navigation applications', 2002.

[7] J. W. Kim, H. J. Jang, D.-H. Hwang, and C. Park, 'A Step, Stride and Heading Determination for the Pedestrian Navigation System', *Journal of Global Positioning Systems*, vol. 3, no. 1&2, pp. 273–279, Dec. 2004.

[8] R. G. Stirling, 'Development of a Pedestrian Navigation System Using Shoe Mounted Sensors', University of Alberta, 2004.

[9] S. K. Park and Y. S. Suh, 'A zero velocity detection algorithm using inertial sensors for pedestrian navigation systems.', *Sensors (Basel, Switzerland)*, vol. 10, no. 10, pp. 9163–78, Jan. 2010.

[10] P. P. Gogia and J. H. Braatz, 'Validity and reliability of leg length measurements.', *The Journal of orthopaedic and sports physical therapy*, vol. 8, no. 4, pp. 185–8, 1986.

[11] A. D. Young, 'Comparison of Orientation Filter Algorithms for Realtime Wireless Inertial Posture Tracking', in *2009 Sixth International Workshop on Wearable and Implantable Body Sensor Networks*, 2009, pp. 59–64.

[12] H. D. Black, 'A passive system for determining the attitude of a satellite', *AIAA Journal*, vol. 2, no. 7, pp. 1350–1351, 1964.

[13] X. Yun, E. R. Bachmann, and R. B. McGhee, 'A simplified quaternion-based algorithm for orientation estimation from earth gravity and magnetic field measurements', *IEEE Transactions on Instrumentation and Measurement*, vol. 57, no. 3, pp. 638–650, 2008.

[14] A. Gallagher, Y. Matsuoka, and W.-T. Ang, 'An efficient real-time human posture tracking algorithm using low-cost inertial and magnetic sensors', in *Proceedings of 2004 IEEE/RSJ International Conference on Intelligent Robots and Systems*, 2004, vol. 3, pp. 2967–2972.

[15] J. Calusdian, X. Yun, and E. Bachmann, 'Adaptive-gain complementary filter of inertial and magnetic data for orientation estimation', in *2011 IEEE International Conference on Robotics and Automation*, 2011, pp. 1916–1922.

[16] S. O. H. Madgwick, A. J. L. Harrison, and R. Vaidyanathan, 'Estimation of IMU and MARG orientation using a gradient descent algorithm', in *2011 IEEE International Conference on Rehabilitation Robotics*, 2011, vol. 2011, pp. 1–7.

[17] F. L. Markley, 'Attitude Determination Using Two Vector Measurements', in *Flight Mechanics Symposium*, 1999, pp. 39–52.

[18] R. Mahony, T. Hamel, and J. M. Pflimlin, 'Nonlinear complementary filters on the special orthogonal group', *IEEE Transactions on Automatic Control*, vol. 53, no. 5, pp. 1203–1218, 2008.

[19] R. Feliz, E. Zalama, and J. G. García-Bermejo, 'Pedestrian tracking using inertial sensors', *Journal of Physical Agents*, vol. 3, no. 1, pp. 35–42, 2009.

Chapter 7

Conclusions and Future Work

This work proposed the study, development and test of an indoor positioning system for wireless sensor networks (WSNs). A generic implementation of a positioning system without limiting its application to a specific context was desired; as such, the achievable accuracy with current off-the-shelf components was explored. The indoor positioning system was integrated into a body posture monitoring system which uses an inertial measurement unit (IMU) to find the orientation of each body segment [1]. Two independent methods of position estimation were investigated, a received signal strength-based (RSS) and an IMU-based, in order to maximize accuracy, while having in consideration the system's efficiency due to the low power and low computational capability requirements associated with WSNs. In light of an efficient approach requirement, RSS positioning was used as the starting point, due to the necessary information being readily available in the WSN node, without the size and power consumption penalty of adding extra hardware capable of performing positioning measurements.

Two main issues were identified with the RSS approach: the lack of consensus on the use of RSS as the basis information for a positioning system and the high heterogeneity of the experimental conditions found in the literature. Nonetheless, the RSS approach was pursued

and a subset of the main RSS-based positioning methods from the literature was implemented and tested in the experimental performance comparison from Chapter 4.

The results from Chapter 4 revealed that the propagation model applied to RSS positioning performed poorly when the environment was severely affected by multipath propagation and due to the body effect. Distances estimated from the model were severely affected by biases that depended heavily on factors such as body orientation, line-of-sight (LOS)/non-line-of-sight (NLOS) conditions and proximity to other objects or walls. The experimental comparison demonstrated that, despite its simplicity, the weighted centroid localization (WCL) algorithm presents better performance than a map-matching solution for the experimental setup of this work. Also, a 55% improvement in accuracy was found when the body effect was removed from the positioning scenario. This conclusion paved the way to the work developed in Chapter 5, which not only studied the body effect in RSS positioning, but also a real-time path loss exponent (PLE) estimation method.

Given that the body presence heavily affects the RSS of transmitted messages, as demonstrated in Chapter 4, accounting for body influence was consequently seen as a possible solution, capable of bringing major improvements to the performance of RSS-based positioning algorithms. Since this system is integrated in a posture monitoring system, the orientation of the body was available to be used in the RSS positioning. This led to the creation of a body attenuation model using a controlled environment (anechoic chamber), in order to compensate for the body effect on the RSS information obtained from the anchor nodes. However, this body attenuation model has not improved the positioning algorithm performance under the same indoor experimental setup as used in Chapter 4. Three datasets with different distances between the body and the sensor node were evaluated and the importance of this distance parameter was highlighted. The results suggest that the multipath propagation effect was more intense when the body was closer to the sensor node and that the shadowing component of the attenuation played a minor role in the RSS. This undermined the performance of the body attenuation model used to compensate RSS readings when the node was near or attached to the human body, with performance degrading as the body approached the antenna.

The developed PLE estimation method (closest links path loss - CLP) explored the fact that the anchors in RSS-based positioning are configured with (or at least possess another method to find) their true location. Knowing the anchor locations allows the calculation of the

distances between anchors. Since each anchor broadcasts its beacon message, all other anchors in the vicinity also receive the beacon. With the information of distances and RSS from anchor nodes received by each anchor, a real-time PLE estimation method was developed. This method provided better accuracy than the WCL algorithm when the body was further apart from the antenna. When the body was closer to the antenna, the improvement was lost and the algorithm performance degraded compared to WCL. Given that the use case envisioned for this work attaches the sensor node(s) to the body of the user, the CLP method was not pursued in order to assess its improvement under a scenario without body influence. Nevertheless, it is believed that this method could provide accuracy improvements in scenarios where the human body is not present; as such its further assessment is left for future work.

Given the availability of an IMU, the inertial and magnetic information from the embedded sensors was used to provide an additional source of position estimation, namely a pedestrian dead reckoning in the form of a stride and heading system (SHS). This type of system is decomposed into two systems: a stride detection (SD)/stride length (SL) estimation system to detect strides and infer distance travelled and an attitude heading and reference system (AHRS) to provide orientation information. The latter of these systems typically employ filtering (or sensor fusion) techniques that require high computation capabilities (e.g., Kalman filters). Given the low computational capability of the sensor node, simplified filtering techniques were pursued, in order to satisfy the low power requirements of WSNs.

The solution for the SD system followed an approach based on the work in [2], but applying the IMU to the ankle, instead of the foot. The SD solution was implemented and compared against typical methods from literature, which are simple, low computationally demanding, threshold-based methods. A comparison between the methods proposed and current existing techniques was performed, under different conditions that can be encountered in the indoor environment. The results demonstrate that the proposed method is able to identify all true positives (i.e., when the stride occurs and is correctly detected). Some marginal signals in special events during the walk, such as turning or stopping and resuming the march, occasionally caused patterns identical to the stride pattern to emerge, being identified as false strides (i.e., false positives) as a result. The proposed algorithm outperformed the other methods for both subjects in the test, even though they already presented high percentage of correct SDs.

The approach used in this work was to imbue the SD system with a higher degree of functionality, identifying the stages of the gait cycle without resorting to complex algorithms. This in turn allowed the development of two heterogeneous SL estimation solutions: a first solution with lower computational demands, which provided lower accuracy in the SL estimation, but in agreement with the WSN requirements profile; and a second, more computationally demanding solution, which improves the method described in [3]. The first solution requires the configuration of a single parameter, the user's leg length, while the second solution does not use any parameters. A calibration phase is not necessary with the proposed methods, which frees the user from the requirements of understanding and performing a calibration of the SL estimation system.

The SD/SL data collected from the subject B exhibited higher errors than from subject A. An analysis of the gyroscope data from this subject showed that the placement of the sensor node in the ankle had a slight misalignment, which explains the high angular velocity measurements that were detected in both x and y axis during the stride. This subject also had a faster pace than subject A. Further testing is necessary in order to determine the cause for the higher error percentage observed.

A preliminary study of sensor fusion techniques showed that the complementary filter (CF), when applied to human motion, is able to provide better results with lesser computational complexity than the typical Kalman filter solution. A quaternion-based CF was chosen, and this method was investigated, implemented and compared with similar methods in the literature. The efficiency requirement of the WSN was taken in consideration for the selection of a quaternion-based approach in detriment of a rotation matrix approach. The quaternion-based approach requires a smaller number of parameters than a matrix (four versus nine), leading to fewer mathematical operations, and therefore it is also much simpler to normalize compared to a rotation matrix.

Given the level of interferences in the indoor environment, and the fact that the IMU is placed in the ankle, robustness against external influences was a necessity in order to apply the AHRS in indoor environment. The developed solution enabled a generic approach consisting of three components: the fusion of the gyroscope integration with a two-vector observation method using a CF; the external influence compensation method, which allows a simple parameterization according to the level of interferences expected from the accelerometer and magnetometer sensors; and a bias estimation component, using also a CF

to estimate the bias from the gyroscope sensor. The generic approach allows the external influence and the bias estimation components to become design choices when implementing the algorithm in devices with low computational capabilities.

Another issue is that the direction of walk is assumed to be coincident with the forward axis of the system, but this is not always the case, since misalignments can occur during the placement of the IMU on the ankle. Ideally, a perfectly placed IMU on the ankle would exhibit angular velocities different than zero, only in one axis. When a misalignment is present, angular velocity measurements different from zero appear mainly in the roll and pitch axes. One possible solution for this issue could be to infer the orientation of the walking direction by analysing the proportion of angular velocity that can be observed in the roll and pitch axes of the sensor. This proportion would then be converted to an angular displacement, which could be used to correct the heading direction whenever a stride is detected.

Two objectives from the work schedule were not accomplished as initially planned: the implementation of the positioning algorithms in an Android platform; and the fusion of both positioning systems, namely the RSS-based and the IMU-based approaches. The first objective was not pursued by choice, mainly due to the amount of design options that originated from the state-of-the-art research.

The RSS-based positioning was also a topic that delayed the work schedule. The RSS-based method was initially considered the main positioning method; however, due to the unfavourable results obtained in Chapter 4, a new search in the state-of-the-art was performed, in order to find any possible alternative algorithms for RSS-based positioning. This search proved unfruitful, given the efficiency requirement of the application scenario in WSNs, but on the other hand, it contributed to widen the state-of-the-art research from Chapter 2. This delay, together with the delay from the first objective, compromised the completion of the research for a method to fuse both RSS and IMU-based positioning systems.

These unaccomplished objectives are postponed for future work. The most important of the objectives is the fusion of both positioning methods. Current methods resort to particle filters, which are completely outside the scope of WSNs. This task however, could be transferred to the smartphone platform. The smartphone could also be used as the main device for orientation information (or at least for a redundant method capable of reducing orientation error), given that it possesses the type of sensors used in the IMU. The smartphone is typically

placed in the pocket or held in the hand while the user is moving. This translates into smaller impacts when walking and less magnetic interference, due to being further away from the ground. The smartphone could be used to improve the heading estimation, or as a bias estimation method for the yaw component of the gyroscope, which is the source of orientation error in the AHRS of the SHS in indoor environment.

The IMU device can be significantly improved with a dedicated hardware design, combining the CC2530 system-on-chip, the MPU6000 and the HMC5883L (or a similar hardware setup) in order to drastically reduce its size. In addition, a neoprene ankle bracelet could be applied to the IMU device, therefore enabling a more secure and comfortable attachment to the ankle of the user. The weight and size reduction could also bring improvements to the algorithm performance. The CC2530 could also be exchanged for the similar Bluetooth Low Energy module (CC2540) from the same manufacturer, which would be compatible with the smartphone approach. The RSS-based positioning could be delegated to the smartphone, along with the orientation part of the IMU-based positioning, leaving the SHS system to be implemented by the IMU device, in order to extend its battery life.

7.1 References

[1] H. D. Silva, P. Macedo, J. A. Afonso, and L. A. Rocha, ‘Design and implementation of a wireless sensor network applied to motion capture’, *1st Portuguese Conference on Wireless Sensor Networks (CNRS 2011)*, Coimbra, Portugal, 2011.

[2] R. G. Stirling, ‘Development of a Pedestrian Navigation System Using Shoe Mounted Sensors’, University of Alberta, 2004.

[3] Q. Li, M. Young, V. Naing, and J. M. Donelan, ‘Walking speed and slope estimation using shank-mounted inertial measurement units’, in *2009 IEEE International Conference on Rehabilitation Robotics*, 2009, pp. 839–844.